The Sun, Space Weather and Effects

Magnus Wik

Swedish Institute of Space Physics

Department of Physics, Lund University

2008

IRF

The Sun, Space Weather and Effects

Magnus Wik

Thesis for the degree of Doctor of Philosophy in Physics

Department of Physics, Lund University, Lund, Sweden
&
Swedish Institute of Space Physics, Lund, Sweden

LUND UNIVERSITY

Thesis advisor:	*Dr. Henrik Lundstedt* *Swedish Institute of Space Physics* *Lund, Sweden*
Faculty opponent:	*Dr. David Boteler* *Natural Resources Canada* *Geomagnetic Laboratory* *Ottawa, Canada*

Cover pictures:

Left:	*Illustration of emerging magnetic loops in the solar photosphere.*
Middle:	*Illustration showing the Sun, solar wind and the Earth.*
Right:	*Blackout in Malmö during the Halloween storm on 30 October 2003*

IRF Scientific Report 296
ISBN 978-91-628-7519-0
ISSN 0284-1703

Printed at the Swedish Institute of Space Physics
Box 812
SE-981 28, Kiruna, Sweden
October 2008

The night has a thousand eyes,
And the day but one;

Yet the light of the bright world dies,
With the dying Sun.

Francis William Bourdillon, 1878

Abstract

The Sun and the solar magnetic activity is responsible for a variety of effects in space and on the Earth. High energy radiation and charged particles are constantly being emitted from the solar atmosphere interacting with our atmosphere and technological systems in space and on the ground.

The research papers included in this thesis cover analysis of solar magnetic activity, solar indices, solar wind data and geomagnetic data. Also included are calculations of induced currents in power grids from geomagnetic disturbances and prediction of the geomagnetic field. The most common solar index, the sunspot number, was studied as a proxy for the total solar irradiance. The solar magnetic activity, in the form of synoptic maps, was analysed on many time scales from about a day up to several years. The data and the analysing tools used in the papers, wavelets and neural networks, are also briefly described.

This doctoral thesis is about space weather and solar-terrestrial physics. It is divided into a summary and five research papers. In the summary I present an outline of the solar-terrestrial environment: The Sun, solar magnetic activity, the heliosphere and the solar wind, geomagnetic storms and ground effects. I also briefly summarise each paper.

In the second part all five papers are reprinted. Papers **A** and **B** compare induced currents in technological systems, both measured and calculated, with geomagnetic disturbances and other solar-terrestrial data. Paper **C** use an empirical model, based on neural networks, to predict the local ground magnetic field fluctuations from solar wind data. Paper **D**, studies the relationship between solar indices and the total solar irradiance using wavelet analysis. Finally, paper **E** includes a multiresolution analysis of solar synoptic magnetic fields.

Populärvetenskaplig sammanfattning

På samma sätt som på jorden finns det väder i rymden, s.k. rymdväder, som påverkar oss dagligen. Källan till rymdvädret är vår närmsta stjärna, solen. För ca 4,6 miljarder år sedan skapades solen ur ett gigantiskt plasmamoln, och idag är solen en medelålders stjärna. Solen har en diameter som är 109 gånger större än jorden och en massa 330000 gånger jordens. I solens kärna, som har en temperatur på ca 15 miljoner grader, produceras energi i form av s.k. gamma-strålning, via omvandling från väte till helium, en process som kallas för fusion (till skillnad från fission som äger rum i kärnkraftverk).

Från kärnan transporteras energin genom två olika ”skal” eller områden. Det inre kallas för strålningszonen, som sträcker sig från kärnan ut till ca 70 % av solens radie, och det yttre kallas för konvektionszonen. Det tar ca 170000 år för energin, via strålning, att nå nedre delen av konvektionszonen. Temperaturen är där ca 2 miljoner grader. Därefter, i den s.k. konvektionszonen, transporteras energin vidare genom konvektion, innan den efter endast ca 1 månad når solatmosfären. Denna delas in i fotosfären (ca 500 km tjock och 5780 grader), kromosfären (ca 2500 km tjock och 10000 grader), övergångsregionen (ca 100 km tjock) och därefter koronan (några miljoner grader) som är solens yttersta atmosfärslager (Figur 2.1).

Varje sekund ”förlorar” solen ca 5 miljoner ton materia genom strålning och den s.k. solvinden. Strålningen består framförallt av synligt ljus men även av ett brett spektrum från radio upp till gammastrålning. Observationer i en del av våglängdsområdena kan ge information om bl.a. solens magnetfält i olika områden i solatmosfären. Med hjälp av den s.k. Zeeman-effekten, där en spektrallinje delas upp i flera komponenter pga magnetfältet, kan man studera solens magnetfält med hjälp av en s.k. magnetograf. Med hjälp av denna skapar man ett s.k. magnetogram, som är en bild av solens magnetfält. För att studera hur magnetfältet utvecklas med tiden konstruerar man i sin tur s.k. synoptiska kartor. För varje dag tar man ut ett smalt område av magnetogrammet längs med den centrala meridianen (en tänkt cirkel som passerar genom nordpolen och sydpolen på solen). Dessa områden, som bildar smala rektanglar, läggs samman efter ca 27 dygn så att man får en ungefärlig bild av solens magnetält under en solrotation.

Själva magnetfältet genereras troligtvis i ett område som kallas för tachocline, ett turbulent område mellan strålningszonen och nedre delen av konvektionszonen. Uppkomsten av detta område beror på att solen roterar som en stel kropp i strålningszonen medan den roterar differentiellt (med olika hastighet) i konvektionszonen. Denna process, där solens magnetfält genereras, kallas för soldynamon. I början av en cykel har magnetfältet formen av en dipol. Pga av den differentiella rotationen, där hastigheten är högre vid ekvatorn jämfört med vid polerna, övergår magnetfältet från att vara poloidalt (norr-söder eller tvärtom) till att bli mer toroidalt (väst-öst eller öst-väst). Denna process kallas för Omega-effekten. När magnetfältet bli tillräckligt kraftigt lyfts det upp genom fotosfären, varvid solfläckar bildas. Dessa består av två olika områden med olika polaritet, där positiv polaritet motsvarar magnetfält som passerar upp genom solytan, och negativ polaritet

motsvarar magnetfält som passerar ner genom solytan. Efter hand så rör sig dessa områden, dels mot polerna, där det poloidala magnetfältet ändrar riktning, och dels mot ekvatorn där de neutraliseras. Den magnetiska cykeln är nu fullbordad.

Solvinden består av två komponenter, en långsam och en snabb, där den långsamma kommer från s.k. coronal streamers och den snabba från koronahål (på eng. coronal holes). Emellanåt inträffar enorma utbrott på solen, s.k. koronamassutkastningar (på eng. coronal mass ejections, CME). Dessa består av laddade partiklar, främst elektroner och protoner, med en total massa på upp till flera miljarder ton. I samband med dessa kan man även få intensiva strålningsutbrott (på eng. solar flares), med kraftig röntgen- och UV-strålning. Det är framförallt s.k. halokoronamassutkastningar, riktade rakt mot jorden, som kan ställa till störst problem för teknologiska system i rymden och på marken.

När solvinden når jordens magnetfält pressas det samman på dagsidan och sträcks ut till en svans på nattsidan. En ”magnetisk bubbla” skapas runt jorden som kallas för magnetosfären, där en mängd olika plasmaprocesser kontrolleras av jordens magnetfält (Figur 3.1).

Det är solvindens hastighet, densitet och magnetfält som bestämmer hur energi överförs till magnetosfären. Om solvindens magnetfält har en riktning motsatt jordens, kan mer energi överföras till magnetosfären. Man kan då få en s.k. geomagnetisk storm. Detta kan i sin tur leda till norrsken runt polerna samt kraftigare strömsystem i magnetosfären och jonosfären.

Under en geomagnetisk storm bildas strömmar på ca 100 km:s höjd uppe i jonosfären. Dessa kan nå en strömstyrka på flera miljoner Ampere. De uppstår på höga latituder som t.ex. Nordamerika och Skandinavien. När strömmarna varierar med tiden induceras ett elektriskt fält på jordytan som i sin tur kan driva strömmar i olika ledare, t.ex. kraftledningar, kommunikationskablar, pipelines och järnvägsräls. Dessa strömmar kallas med ett gemensamt namn för geomagnetiskt inducerade strömmar (på eng. geomagnetically induced currents, GIC).

Kraftindustrin är den bransch som har haft störst problem med GIC. Sveriges kraftnät består bl.a. av långa kraftledningar sammankopplade via transformatorer. Som skydd är transformatorerna vanligtvis jordade. Under normal belastning är strömmen noll i jordningen, men under en geomagnetisk storm kan GIC ta sig in via jordningen, följa kraftledningarna, och ta sig tillbaka till jord via andra transformatorer. GIC är, till skillnad från växelströmmen på 50 Hz som vi har i våra hushåll, närmast en likström. En mängd problem kan uppstå då strömmen passerar transformatorlindningen. Transformatorn kan skadas och skapa överhettning i kyloljan och s.k. övertoner i strömmen kan leda till att skyddsrelän löser ut och kan även leda till urkoppling av flera ledningar. Detta kan orsaka en kollaps av nätet. Graden av störning beror på t.ex. kraftnätets geografiska placering, markkonduktiviteten, nätets uppbyggnad samt transformatordesignen.

Under den kraftiga geomagnetisk stormen, 13–14 mars 1989, kollapsade elnätet Hydro-Québec, i Kanada, varvid 6 miljoner människor blev strömlösa i upp till 9 timmar. Även i Sverige har det inträffat flera störningar på nätet på grund av GIC, varav den kraftigaste inträffade under ”Halloween-stormen”, den 30 oktober 2003, då Malmö drabbades av strömavbrott.

Den här avhandlingen omfattar totalt fem artiklar inom solfysik och rymdväder. Den första artikeln, **A**, behandlar beräknad och uppmätt GIC i 400 kV-kraftnätet i södra Sverige. I den andra artikeln, **B**, analyserar vi två kända rymdvädershändelser. Den första, 13–14 juli 1982, påverkade signalsystemet hos banverket. Den andra, 29–30 oktober 2003, gav upphov till ett strömavbrott i Malmö.

Artikel **C** omfattar prognoser, med användandet av empiriska modeller, av det lokala

geomagnetiska fältet från solvindsdata. I artikel **D** studerade vi förhållandet mellan indikatorer av solaktiviteten och totala instrålningen med hjälp av waveletanalys. I artikel **E** analyserade vi solens magnetiska aktivitet, i form av s.k. synoptiska kartor, på tidsskalor från ungefär en dag till flera år. Tillsammans utgör dessa artiklar en gemensam studie av vår sol, vårt rymdväder och dess effekter.

Thesis and list of publications

This doctoral thesis contains a summary and the following five papers. In the text, each paper will be referred to by its respective letter.

Paper **A**:

M. Wik, A. Viljanen, R. Pirjola, A. Pulkkinen, P. Wintoft and H. Lundstedt
Calculation of geomagnetically induced currents in the 400 kV power grid in southern Sweden
Space Weather, 6, S07005, doi:10.1029/2007SW000343, 2008.

Paper **B**:

M. Wik, R. Pirjola, H. Lundstedt, A. Viljanen, P. Wintoft and A. Pulkkinen
Space weather events in July 1982 and October 2003 and the effects of geomagnetically induced currents on Swedish technical systems
Submitted, Annales Geophysicae, 2008.

Paper **C**:

P. Wintoft, M. Wik, H. Lundstedt and L. Eliasson
Predictions of local ground geomagnetic field fluctuations during the 7–10 November 2004 events studied with solar wind driven models.
Annales Geophysicae, 23, 3095–3101, 2005.

Paper **D**:

P. Wintoft, M. Wik, and H. Lundstedt
Sunspot records as proxy for total solar irradiance
Submitted, Annales Geophysicae, 2008.

Paper **E**:

M. Wik, H. Lundstedt and P. Wintoft
Multiresolution analysis of synoptic solar magnetic fields
To be submitted, Annales Geophysicae, 2008.

Acronyms and notations

Below is a list of symbols, acronyms and units used in this thesis. Bold letters denote vector quantities.

Acronyms

AC	Alternate current
ACE	Advanced Composition Explorer
AE	Auroral electrojet index
CME	Coronal mass ejection
COST	European Cooperation in the field of Scientific and Technical Research
CR	Carrington rotation: The number of rotations of the Sun (starting from 9 Nov. 1853)
CWT	Continuous wavelet transform
DC	Direct current
Dst	Storm-time Disturbance index of geomagnetic activity
DWT	Discrete wavelet transform
ELFORSK	Its overall aim is to coordinate the power industry's joint research and development
E.ON	Energy On - One of the world's leading energy companies
ESA	European Space Agency
FMI	Finnish Meteorological Institute
GIC	Geomagnetically induced current
G2	Spectral class 2
GSFC	NASA Goddard Space Flight Center
IMAGE	International Monitor for Auroral Geomagnetic Effects
IMF	Interplanetary magnetic field
IMP8	Satellite Interplanetary Monitoring Platform 8
INTERMAGNET	International Real-time Magnetic Observatory Network
IRF	Institutet för rymdfysik (Swedish Institute of Space Physics)
ISES	International Space Environment Service
Kp	3–hour planetary index of geomagnetic activity
L1	Lagrange point 1
MDI	Michelsen Doppler Imager
MHD	Magnetohydrodynamics
MODWT	maximal overlap DWT
MRA	Multiresolution analysis
MSFC	NASA's Marshall Space Flight Center
NASA	National Aeronautics and Space Administration

NN	Neural network
NOAA	National Oceanic and Atmospheric Administration
NWS	National Weather Service
OKG	Oskarshamns kärnkraftsgrupp (”Oskarshamn nuclear power plant group”)
R_z, R_g	Sunspot and group sunspot number
RWC	Regional Warning Center
SCHA	Spherical Cap Harmonic Analysis
SDA	Service Development Activity
SDO	Solar Dynamics Observatory
SEC	Space Environment Center
SECS	Spherical elementary current systems
SIDC	World Data Center for Sunspots in Brussels, Belgium
SOHO	Solar and Heliophysics Observatory (spacecraft located at L1)
SSA	Sunspot area
SVK	Svenska Kraftnät (Swedish power grid)
SWPC	Space Weather Prediction Center (formerly SEC)
TSI	Total solar irradiance
WDC	World Data Center
WIND	Spacecraft at L1
WSO	Wilcox Solar Observatory
WT	Wavelet transform

Notations

$\mathbf{B}$	magnetic field
$\mathbf{E}$	electric field
pfu	particle flux unit = 1 particle $\mathrm{cm}^{-2}\mathrm{s}^{-1}\mathrm{sr}^{-1}$
t	time
$\mathbf{v}$	velocity
σ	electrical conductivity
μ_0	permeability of free space
$\mathbf{Y}$	network admittance matrix
$\mathbf{Z}$	earthing impedance matrix
I_i	earthing current
I_{ij}	current along transmission line
R_{ij}	line resistance
R_i	earthing resistance
$Z(\omega)$	surface impedance
V_{ij}^0	geovoltage
ω	angular frequency

Contents

Chapter 1

Introduction

Our nearest star, the Sun, is powered by nuclear reactions in the core converting mainly hydrogen to helium, and in return energy is created. The energy is transported as electromagnetic radiation in the radiation zone and then as convective motions in the convection zone. In the photosphere almost all of this energy is released again as electromagnetic radiation in a broad spectrum of wavelengths from radio waves to gamma rays, with most of the energy in the visible part of the spectrum. Observations at certain wavelengths can give us information about e.g. the magnetic fields on the Sun using the Zeeman effect. Synoptic maps of the magnetic field can give us information about the transport and complexity of the magnetic flux. A well known indicator of the solar activity is the sunspot number. Together with other indices, such as the 10.7 cm radio flux and the total solar irradiance, they are a measure of the evolution of the solar magnetic activity (Schrijver and Zwaan (2000)).

The magnetic fields are generated deep in the convection zone, close to the radiation zone in a region called the tachocline. In a cycle of about 11 years, magnetic flux tubes first rise up through the photosphere, lifted by bouyancy, to produce magnetic active bipolar regions. The closed fields form loops extending up into the corona whereas open field lines extend further out into the heliosphere and the solar system. This also means that we are under the influence of many phenomena related to the solar magnetic field. These phenomena cause a variety of effects in the Earth's environment and on technological systems ranging from small temporal and spatial scales, like induced currents in a power system on the ground to the modulation of the Earth's climate. A common name for these phenomena and their associated effects is "Space Weather" (e.g. Bothmer and Daglis (2007)).

What is space weather? In 1995, The National Space Weather Program (NSWP), in USA, defined space weather as (Robinson et al. (2001)):

> "Space weather refers to conditions on the Sun and in the solar wind, magnetosphere, ionosphere, and thermosphere that can influence the performance and reliability of space-borne and ground-based technological systems and can endanger human life or health. Adverse conditions in the space environment can cause disruption of satellite operations, communications, navigation and electric power distribution grids, leading to a variety of socioeconomic losses."

A newer, European definition, created by COST 724 in 2007, is as follows (Lilensten and Belehaki (2008)):

> "Space weather is the physical and phenomenological state of natural space environments. The associated discipline aims, through observation, monitoring, analysis and modelling, at understanding and predicting the state of the Sun, the interplanetary and planetary environments, and the solar and non-solar driven perturbations that affect them, and also at forecasting and nowcasting the potential impacts on biological and technological systems."

This thesis is based on five papers with space weather as the common theme. The thesis is divided into two parts, a summary and the five papers. In chapter 2, I present a general overview of the Sun together with the solar magnetic activity and the solar dynamo. Chapter 3 starts with a general description of space weather and international organisations associated with space weather. Next I present an overview of our magnetosphere and ionosphere followed by a discussion of geomagnetic storms and substorms. The last two sections of chapter 3 cover ground effects of space weather by containing presentations of geoelectromagnetic fields and geomagnetically induced currents (GIC). The data and analysing tools used in the thesis work are described in chapters 4 and 5, respectively. Finally, conclusions and an outlook for future studies are presented in chapter 6.

Chapter 2

The Sun

Compared to other stars in our galaxy, the Milky Way, our closest star, the Sun, is an ordinary type G2 star. It is situated about 28000 light years from the galaxy centre. Still, the Sun is a very special star to us, due to its close proximity to the Earth only 8 light-minutes away. It is also the only star that we can study in detail and the only star, except for supernovas, that has an direct impact on us. For comparison, the nearest neighbour to our Sun, Proxima Centauri, is 4.3 light-years away. The Sun is a middle aged star, about $4.6 \cdot 10^9$ years old. The radius is about 109 times that of the Earth (695500 km). The mass of the Sun is about 330000 times the Earth's mass. The primary elements of the Sun are hydrogen (about 74 % of its mass) and helium (about 24 % of its mass). Heavier elements constitute only about 2 % (Schrijver and Zwaan (2000)).

In the core of the Sun, with a temperature of 15.6 million degrees kelvin, energy is produced in the form of gamma-rays, as a by-product in the conversion from hydrogen to helium, in a process called fusion. The energy is transported from the core, first by radiation through the radiation zone, extending out to about 70% of the solar radius. The temperature has now decreased to about 2 million K. Here, in the bottom of the convection zone, the temperature is cool enough for some heavy nuclei to capture electrons. These heavy particles absorb photons and block the radiation transport. In the convection zone, the energy is transported, as the name suggests, by material convection until it reaches the solar atmosphere. It takes about 170000 years for the energy to reach the bottom of the convection zone, and only about 1 month to continue to the top. There the hot material, in the convection cells, cools by radiating the energy out into space while the material sinks back once again to be reheated.

The solar atmosphere is divided into several layers with different properties. The photosphere (from photos, Greek word for light), with a thickness of about 500 km and an effective temperature of 5780 K, is the visible layer where most of the light originates. Going further outwards the temperature first reaches a minimum of about 4300 K until we enter a region called the chromosphere, believed to be heated by magneto-acoustic waves (from chromos, the Greek word for color). This faint layer, compared to the photosphere, has a thickness of about 2500 km. The temperature rises to about 10^4 K in the chromosphere, but the density is much lower than that of the photosphere. The temperature then increases extremely rapidly in the transition layer, with a thickness around 100 km, from about 10^4 K to 10^6 K. The outermost layer, the corona, is a very tenuous layer extending outwards several solar radii. Due to the very high temperature, a few million K, the plasma (consisting of charged particles i.e. ions, protons and electrons) is ionized several times. The structure of the Sun is shown in Figure 2.1.

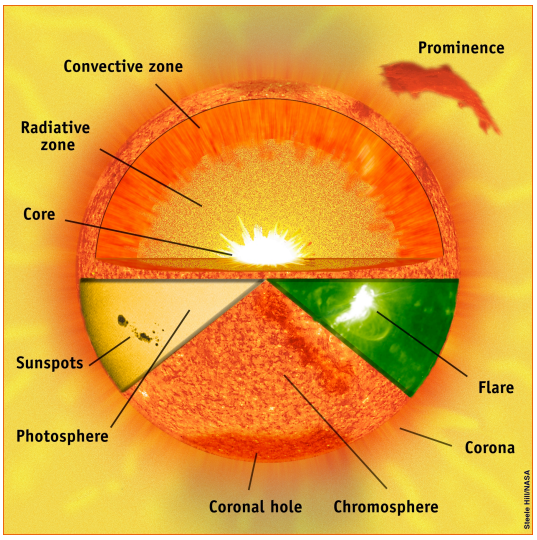

Figure 2.1: Cross section of the Sun : An illustration of the different layers of the Sun and associated phenomena (Courtesy of SOHO/EIT ESA/NASA).

2.1 Solar magnetic activity

The earliest evidence that our Sun has some sort of activity comes from observations of sunspots. These have been observed for many thousands of years but were observed for the first time with a telescope in 1610-11. In the middle of the 19th century it was determined that the number of sunspots vary according to a roughly 11-year cycle (Bhatnagar and Livingston (2005)).

In 1908, the first observations, using the Zeeman effect, of the magnetic field in a sunspot were made by George Ellory Hale at the Mount Wilson Observatory, in California. He discovered that the magnetic field in a sunspot was about one thousand times stronger than the magnetic field of the Earth. Sunspots are dark because they are cooler than the surrounding photosphere. The temperature at the centre of a sunspot is about 2000 K lower than the surrounding gas. It is the strong magnetic field, in the sunspot, that suppresses convective flow of hot plasma to reach the surface in the sunspot region. Sunspots are comparable in size with the Earth and have lifetimes ranging from hours to months. Apart from sunspots, the whole solar surface is covered with a complex network of magnetic fields. There also exist localised concentrations of magnetic flux, in hot and dense regions, called Plages. These regions are chromospheric phenomena and are often located near sunspots.

New magnetic flux, emerging from below the photosphere, sometimes form “active regions”. Sunspots correspond to the most intense phase of an active region. This occur especially around a solar maximum, where the magnetic field can evolve into great complexity and a build-up of magnetic energy. Occasionally, this energy is released in the solar corona in the form of a coronal mass ejection (CME). A CME can carry away 5 to 50 billion tons of matter from the corona, and reach speeds up to about 2500 km/s.

A solar flare is another phenomenon related to the magnetic field. A flare is an explosive event releasing high-energy protons and electrons, including intense radiation in all wavelengths. The time of an outburst is related to the magnetic field complexity in an active region. A CME and a flare event that occurred on 28 October 2003, are shown in Figure 2.2. Several solar events occurred during the intense “Halloween storms” on 28–30 October 2003.

The solar wind consists of charged particles, mostly protons and electrons, flowing

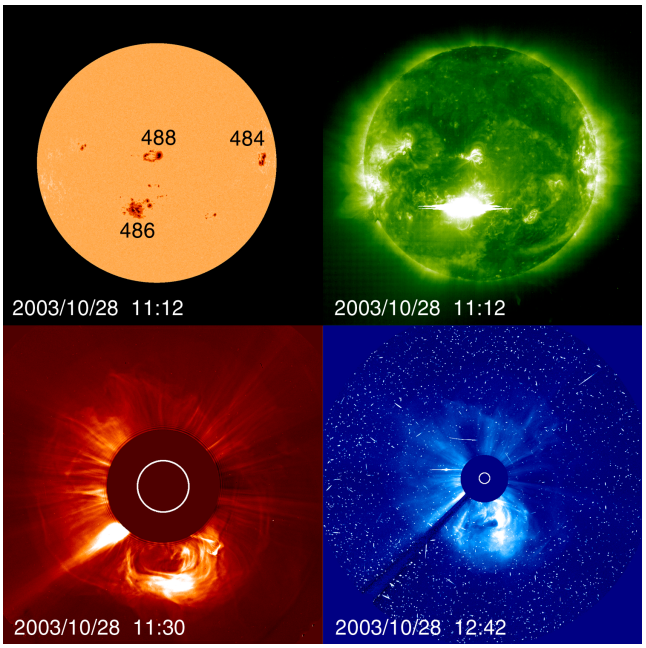

Figure 2.2: White light image of the active regions 484, 486 and 488 on 28 October 2003. Also shown are an X17 flare and a CME. Another CME on the 29th, from the active region 486, eventually resulted in a power blackout in the city of Malmö, Sweden, the following day (Courtesy of SOHO).

continuously out into the interplanetary space from the corona. The flow exists because of the pressure gradient between the corona and the interplanetary medium. This pressure difference overcome the solar gravitational pull on the plasma. Observations of comet tails gave the first indirect evidence of the solar wind. There are two different types of solar winds: a slow and a fast solar wind. The slow solar wind originates from coronal streamers, with an average speed of about 300 km/s. The fast solar wind comes from coronal holes, which are areas where cool gas can expand outwards into the interplanetary space due to open magnetic field lines. These field lines are dragged out by the solar wind forming the interplanetary magnetic field (IMF). Due to the solar rotation, this field is shaped into a spiral. During a solar minimum, coronal holes are often located at the poles, and at a maximum they can be found closer to the equator. The fast solar wind has an average speed of about 700 km/s (Priest (1982)).

The fast solar wind from coronal holes sometimes interacts with the slow wind producing shock fronts. Since the source regions of the two types of solar wind are often long-lived, the shock fronts, or recurrent structures, have a "periodicity" of about 27 days, sometimes seen in solar wind data. They are characterised by an increase in the solar wind density and speed. Coronal mass ejections are also able to form shock fronts when high-speed CMEs, between 1000–2000 km/s, interact with the slower solar wind. This shock front can trigger an initial phase, or sudden commencement, of a geomagnetic storm. A solar proton event is an indication of a halo-CME. Protons are then accelerated to very high speeds and can reach the Earth within 30 minutes. An overview of the solar wind can be found in Meyer (2007).

The solar wind is constantly flowing outwards, at supersonic speed, carrying with it the interplanetary magnetic field. This radial outflow creates a huge bubble called the heliosphere (from helios, the Greek word for the Sun). The heliosphere is the region of space that is influenced by the Sun and the solar wind. This region encompasses the entire

solar system out to about 150 times the distance between the Earth and the Sun. This means that not only the Earth is affected by space weather, but in fact the entire solar system. One can therefore say that we actually live inside the solar atmosphere.

The solar activity is often described by the sunspot number, R_z, which is the longest time series, or index, we have from solar observations going back to the 17th century. The sunspot number varies with a cycle of about 11 years. A solar cycle is the time interval between two successive minima. Other proxies for solar activity are the group sunspot number, R_g, and the sunspot area, SSA. Commonly used physical indices are the Total Solar Irradiance (TSI), Ultraviolet radiation (UV), 10.7 cm radio flux and Cosmic rays. They are all modulated by the varying solar activity. There are many other indices, both direct and indirect, that in some way are related to the activity of the Sun (Schrijver and Zwaan (2000)). In paper **D** we derive a proxy for TSI using sunspot records.

The Solar Heliospheric Observatory (SOHO), launched in 1995, is today the most advanced spacecraft that continuously monitors the Sun. It is located at Lagrangian point 1 (L1), about one one-hundredth of the way from the Earth to the Sun, i.e. at a distance of about 1.5 million km towards the Sun. SOHO has three instruments to study the interior of the Sun, six instruments for studies of the solar corona and three for studies of the solar wind. This spacecraft has revealed a new picture of the Sun, of the structure of its interior, of phenomena in the solar atmosphere and direct, in-situ, measurements within the solar wind. SOHO is a cooperation between NASA and ESA (Fleck et al. (1995)).

The Sun rotates, relative to the stars, with a sidereal rotation period of 25.4 days at the equator, and 33.4 days at 75 degrees latitude. This varying rotation is known as differential rotation, which persists to the bottom of the convective zone. The synodic rotation period (as seen from the Earth) of the solar equator, is about 27.3 days. The Carrington rotation (CR), arbitrarily taken to be 27.2753 days, of the Sun is a system for comparing locations on the Sun over a period of time. Each rotation is given a "Carrington Rotation Number" starting from 9 November 1853.

The Sun's interior flows in ways other than rotation. Deep zonal bands of slightly faster and slower rotation gradually move from high latitudes toward the equator over a few years period. The motion of these bands is consistent with the similar drift of sunspots. There is also another flow, the meridional flow, from the equator to the poles. There is likely also a return flow to the equator. This is related to the transport of magnetic flux to high latitudes and the reversals of the polar magnetic fields. Work is in progress to understand this for many temporal scales (paper **E**).

Using a magnetograph, that consist of an array of tiny detectors, it is possible to detect the magnetic field on the Sun using the Zeeman effect. The result, a magnetogram, shows the locations and strengths of the magnetic fields on the solar disc. Today, magnetograms are produced on a daily basis from observations both on the ground and in space.

From a magnetogram it is also possible to construct a synoptic map of the magnetic field that shows the magnetic field on the Sun for one solar rotation. A synoptic map is constructed from line-of-sight magnetograms. Each day a strip along the central meridian is cut out from a magnetogram. Since the solar rotation is about 27 days a synoptic map is constructed by adding up 27 stripes to give a two-dimensional visualisation of the solar magnetic field. A synoptic map is basically a contour map of the photospheric magnetic field over the entire surface of the sun. A synoptic map, constructed at the Wilcox Solar Observatory (WSO), Stanford, is shown in Figure 2.3.

The longitudinally averaged line-of-sight magnetic fields (in μT), observed at WSO is shown in Figure 2.4. This shows how the magnetic field, averaged over a Carrington rotation, gradually changes over time. It is derived by calculating the average magnetic

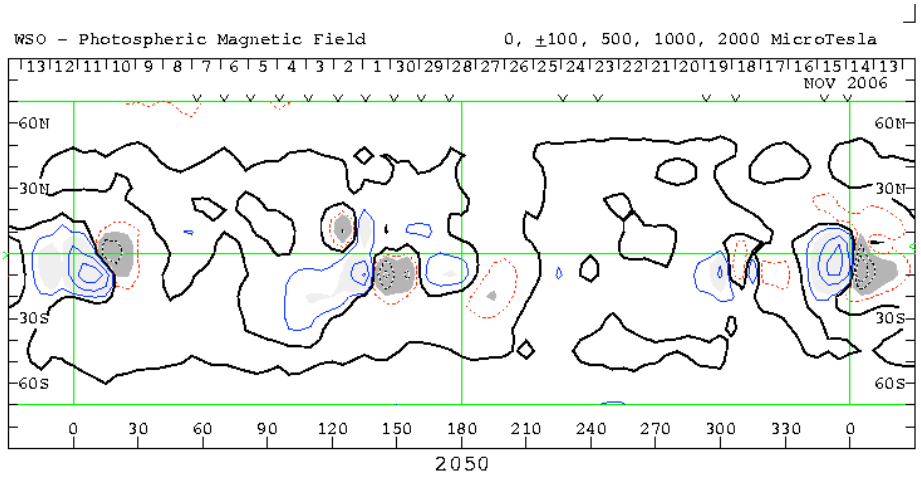

Figure 2.3: Synoptic map of the Sun based on WSO magnetograms (Courtesy of WSO/Stanford).

flux density for each latitude and synoptic map. In paper **E** we derive the diagram using wavelet analysis.

Ideally, one would like to have a real-time map of the solar vector magnetic fields. With the launch of the Solar Dynamics Observatory (SDO) in 2009, the successor of SOHO, we will finally have access to real-time vector magnetograms with a resolution of 1 arcsec. It is the first mission to be launched for NASA's Living With a Star (LWS) Program.

2.2 Solar dynamo

The solar magnetic activity changes on many temporal and spatial scales, from small-scale complex structures to large-scale ordered fields. Sunspots are confined to a belt between ∼30 degrees north and south of the solar equator. At the start of a new cycle they appear at around ±30 degrees and appear to move closer to the equator over a period of approximately 11 years. This is known as the Schwabe cycle, from Heinrich Schwabe who determined that the number of sunspots vary over an approximate period of 11 years (Schwabe (1843)). This can be seen in a "sunspot butterfly diagram", where the locations of the sunspots are shown as functions of latitude and time. The sunspot butterfly diagram is shown in Figure 2.5.

With the Michelsen Doppler Imager (MDI) instrument onboard SOHO it is possible to detect oscillating waves on the solar surface due to sound waves in the convection zone of the Sun. These sound waves have revealed the temperature distribution and dynamics of the interior down to the radiative zone. This research field is called "helioseismology". We now know that the Sun rotates as a solid body in the radiative zone and differentially, faster at the equator than at the poles, in the convective zone. Together with turbulent and helical plasma flow, the solar magnetic field and the sunspots can then be generated by a process called the solar dynamo (e.g. Charbonneau (2005)).

The solar differential rotation first stretches the magnetic fields around the Sun, transforming a meridional (north – south or vice versa) magnetic field into an azimuthal (east – west or vice versa) magnetic field. This process is called the Ω-effect. This is schematically shown in Figure 2.6. The magnetic field returns to a meridional field by the α-effect due to convective motions and rotation generating small-scale meridional loops.

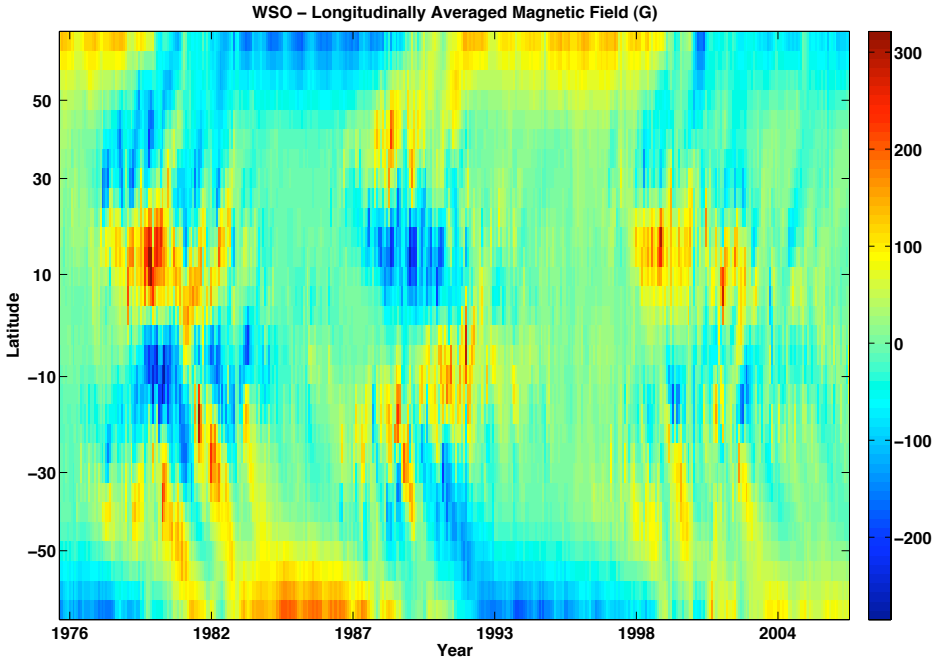

Figure 2.4: Longitudinally averaged line-of-sight magnetic field observed at WSO, Stanford. The color scale is in unit μT (data from WSO/Stanford) (from paper **E**).

Due to the stretching of magnetic field lines, the azimuthal field becomes buoyant and starts to rise. Sunspots are often formed in bipolar pairs, when these magnetic flux tubes pierce through the photosphere. The sunspot pairs are often lined up slightly tilted with respect to the equator, a tendency called Joy's law. The spots also follow Hale's law, where the leading spots (L) have the same polarity in the same hemisphere, and the reverse polarity in the other hemisphere (see Figure 2.6). During the next solar cycle, the pattern of polarities changes. A complete cycle is therefore about 22 years, the magnetic solar cycle. The solar magnetic field in the polar regions also reverses polarity in an interval of around 11 years, but out of phase with the sunspot cycle. Sunspots are described in e.g. Schrijver and Zwaan (2000).

Since the dynamo mechanism is related to the differential rotation, the Sun's large-scale magnetic activity is likely generated and maintained in the tachocline, a turbulent layer between the radiative zone and the lower convective zone. The solar dynamo theory can be described by solar magnetohydrodynamics (MHD), which is the study of the interaction between magnetic fields and moving, conducting, fluids (e.g. Davidson (2001)).

The fundamental problem of solar-MHD is to explain the origin of the Sun's magnetic field. This dynamic field is responsible for all solar magnetic phenomena, such as e.g. flares, CMEs, solar wind and the heating of the corona. In dynamo theory the solar magnetic field, $\mathbf{B}$, is maintained by the motion, $\mathbf{v}$, of an electrically conducting fluid, where the motion of the fluid induces those electric currents needed to sustain the field.

By combining Maxwell's equations and Ohm's law for a moving conductor we get the induction equation

$$\frac{\partial \mathbf{B}}{\partial t} = \nabla \times (\mathbf{v} \times \mathbf{B}) - \nabla \times [\eta \nabla \times \mathbf{B}] \tag{2.1}$$

where η is the magnetic diffusivity defined as

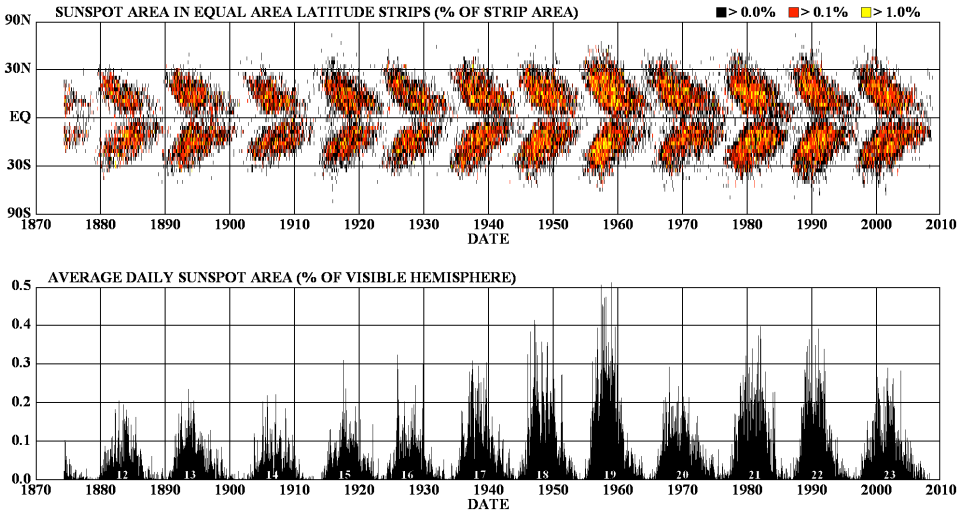

Figure 2.5: Sunspot cycle: Upper panel shows the location of sunspots. The lower panel shows the total area, in percentage, of the sunspots that cover the visible hemisphere (Courtesy of NASA/MSFC).

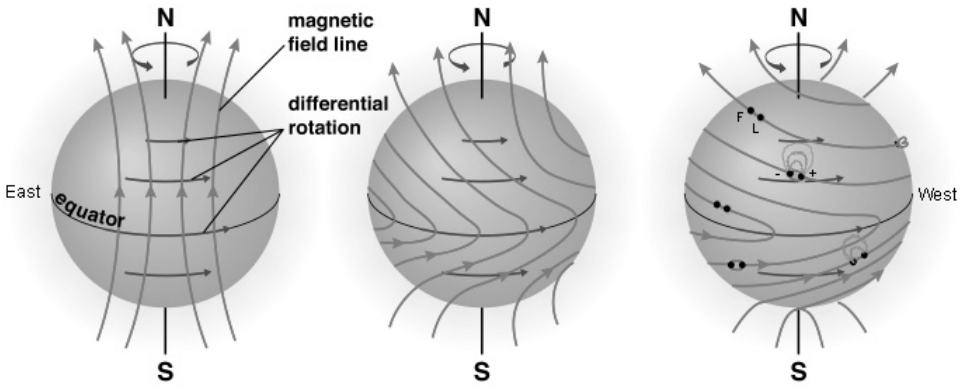

Figure 2.6: Generation of the toroidal magnetic field and emerging bipolar regions. The Sun rotates from east to west so leading (L) sunspots are to the right and following sunspots (F) to the left.

$$\eta = \frac{1}{\mu_0 \sigma} \tag{2.2}$$

where μ_0 is the permeability of free space and σ is the electrical conductivity. The induction equation determines $\mathbf{B}$ once the plasma speed $\mathbf{v}$ is known. The first term on the right-hand side, the convection term, represents the inductive effects of motions which lead to an increase in the magnetic field. The second term, the diffusion term, describes the diffusion of magnetic field lines with the flow.

The magnetic field is divided into two components, the poloidal (meridional) field and the toroidal (azimuthal) field, described above. The poloidal field generates a toroidal field by the differential rotation. A strong differential rotation in the tachocline can then generate a very large toroidal field (about 10 T). Convection and the coriolis force give rise to a helical motion that in turn twists parts of the toroidal field into loops that together form the poloidal field. The induction equation, for the mean field, describes how small-scale fluctuations give rise to a large-scale magnetic field. In the mean-field MHD approach

the velocity and the magnetic field are split into an average and a fluctuating part. An overview of MHD models are described by Charbonneau (2005).

Chapter 3

Space weather and effects

Coronal mass ejections (CMEs), heading towards the Earth, can cause most problems to technological systems in space and on the ground. Since these phenomena are caused by the magnetic activity of the Sun, they vary, on average, in strength and frequency with a "period" of about 11 years, the so-called solar cycle. Space weather changes, in temporal scales, from short-term (minutes to hours to days), medium-term (days to months) to long-term (∼11 years and longer). Since space weather can affect our society in many ways it is a highly relevant research subject. During a solar maximum the activity is the highest when we can expect more intense CMEs and flares. During a minimum there are fewer events, although large events can still occur at any time. The radiation from a flare reaches the Earth within 8 minutes, proton events within 30 minutes and coronal mass ejections within 1-2 days. This makes it difficult to make predictions of space weather.

The International Space Environment Service (ISES), is an important organisation where scientists can exchange space weather data and provide space weather forecasts to different customers (http://www.ises-spaceweather.org/). The forecasts are being provided through different Regional Warning Centers (RWCs) around the world. At present, there are twelve RWCs around the world: Boulder (RWC-USA), Ottawa (Canada), Lund (Sweden), Beijing (China), Moscow (Russia), New Delhi (India), Prague (Czech Republic), Tokyo (Japan), Sydney (Australia), Brussels (Belgium), Warsaw (Poland) and Hermanus (South Africa). The Director of ISES is David Boteler at RWC-Canada and the Deputy Director is Henrik Lundstedt at RWC-Sweden. In Europe there also exists a collaboration coordinated by the European Space Agency (ESA).

In the USA, space weather forecasts on a daily basis are available from the Space Weather Prediction Center (SWPC) (formerly the Space Environment Center (SEC)). They provide forecasts and warnings to a number of different users, both companies and individuals. SWPC is part of the National Weather Service (NWS), which is also responsible for forecasts and warnings of terrestrial weather. In turn, NWS is part of the National Oceanic and Atmospheric Administration (NOAA). One of the largest users of forecasts from SWPC is NASA, which needs detailed forecasts for its satellites and manned space missions. Besides NASA, the biggest users are power companies, airlines, the military forces, amateur radio users and companies within the satellite business. The RWC in Boulder coordinates the data exchange and forecasts to the other RWCs around the world.

3.1 Magnetosphere and ionosphere

The geomagnetic field at the Earth's surface can be approximated by a dipole field, whereas further from the Earth it is distorted by the solar wind. The terrestrial magnetic field

deflects the solar wind around the Earth creating a cavity, a "magnetic bubble", called the magnetosphere. The magnetopause is the boundary between the Earth's magnetic field and the solar wind as shown in Figure 3.1. This magnetospheric cavity is formed because the fast moving solar wind, with its magnetic field, cannot penetrate the magnetopause.

The solar wind continuously blows out from the Sun. When this high speed magnetised plasma meets the Earth's magnetic field it first forms a bow shock at a distance of about ten times the Earth's radius. The solar wind pushes the magnetic field up against the day side of the Earth and drags it into a long tail on the night side. Since the magnetosphere is not shaped like a sphere the term instead refers to a region where plasma processes are dominated by the Earth's magnetic field (e.g. Campbell (2003)).

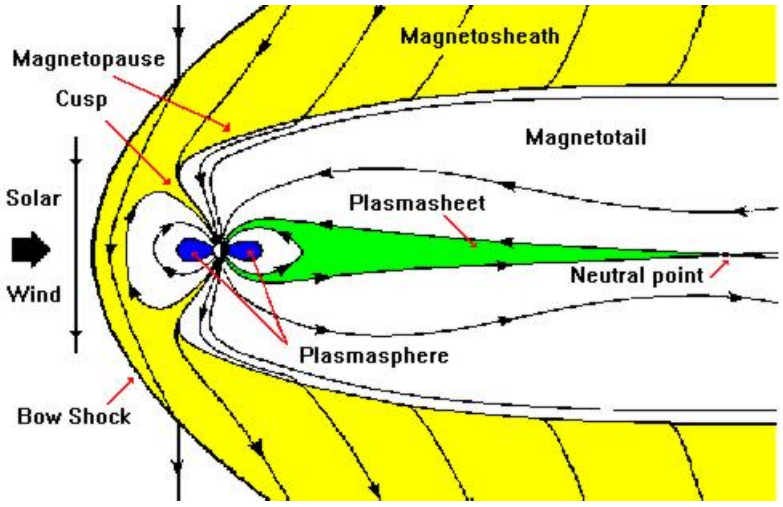

Figure 3.1: Schematic view of the Earth's magnetosphere (Courtesy NASA/GSFC).

The deformation of the Earth's magnetic field generates current systems within the magnetosphere (e.g. Cowley (2000)). Basically, there are five currents in the magnetosphere: the magnetopause current, the tail current, the ring current, field aligned currents and ionospheric currents.

The ionosphere consists of ionised molecules produced by UV radiation, energetic particles and solar X-rays. There are two main current systems in the polar ionosphere: the eastward electrojet (in the morning sector) and the westward electrojet (in the evening sector). The westward electrojet current depresses the northward geomagnetic field at high latitudes. During substorms (see below) auroral activity increases as well as the ionospheric current flow.

3.2 Geomagnetic storms and substorms

Sometimes energetic particles in the solar wind manage to penetrate into the magnetosphere. In particular, this happens when the solar wind magnetic field component B_z has an opposite direction compared to the Earth's magnetic field. This is called magnetic reconnection. The solar wind magnetic field lines then become linked together with the magnetosphere and particles can enter. Particles may also enter the magnetosphere through the polar cusps. During reconnection there is a magnetic erosion on the dayside magnetosphere leading to an accumulation of magnetic fields in the night side magnetotail region. With subsequent reconnection in the tail, plasma is injected into the night side of

the Earth at high-latitudes. At these times auroras can often be seen.

A geomagnetic storm is a global disturbance in the Earth's magnetic field lasting typically from a few hours to a few days (Gonzalez et al. (1994)). The cause of a geomagnetic storm can be the arrival of a high-speed solar wind from a coronal hole or a CME. The most intense geomagnetic storms are usually produced by fast CMEs, especially during the solar maximum. A fast CME with a southward magnetic field direction is more likely to transfer much more energy to the magnetosphere. The amount of energy transferred is also related to the solar wind speed and density. During the declining phase of the solar cycle, recurrent activity from coronal holes is responsible for moderate geomagnetic activity every 27 days. The top three panels in Figure 3.2 show solar wind measurements from the ACE spacecraft during the Halloween events.

A geomagnetic storm is usually divided into three phases: the initial phase, the main phase and the recovery phase. During the initial phase, or sudden commencement, the magnetosphere is compressed on the day side leading to an increase in the magnetic field strength at the Earth's surface. Next, during the main phase, protons and electrons injected from the magnetotail start to drift around the Earth. This "ring current" causes a magnetic field with a direction opposite to the Earth's magnetic field resulting in a depression of the field strength. Finally, during the recovery phase the ring current slowly disappears and the geomagnetic field returns to a quiet time value.

A substorm is another type of geomagnetic disturbance that varies on shorter time scales, of the order of one hour, than those typical of a geomagnetic storm. Substorms are triggered by reconnection in Earth's magnetotail. They are observable mainly in polar regions, at magnetometer stations, and in connection with rapid auroral intensification. Geomagnetic storms often appear to be the superposition of many substorms.

The auroral oval is the "ring" where auroras exist. During a substorm the auroral oval expands, both equatorward and poleward from solar wind energy input. The auroral zone is the area of maximum auroral occurrence at the Earth's surface around 65^0 latitude.

Geomagnetic indices are used to give a simple description about the magnetospheric and ionospheric activity. Two of the most widely used indices are Dst and AE. They are related to the ring current and the magnetotail current (Dst), and to the auroral electrojet current (AE), respectively. These indices together with the Kp index are shown in Figure 3.2. Different geomagnetic indices are presented by Mayaud (1980). The indices used in this thesis are discussed in Chapter 4. An analysis of geomagnetic storms and geomagnetic indices, together with effects on technological systems, was carried out in paper **B**.

3.3 Geoelectromagnetic fields at the Earth's surface

During a geomagnetic storm electrojets are generated in the ionosphere, at an altitude of about 100 km, reaching up to several million Amperes. When these currents change in time geoelectric fields are, according to Faraday's law of induction, induced at the surface of the Earth and in the ground.

In theory, the electric field can be calculated, using Maxwell's equations and boundary conditions, due to a general three-dimensional magnetospheric-ionospheric current system (Häkkinen and Pirjola (1986)). In practice, however, an appropriate method to determine the geoelectric field is to use ground-based geomagnetic data and the plane wave relation between the horizontal electric ($E_{x,y}$) and magnetic fields ($B_{x,y}$) (Viljanen et al. (2004)):

$$E_x(\omega) = Z(\omega)B_y(\omega)/\mu_0,\ E_y(\omega) = -Z(\omega)B_x(\omega)/\mu_0 \tag{3.1}$$

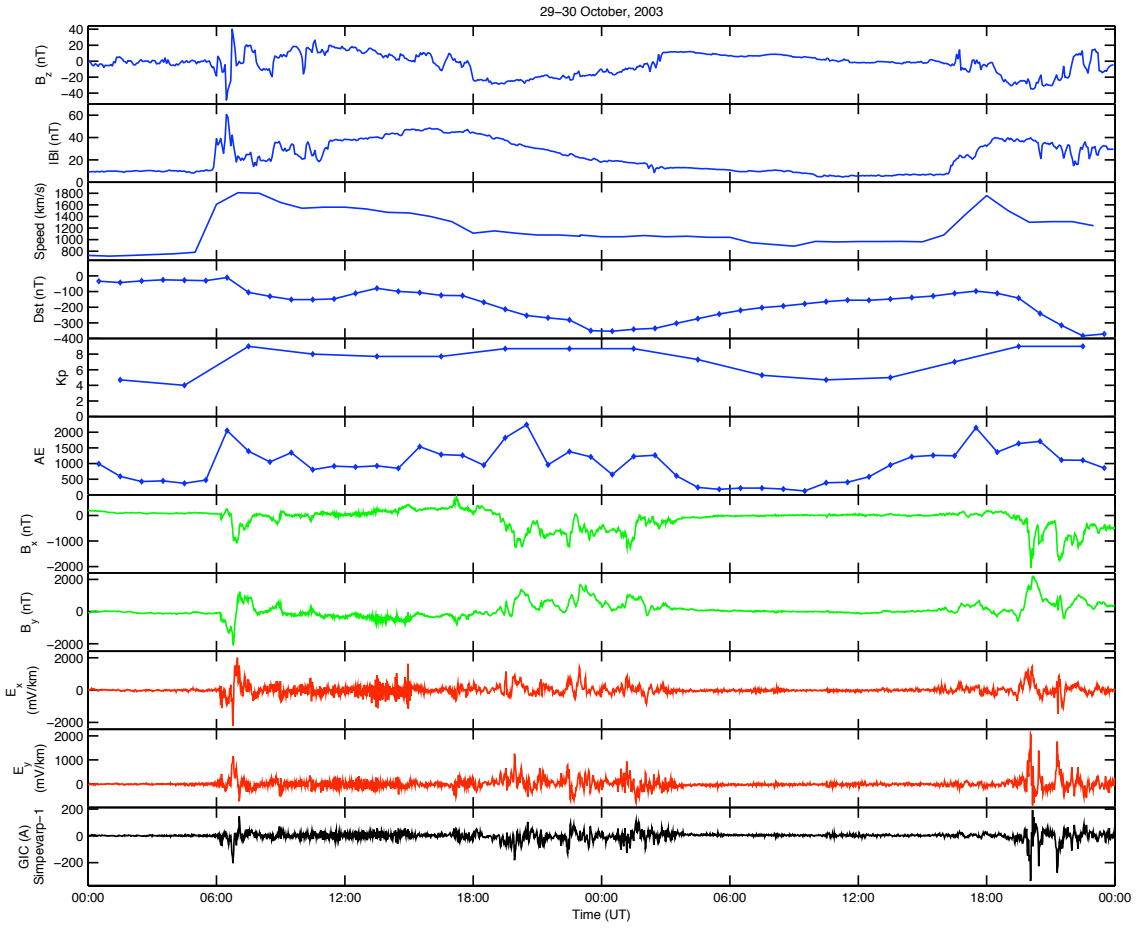

Figure 3.2: Stack plot of ACE solar wind data, geomagnetic indices, horizontal geomagnetic and geoelectric data and geomagnetically induced currents for 29–30 October, 2003. The top three panels show the solar wind B_z component and magnetic field magnitude $|\mathbf{B}|$ from ACE/MAG and helium ion bulk speed from ACE/SWICS. The next three panels present the Dst, Kp and AE indices. The following four panels show the interpolated geomagnetic field (B_x and B_y) and calculated geoelectric field (E_x and E_y) for a site in southern Sweden. The bottom panel presents calculated GIC at the station Simpevarp-1 in southern Sweden. These data sets are also described in paper **B**.

where $Z(\omega)$ is the surface impedance characterizing the ground conductivity structure in the area considered and μ_0 is the vacuum permeability (e.g. Kaufman and Keller (1981)). The x, y and z coordinates refer to the northward, eastward and downward directions, respectively. Usually, as in Equation 3.1, the surface impedance is defined in the frequency domain (ω = angular frequency). Inverse Fourier transforming Equation 3.1 results in a convolution relation between the electric and magnetic fields (Pirjola et al. (2008)).

It is implicitly assumed in Equation 3.1 that the electric and magnetic fields have no spatial dependence in the area considered, i.e. the "plane wave case" is referred to. Assuming that the Earth has a uniform or a multilayered structure, the electric and magnetic fields constitute upward and downward propagating plane waves in the layers, except for the lowermost half-space that only includes a downward wave. Based on the fact that the tangential components of the electric field and the magnetic **H** field (= **B** divided by the permeability) are continuous at the layer boundaries, a recursive formula for the surface

impedance can easily be derived (e.g. Kaufman and Keller (1981)). It is used for a two-layer Earth model in papers **A** and **B**. In the most simple case of a uniform Earth $Z(\omega)$ equals $\sqrt{i\omega\mu_0/\sigma}$ where σ is the ground conductivity. In geoelectromagnetic studies, the Earth's permeability can be assumed to be equal to the vacuum value μ_0.

It was pointed out that the electric and magnetic fields appearing in Equation 3.1 do not depend on the spatial coordinates. Nevertheless, the equation is applicable locally, so that the electric field, the magnetic field and the surface impedance may vary from one site to another. This technique, called the "local plane wave method" (see Viljanen et al. (2004)), is utilised in papers **A** and **B**.

To derive GIC in a network we need the geoelectric field. However, there are very few recordings of the geoelectric field. Measuring the geoelectric field is technically quite simple but difficult to interpret, due to man-made disturbances and the variability of the ground conductivity. Also, a measured geoelectric field only represents a local field (e.g. Viljanen et al. (2004)). The geomagnetic field is, however, available from many magnetic observatories around the world. Also, it is not so sensitive to local ground conductivity anomalies. The geomagnetic field is measured by a magnetometer. The most common type is the fluxgate (or saturable core) magnetometer for directional (vector) geomagnetic field measurements (see e.g. Campbell (2003)). The aim then is to relate the measured geomagnetic field, $B_{x,y}(t)$ to the horizontal geoelectric field $E_{x,y}(t)$ at the Earth's surface (Equation 3.1).

Unfortunately, measured geomagnetic data are seldom available from a dense array of stations. The data have to be interpolated onto a grid covering the region in question (see Figure 3.3). This can be done in many ways. The simplest method would be to use a linear interpolation. It would, however, not necessarily result in a physically acceptable magnetic field, i.e. in field expressions that satisfy Maxwell's equations. Therefore we use the method of Spherical Elementary Current Systems (SECS) in this study (Amm (1997); Amm and Viljanen (1999)). The basic idea of SECS is to divide the magnetospheric-ionospheric current system into divergence-free and curl-free parts and to note that the former can explain magnetic field data recorded on the ground. Therefore, the divergence-free elementary systems constitute equivalent ionospheric currents. They can be determined by utilising ground-based magnetic recordings and then used to calculate the (interpolated) magnetic field at any point at the Earth's surface. An additional feature is that SECS elements may also be placed within the Earth to describe the induction in the Earth (Pulkkinen et al. (2003)). In this study, however, we do not need a magnetic field separation but just the total horizontal field on a dense grid covering southern Sweden. Therefore SECS elements are only assumed to be located in an ionospheric shell. (It should be noted that in order to interpolate the vertical magnetic field properly, currents in the ground should be included as well, though this is not required now.)

Besides SECS, there are also other methods to be applied to the determination of ionospheric equivalent currents. These include the Spherical Cap Harmonic Analysis (SCHA) (Haines (1985)) and the Fourier method (Mersmann et al. (1979)). However, all of them have some drawbacks as compared to SECS. One of them is that, though being only equivalent, the SECS currents also give direct insight into real physical currents in the ionosphere. This is utilised in paper **B**, which investigates properties of the ionospheric electrojet during the magnetic storm in October 2003. Contrary to SCHA and any other techniques based on expansions of the magnetic field in terms of harmonic functions, it is not necessary in SECS to specify the shortest wavelength to be included globally, but we may freely choose the positions of the SECS elements. This means that SECS can be adapted both according to the locations of the available ground-based magnetometers

available and regarding the grid onto which the field is calculated. An example of the interpolated horizontal geomagnetic and calculated horizontal geoelectric field based on SECS is shown in Figure 3.2.

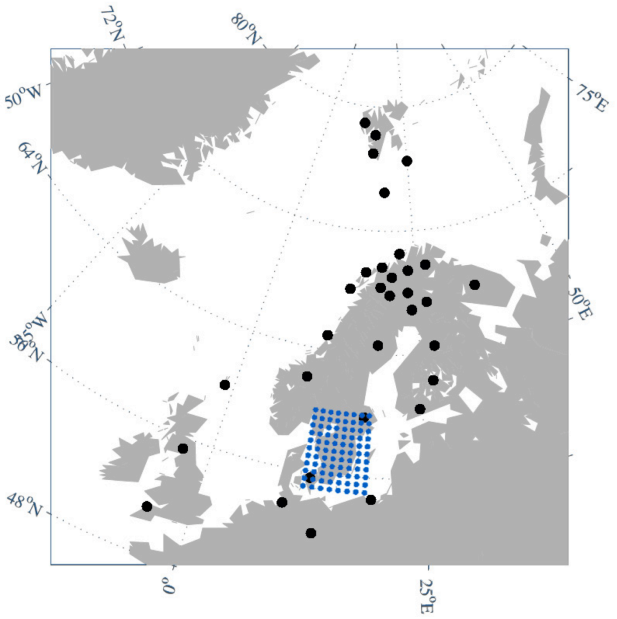

Figure 3.3: Magnetometer stations (black) and a dense grid for the interpolation (blue) in southern Sweden. The observatories in the SW and NE corners of the grid are Brorfelde and Uppsala (from paper **A**).

At magnetic observatories, the magnetic field is usually described by the XYZ coordinate system with the three orthogonal components X (north), Y (east) and Z (vertical into the Earth). The geomagnetic field can be divided into different contributions as follows

$$\begin{aligned} \mathbf{B}_{total} &= \mathbf{B}_{quiet} + \mathbf{B}_{disturbed} = \\ &= (\mathbf{B}_{dynamo} + \mathbf{B}_{regional} + \mathbf{B}_{local}) + (\mathbf{B}_{primary} + \mathbf{B}_{secondary}) \end{aligned} \tag{3.2}$$

where $\mathbf{B}_{quiet}$ and $\mathbf{B}_{disturbed}$ are the "baseline" field and the disturbance part, respectively. The fields $\mathbf{B}_{dynamo}$, $\mathbf{B}_{regional}$, and $\mathbf{B}_{local}$ are related to the Earth's dynamo, crustal anomalies and magnetised rocks. The fields $\mathbf{B}_{primary}$ and $\mathbf{B}_{secondary}$ are related to ionospheric/magnetospheric currents and currents induced in the ground (telluric currents). Geomagnetic variations ($d\mathbf{B}_{disturbed}/dt$), the only related to GIC effects, are of the order of 2500 nT/min in maximum (Viljanen (1997)). The quiet time baselines, for $\mathbf{B}_{disturbed}$, are selected from case to case. The total field, $|\mathbf{B}_{total}|$, in southern Sweden is about 50000 nT.

3.4 Geomagnetically induced currents

The geoelectric fields drive currents in the ground and in man-made conductor networks, such as power grids, communication cables, oil and gas pipelines and railway equipment. A common name for these currents is geomagnetically induced currents (GIC) and they are the ground end of the space weather chain. GIC are mainly (but not only) a high-latitude

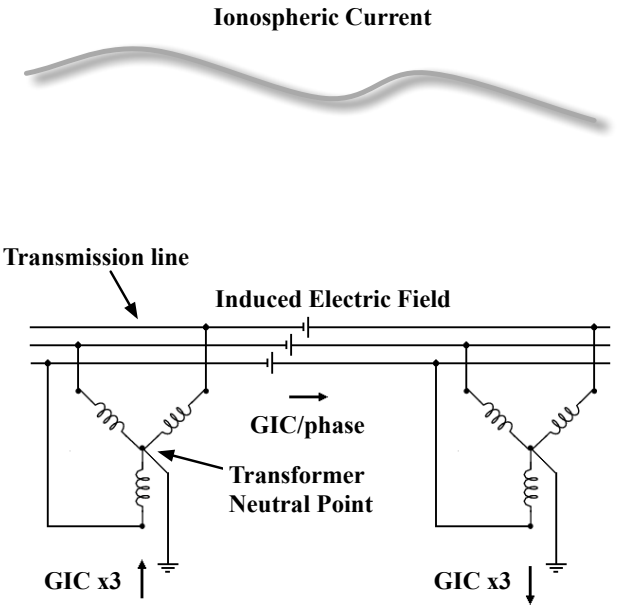

Figure 3.4: GIC flowing along the transmission line between two transformers. A time-varying ionospheric current, i.e. the primary driver of GIC, is also schematically shown. (from paper **A**)

phenomenon since geomagnetic disturbances and geoelectric fields are the largest and most frequent in these areas.

The power industry is perhaps the branch that has had most problems with GIC. A power grid consists of 3-phase transmission lines with "Y"- or "Delta"-connected transformers. The former transformer type always has a grounding whereas the latter does not. During normal loads the currents add up to zero at the neutral point. The earthing offers a path for GIC to enter the power grid. The currents flow along the transmission lines and then back to the ground at other transformer stations. Compared to the 50/60 Hz frequency used for household electricity, GIC can be treated as a direct current (< 1 Hz). A schematic GIC path between two transformers is shown in Figure 3.4.

The problems arise when the flow of GIC in the transformer winding creates a DC magnetic field that can lead to saturation of the core. This results in a non-linear operation of the transformer. The magnetising current increases during every half-cycle resulting in an excessive amount of harmonics. In a saturated transformer, the magnetic flux can spread out through structural members producing eddy currents, which in turn may cause hotspots, possibly with permanent damage. Protective relays may malfunction resulting in parts of the system being disconnected. Together with increased reactive power demands these effects may cause a collapse of the whole system. The degree of disturbance depends on several factors, such as the geographical location of the power grid, the ground conductivity, the design of the grid and the transformers and the load situation (e.g. Lindahl (2003)). GIC research has been, and still is, important especially in Canada, USA, Finland and Sweden due to their location at active auroral latitudes. But studies at low latitudes, like South Africa are also of interest (Koen and Gaunt (2002)).

In 13–14 March 1989, a geomagnetic storm caused a blackout in the Hydro-Québec power grid in Canada. About 6 million people were left without power up to 9 hours (Bolduc (2002)). GIC events have also occurred many times in Sweden, the latest during the "Halloween storm", on 29–30 October 2003. The result was a blackout in the city

of Malmö affecting 50000 customers and lasting almost an hour (see paper **B**; Lundstedt (2006b); Lindahl (2003); Pulkkinen et al. (2005)). Calculated GIC in a transformer neutral at the OKG nuclear power plant in southern Sweden is shown in the bottom panel of Figure 3.2.

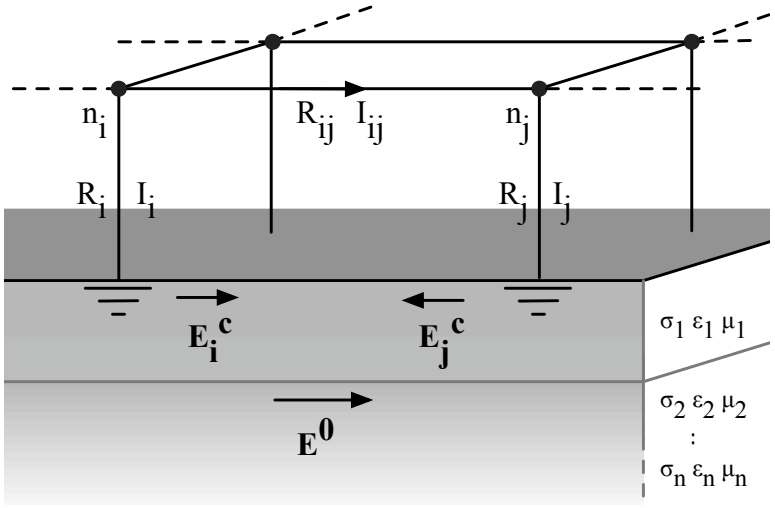

Figure 3.5: Schematic view of two nodal points, n_i and n_j, in a part of an earthed conductor network together with a cut-away view of the ground layers.

When the geoelectric field at the Earth's surface is known the calculation of currents in the system is straightforward and can in principle be carried out exactly based on Ohm's and Kirchhoff's laws and on Thévenin's theorem. GIC flowing in a power network will be divided equally between the three phases. The following calculation technique of GIC is based on Lehtinen and Pirjola (1985).

A schematic picture of (a part of) a grounded conductor network (e.g. a power grid) is shown in Figure 3.5. The network consists of nodal points $n_1, .., n_i, n_j, .., n_m$ that are earthed with earthing resistances $R_1, .., R_i, R_j, ..., R_m$. Between two nodal points, e.g. n_i and n_j, a connection may exist with a resistance R_{ij}.

We assume that the horizontal induced geoelectric field, $\mathbf{E^0}$, is known at the Earth's surface. The geovoltage between the nodal points n_i and n_j, along path s_{ij} directly below the conductor, is then equal to

$$V_{ij}^0 = \int_{s_{ij}} \mathbf{E^0} \cdot \mathbf{ds} \tag{3.3}$$

This "battery" for GIC must be treated as an induced voltage in the network conductor and not in the ground since the geoelectric field is not a potential field (Boteler and Pirjola (1998); Pirjola (2000)).

When computing GIC, both the electric field and the voltage are considered to be independent of time, which thus means a DC treatment. That is, for each time step, t, the voltage (and GIC) can be calculated from the electric field at the same time t.

The earthing currents, I_i, at each nodal point can be derived by utilising Kirchhoff's current law

$$I_i = \sum_{j \neq i, j=1}^{m} I_{ji} \tag{3.4}$$

where I_{ij} is the current (in the transmission line) from n_i to n_j. Finally, the earthing current vector $\mathbf{I}$, with elements I_i, is equal to

$$\mathbf{I} = (\mathbf{1} + \mathbf{YZ})^{-1}\mathbf{J} \tag{3.5}$$

where the (symmetric) network admittance matrix $\mathbf{Y}$ is determined by the resistances, R_{ij}, of the conductors between the nodal points. The (symmetric) earthing impedance matrix $\mathbf{Z}$ couples the currents flowing between the network and the earth to the voltages of the nodal points with respect to a remote earth. The diagonal elements of $\mathbf{Z}$ are equal to the earthing resistances, R_i, of the nodes. If the nodes are distant enough, the off-diagonal elements of $\mathbf{Z}$ are zero. The elements in $\mathbf{Z}$ and $\mathbf{Y}$ are real due to the DC treatment.

The column matrix $\mathbf{J}$ gives the earthing currents in the case of perfect earthings, i.e. when $\mathbf{Z}$=0. The elements depend on the conductor resistances and on the geovoltages obtained from Equation 3.3.

In GIC calculations for a real power system, the three phases are usually treated as one circuit element with a resistance one third of that of a single phase. For convenience, the (total) earthing resistances of the stations are defined to include the actual earthing resistances, the transformer resistances and the resistances of possible neutral point reactors (or any other resistors) in the earthing leads of transformer neutrals (all resistances in series). In case of several parallel transformers at a station, they are handled as one element. If two different voltage levels are included in a GIC calculation, special treatments are needed (see e.g. Pirjola (2005)). In papers **A** and **B** we take the 130 kV level into account in computations of GIC in the southern Swedish 400 kV network by approximately decreasing the earthing resistance values at stations with autotransformers.

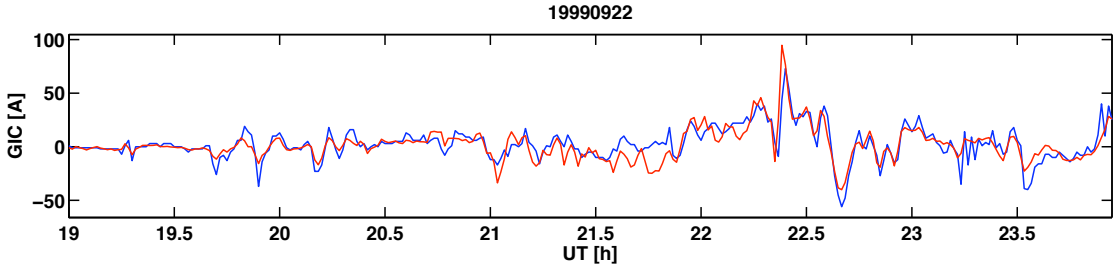

Figure 3.6: Measured (blue) and calculated GIC, at a transformer neutral in southern Sweden, for an event on 22 September 1999. (from paper **A**)

An example, from paper **A**, of calculated GIC and measured GIC for an event is shown in Figure 3.6.

Chapter 4

Data

Many different types of data sets have been used in the papers contributing to this thesis. The data include indicators of solar activity, the solar magnetic field, solar wind parameters, geomagnetic indices, the geomagnetic and geoelectric field, power system data, and geomagnetically induced currents (GIC). Additional data and information were taken from e.g. Solar-Geophysical Data Prompt Reports and Comprehensive Reports (published by NOAA National Geophysical Data Center, Boulder, USA). The data sets are summarised in Table 4.1, and described in more detail in the following sections.

Table 4.1: All data sets used in this thesis.

Data set	Available at:
Sunspot number R_z	http://sidc.oma.be/DATA/dayssn_import.dat
Group sunspot number R_g	ftp://ftp.ngdc.noaa.gov/STP/SOLAR_DATA /SUNSPOT_NUMBERS/GROUP_SUNSPOT_NUMBERS/
Sunspot area SSA	http://solarscience.msfc.nasa.gov/greenwch.shtml
Total solar irradiance TSI	ftp://ftp.ngdc.noaa.gov/STP/SOLAR_ DATA/SOLAR_IRRADIANCE/composite d25 07 0310a.dat
Solar magnetic field WSO synoptic charts	http://wso.stanford.edu/synopticl.html
Solar wind data IMP8	http://www-ssc.igpp.ucla.edu/forms/imp8_form.html
Solar wind data ACE	http://www.srl.caltech.edu/ACE/ASC/level2/index.html
Solar wind data SOHO	http://seal.nascom.nasa.gov/cgi-bin/gui_plop
Solar wind data WIND	http://www-ssc.igpp.ucla.edu/forms/polar/corr_data.html
Geomagnetic field IMAGE	http://www.space.fmi.fi/image/
Geomagnetic field INTERMAGNET	http://www.intermagnet.org/
Geomagnetic activity indices Dst and Kp	http://spidr.ngdc.noaa.gov/spidr/index.jsp
Geomagnetic activity index AE	http://swdcwww.kugi.kyoto-u.ac.jp/wdc/Sec3.html
Power grid data	Svenska Kraftnät (SVK) power company
Geomagnetically induced current GIC	Oskarshamns kraftverksgrupp (OKG), E.ON, Sweden

4.1 Indicators of solar activity

The relative sunspot number R_z was created in 1848 by J. R. Wolf at the Zürich Observatory (Waldmeier (1961)). But already in 1842, H. Schwabe had noticed that the number of spots varies with a period of about 11 years (Schwabe (1843)). The sunspot number is a rough measure of the total magnetic flux within the sunspots (Zharkov and Zharkova (2006)). Since 1981 an International Sunspot Number is derived at the World Data Center (SIDC) for sunspots in Brussels, Belgium (Vanlommel et al. (2005)). To guarantee continuity with older data, the same reference station, in Locarno (Switzerland), is used. The sunspot number is derived as a weighted mean of sunspot numbers observed at a number of solar observatories around the world. It is given by

$$R_z = k(10G + S) \tag{4.1}$$

where S represents the number of observed sunspots, G the number of observed sunspot groups and k the quality factor dependent on the observer.

The group sunspot number, R_g was constructed by Hoyt and Schatten (1998), as an alternative to the international sunspot number. It is given by

$$R_g = \frac{12.08}{N} \sum_{i=1}^{N} k_i G_i \tag{4.2}$$

where G_i is the number of sunspots, k_i is the ith observers correction factor and N the number of observers. The data can be obtained from NOAA's National Geophysical Data Center.

The sunspot area data, SSA, goes back to 1874 and is obtained from NASA. It is derived as the total area of sunspots in units of millionths of a hemisphere. Data after 1976 include a correction factor.

The total solar irradiance, TSI, is the radiant energy (W/m^2) measured outside the Earth's atmosphere. It describes the emitted radiation from the Sun over all wavelengths. The composite TSI data set is assembled from six different satellite observations covering the period 1978 to present (Fröhlich and Lean (1998)) and are obtained from NOAA's National Geophysical Data Center.

The data sets in this section are used in paper **D**.

4.2 Solar magnetic field

The solar magnetic field data are collected at the John M. Wilcox Solar Observatory (WSO) at Stanford University. Daily values are used. The WSO synoptic charts were calculated from the line-of-sight photospheric magnetic fields, of 3 arcmin resolution, observed at WSO (Scherrer et al. (1977); Hoeksema (1985)). The WSO data cover three cycles from 1976 (CR 1642) up to 2007 (CR 2065). The data for each Carrington rotation consist of 72x30 values (longitude and latitude). The magnetograph uses a wavelength of 525.02 nm (Fe I). This data set is used in paper **E**.

4.3 Solar wind data

The IMP8 (Interplanetary Monitoring Platform 8) satellite was launched by NASA on 26 October 1973. It was designed to measure magnetic fields, plasma parameters, and energetic charged particles of the Earth's magnetotail and magnetosheath and the near-Earth solar wind (King (1982)). For each orbit around the Earth, the spacecraft spend seven to eight days in the solar wind, and about four to five days in the magnetosheath and magnetosphere. IMP8 data consist of solar wind magnetic B_z component, from the MAG instrument, and solar wind density and the speed, from the MIT Faraday cup plasma instrument (P.I. for these instruments are R. P. Lepping (NASA/GSFC) and A.J. Lazarus (MIT)). The IMP8 data are available from the Space Science Center at UCLA. This data set is used in paper **B**.

The Advanced Composition Explorer (ACE) spacecraft, launched on 25 August 1997 by NASA, is in orbit around the L1 libration point about 1.5 million km from Earth and 148.5 million km from the Sun. ACE measures the solar wind, the interplanetary magnetic

field and higher energy particles accelerated by the Sun, as well as particles accelerated in the heliosphere and in galactic regions beyond. The ACE data are available in real time. Data from the following instruments are used: Solar Wind Electron Proton Alpha Monitor (SWEPAM) (McComas et al. (1998)), the ACE Magnetic Field Experiment (MAG) (Smith et al. (1998) and the Solar Wind Ion Composition Spectrometer (SWICS) (Gloeckler et al. (1998)). The ACE data are available from the Space Radiation Lab at the California Institute of Technology. These data sets are used in papers **B** and **C**.

Solar wind density and velocity data are also collected by the Solar Wind Experiment (SWE) onboard the WIND spacecraft (Ogilvie et al. (1995)). This data are available from the MIT Space Plasma Group. Solar wind magnetic field data are measured by the Magnetic Field Investigation (MFI) instrument (Lepping et al. (1995)). WIND was launched on 1 November 1994 and is also in orbit around L1. This data set is used in paper **C**.

The Solar and Heliospheric Observatory (SOHO) is a project of international collaboration between ESA and NASA to study the Sun from its deep core to the corona and the solar wind. SOHO was launched on 2 December 1995. Solar wind data consist of density and velocity measurements by the CELIAS/MTOF (Mass Time-Of-Flight) proton monitor (Ipavich et al. (1998)). The data are available from the University of Maryland. This data set is used in paper **C**.

4.4 Terrestrial data

The geomagnetic field is recorded continuously at several sites in northern Europe. They include the IMAGE magnetometer array sites and INTERMAGNET stations (Syrjäsuo et al. (1998); Kerridge (2001)). The magnetic field is often described by using the XYZ-component representation. In this (local) coordinate system, the three orthogonal field directions are geographical northwards and eastwards, and downwards into the Earth. Another representation is the HDZ-component coordinate system, with the components H (horizontal), D (declination), and Z (downwards into the Earth) (Campbell (2003)). IMAGE and INTERMAGNET data can be obtained from FMI and from the INTERMAGNET websites. Geomagnetic field data are used in paper **A**, **B** and **C**.

Geomagnetic activity indices are used to characterise the dynamics of the magnetosphere and iononsphere (Mayaud (1980)). The indices are based on recorded magnetograms from magnetic observatories around the world. The Kp index is one of the most used geomagnetic indices (Bartels et al. (1939)). It is based on the local K index, which is defined by the largest variation in a 3-hour interval in X (or H) and Y (or D). The purpose of Kp is to characterise the worldwide geomagnetic activity. The Kp values are derived using K values from 11 stations. The Kp scale is divided into 28 levels, in steps of 1/3, from 0 to 9. Major geomagnetic storms have Kp values between 8 and 9 (Campbell (2003)). The hourly Dst index (storm-time disturbance) is a measure of the strength of the ring current around the Earth. It is derived from an average of the H components at four stations evenly distributed around the Earth along the magnetic equator, with adjustments for quiet day levels and latitude (Sugiura (1964)). The 1-hour auroral electrojet index, AE, was developed as an indicator of the geomagnetic activity produced by ionospheric currents within the auroral oval in the northern hemisphere (Davis and Sugiura (1966)). A chain of magnetometers in the auroral zone is used. First, the H components for all observatories, corrected for quiet day values, are plotted in a single plot. Next, for each time step, the highest and lowest H values are determined. The largest positive values are defined as the AU index (auroral upper index), and the lowest negative values are defined as the AL

index (auroral lower index). The AE index is finally defined as AE=AU-AL. The Dst and Kp indices can be downloaded from the Space Physics Interactive Data Resource (SPIDR) within the NOAA National Geophysical Data Center in Boulder, USA. The AE index can be downloaded from the World Data Center for Geomagnetism in Kyoto. Geomagnetic indices are included in paper **B**.

The power grid data, which refer to the southern Swedish 400 kV system, were obtained from the Svenska Kraftnät (SVK) power company. The data include the station coordinates, the network topology, the transformer resistances, the transmission line resistances and the station earthing resistances. At some stations the 400 kV network is connected to the 130 kV system by autotransformers. The grid data contains 22 stations and 24 lines. This data set is used in papers **A** and **B**.

Measurements of geomagnetically induced currents (GIC) are provided by Oskarshamns kraftverksgrupp (OKG), a company within E.ON, Sweden. GIC have been recorded in the Swedish 400 kV power system since 1998. The recordings take place in transformer neutrals, at the eastern coast close to the nuclear power plant OKG in Oskarshamn. Measured GIC data were recorded instantaneously every minute, from 1998 to 2000. At the end of 2000, a resistor was installed in the earthing lead of the transformer neutral to efficiently decrease GIC. GIC measurements, with 1-min instantaneous values, are still in operation. The geographical coordinates of OKG and the measurement site are approximately 57.4 N and 16.7 E. GIC data are used in papers **A** and **B**.

Chapter 5

Analysing methods

Two different mathematical tools have been used extensively in the papers presented in this thesis. The first method is wavelet analysis and the second is neural networks.

5.1 Wavelet analysis

Wavelet analysis is today a common method in studies of solar-terrestrial data. A new approach for exploring, understanding and predicting solar activity, using wavelets and neural networks, was introduced in Lundstedt (2006a). These wavelet methods were applied to solar activity indicators by Lundstedt et al. (2005). Wavelet analysis of solar activity indicators have also been performed by e.g. Frick et al. (1997), Ippolitov et al. (2002), Ballester et al. (2002) and Moussas et al. (2005).

A wavelet is basically a function with zero mean that is localised in both time and frequency. In comparison, the basis functions sine and cosine in the Fourier analysis are only localised in frequency. There are also an infinite number of basis functions in the wavelet transform (see e.g. Addison (2002)). The wavelet analysis is useful for investigating signals that are for example aperiodic and contain transients. The wavelet transform uses a "local" waveform called a wavelet, to transform the signal into a more useful form. The wavelet transform is defined mathematically as the convolution of the signal with the wavelet function. There are many types of wavelets, e.g. Morlet, Mexican Hat and Daubechies, both real and complex. The "mother wavelet" can be changed in two ways. It can be moved along the signal (translated), to location b, and it can be stretched or compressed (dilated), using the scale a. A low scale, i.e. a compressed wavelet, corresponds to a high frequency and a high scale, i.e. a stretched wavelet, corresponds to a low frequency.

The wavelet transform is calculated for different translation and dilation values creating a continous wavelet transform (CWT) or, for discrete steps, a discrete wavelet transform (DWT). The wavelet transform is sometimes called a "mathematical microscope", where b is the location of the study, and a the magnification at this location.

The wavelet transform of a signal x returns the wavelet coefficients $C(a, b)$. If the coefficients are large there is a local matching between the signal and the wavelet at this particular scale and position. This concerns both the continuous and the discrete wavelet transform.

The continuous wavelet transform of a time series $x(t)$ is defined as

$$C(a,b) = \frac{1}{\sqrt{a}} \int_{-\infty}^{+\infty} x(t)\psi^*(\frac{t-b}{a})dt \tag{5.1}$$

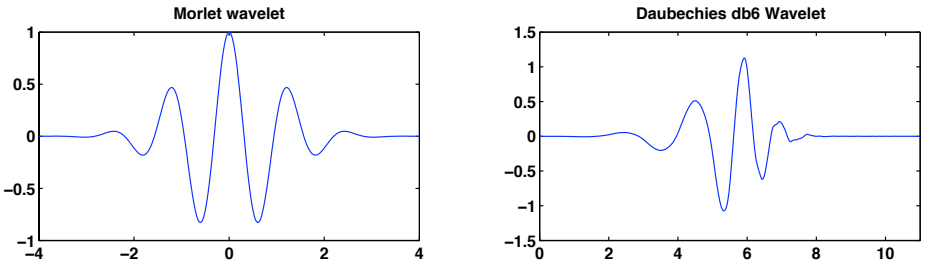

Figure 5.1: Morlet and Daubechies wavelets.

where ψ is the wavelet, a continuous function of both time and frequency, b is the translation parameter, a is the scale parameter and $*$ represents complex conjugate. The discrete wavelet transform is the same but only discrete values for a and b are used, where $a = 2^j$ and $b = k2^j$ $(j, k \in Z)$ .This is called a dyadic grid scaling.

In a multiresolution analysis, the time series are decomposed into approximations and details using the discrete wavelet transform (DWT).

The detail D_j at level j is calculated as

$$D_j(t) = \sum_{k \in Z} C(j,k)\psi_{j,k}(t) \tag{5.2}$$

where $\psi_{j,k}$ is the wavelet, and $C(j,k)$ are the wavelet coefficients. A signal $x(t)$ is the sum of all the details. By choosing a reference level J, the signal is equal to the approximation A_J and the sum of the details D_j

$$x(t) = \sum_{j \in Z} D_j = \sum_{j \leq J} D_j + A_J \tag{5.3}$$

where the level j goes from 1 to J. The approximations are related to one another by

$$A_{J-1} = D_J + A_J \tag{5.4}$$

A version of DWT is called the maximal overlap DWT (MODWT) (see Percival and Walden (2002)). The main difference of the MODWT is that the transform is invariant under temporal shifts. Multiresolution analysis is used in paper **E**, and the MODWT is used in paper **D**. The Daubechies *db*6 (where 6 is the order) wavelet, together with the Morlet wavelet, is shown in Figure 5.1.

5.2 Neural networks

Neural networks are based on the architecture of the human brain. The human brain contains about 10 billion nerve cells, or neurons, that are connected to other neurons. This network forms a massively parallel information processing system compared to a single computer processor, that executes a single series of instructions.

While the neurons in the brain are slow compared to a computer processor, it is able to process many tasks at the same time. Neural networks are trained, for example, to recognise patterns, classify data and predict. There are many types of neural network designs and neuron models. For feed-forward networks the outputs are functions of the inputs only. For recurrent networks, however, the output is a function of time (Haykin (1998); Hagan et al. (2002)).

It is the arrangement of neurons and the strength of the connections between them that constitute a neural network. Combinations of these result in different neural network designs, or neural network architectures.

In a neuron, all the incoming signals, p_i, are first multiplied with their respective weights w_i. Their sum is then added to an external bias, b. This is called the net input, n. Then, the output signal is derived by applying a transfer function (or activation function), f, to the net input:

$$a = f(n) = f(\sum_i w_i p_i + b) = f(\mathbf{W} \cdot \mathbf{p} + b) \tag{5.5}$$

where a is the output from the neuron, $\mathbf{W}$ the weight vector and $\mathbf{p}$ the input vector. The transfer function, f, must be: differentiable, monotonous rising, limited and non-linear. With several neurons, the output is derived as

$$\mathbf{a} = f(\mathbf{W} \cdot \mathbf{p} + \mathbf{b}) \tag{5.6}$$

where the output $\mathbf{a}$ is a vector, $\mathbf{W}$ is a matrix consisting of weights w_{ij} from input p_i to neuron j, and $\mathbf{b}$ is the bias vector consisting of a bias, b_j, for each neuron. This network consists of only one layer of neurons but it is possible to include more layers.

Transfer functions may be linear or nonlinear functions of the net input. Common functions are e.g. linear ($a = n$), log-sigmoid ($a = \frac{1}{1+e^{-n}}$) and hard-limit ($a = 0, n < 0; a = 1, n \geq 0$).

The most common network design is the multilayer feed-forward. These networks consist of neurons in one layer that are connected to neurons in the next layer. In the first layer, the input layer, the number of neurons is determined based on the number of input variables, whereas the number of neurons in the output layer is determined by the number of target variables. The outputs of each intermediate layer are then inputs to the following layer. It is common for the number of neurons in a layer, except the input layer, to be different from the number of inputs.

In a feed-forward network, the signal (or data), enters the network in the input layer, continues through the hidden layers and then goes to the output layer. This type of a network is often trained by an error-propagation algorithm. The network weights and biases are first initialised. The network is then trained using a set of network inputs p and target outputs t. In the training phase, the weights and biases are updated so that the network outputs move closer to the target values. The average squared error between the outputs a and the target outputs t is then minimised:

$$E = \sum_{s=1}^{N} (t(s) - a(s))^2 \tag{5.7}$$

where N is the total number of training values. In summary, the weights w_{ji} and the biases b_j are adjusted to minimise the error E.

Another common network design is the Elman recurrent neural network (Elman (1990)). It consists of a two-layer backpropagation network together with feedback connections from the output of the hidden layer to its inputs. These feedback connections store values from previous input states to be used in the current input state, simulating a memory. A recurrent network is used in paper **C**.

Chapter 6

Conclusions and outlook

The work presented in this thesis concerns space weather and effects. Papers **A**, **B** and **C** involve ground effects from space weather. These studies are the continuation of the results from the ESA pilot project Service Development Activity (SDA), "Real-time forecast service for geomagnetically induced currents", supported by ESA and ELFORSK. That study was a joint collaboration between the Swedish Institute of Space Physics (IRF) and the Finnish Meteorological Institute (FMI) (Lundstedt et al. (2007)). Papers **D** and **E** are related to proxies of the solar activity and analysis of the large-scale solar magnetic field.

In paper **A** we provide an analysis and a model of GIC for the southern Swedish 400 kV power system. This is the first quantitative modelling of GIC in Sweden and is based on theoretical modelling and measured data. The input to the model is the electric field, derived from geomagnetic data and an adjustable two-layered ground conductivity model. The output from the model was compared to measured GIC from one site. The conductivities of the two layers were adjusted until a satisfactory fit was obtained between measured and calculated GIC. For other sites in the network, we were not able to estimate the accuracy since GIC recordings are not available. From this study, we conclude that for most events the linear correlation between measured and calculated GIC is above $\sim$0.7. However, for a few events, especially the storm in April 2000, the modelled GIC differs greatly from the measured data. It is possible that the temporal resolution of 1 min for the geomagnetic data, during the most extreme parts of the events, is too low. Also, for larger GIC values, modelled GIC appears to be systematically lower than the measured GIC. This is most likely due to the large number of small GIC values in the least-square fit used for the determination of the ground conductivity values. Other reasons, less likely to be significant however, are unknown changes in the power grid or effects of the 130 kV part.

For future studies we plan to use 10 s geomagnetic data and improve the ground conductivity model used for calculating the geoelectric field and GIC. An optimal layered-earth model for GIC studies can be derived using the "optimal modelling technique" (Pulkkinen et al. (2007)). Another issue that should be investigated in the future is the "coast effect", i.e. the determination of the effect of the boundary between the land and the sea on geoelectric fields and GIC in coastal areas. With a new magnetometer being installed closer to the GIC measurement site, we expect to get a better accuracy for the magnetic field. Finally, we should include all voltage levels of the Swedish high-voltage system in our GIC computation model.

In the second paper, **B**, we studied two GIC events, from the Sun to the ground, that occurred in Sweden in July 1982 and October 2003. Around midnight, between 13 and 14 July 1982, the calculated geoelectric field reached values of 3–6 V/km, which is of the same

order as deduced from voltage recordings based on two telecommunication cables close to Stockholm. This was large enough to de-energise a relay in the railway traffic light system and cause a red light to be shown without any train coming. During the events on 28–30 October 2003, two CMEs were responsible for large geomagnetic storms with Kp reaching 9. During the second storm, on 30 October, a blackout occurred in the city of Malmö and lasted for 20 to 50 minutes. It has been confirmed that the cause was a misoperation of a relay in the 130 kV system. The relay was too sensitive to the third harmonics of the fundamental frequency which were a result from transformer saturation due to GIC. Both events, in 1982 and 2003, were probably caused by halo-CMEs. The GIC calculations were based on the model developed in paper **A**. In the storm of July, 1982, the largest time derivative values, around 2500 nT/min, of the ground magnetic field were much stronger than in the October 2003 storm. In the future we plan to investigate, in some more detail, the effects of induced geoelectric fields on railway systems by developing a calculation model applicable to a precise computation of GIC and induced voltages on railways.

In paper **C** we studied the prediction of the 10-min root mean square of variations of the horizontal components of the local ground magnetic field. The prediction model is based on a recurrent neural network and uses the solar wind data from the ACE spacecraft. The study covered the period from 7 to 10 November 2004. The model was developed earlier by Wintoft (2005). However, the model does not take into account the exact location of ACE. Here we compare the prediction results using solar wind data from the L1-spacecrafts ACE, SOHO and WIND. The ACE data show a better agreement to the near-Earth solar wind during the first two days as compared to the last two days. Thus, the accuracy of the predictions depends on the location of the spacecraft and the solar wind flow direction. The response of the model was also studied by artificially changing the sign of the solar wind magnetic field component B_z. Basically, the ΔX model is almost independent of the sign of B_z whereas the ΔY model shows a strong dependence at all times. In a future study we will include more data, including the exact location of the spacecraft.

In paper **D** we analysed the time series: the sunspot number R_z, the group sunspot number, R_g, and the sunspot area, SSA, against the total solar irradiance, TSI, in the context of TSI reconstruction. When no solar magnetic field observations exist, TSI can be reconstructed by SSA, R_z, and R_g instead. Using wavelet analysis, we studied the correlation as function of temporal scale. A strong anti-correlation, around periods of 64 to 128 days, exist between SSA and TSI that may be interpreted as the sunspot dimming effect being dominant in SSA around these time scales. R_z showed a similar relation to TSI but with a weaker anticorrelation. Finally, Rg shows no correlation at intermadiate scales Next we reconstructed TSI using SSA, R_g and R_z by separating the short term from the long term variations. The first reconstruction (one component) is a linear model using only the long term variation of one of the three indices. The three reconstructed TSI series are in reasonable agreement back to about 1880. Going further back in time the differences become larger due to differences between the R_z and R_g series. The second reconstruction of TSI also includes the short term variations, or wavelet details. For SSA, the correlation between the reconstructed and observed TSI now increases from 0.83 to 0.91. For R_z the increase in correlation is smaller, from 0.83 to 0.86. Finally, there is no improvement when the high frequency component is included using R_g. The results show that the trend in observed TSI is completely different from the trends in the reconstructions. This may be explained by the finding that the TSI series have properties that are quite different from all other series of solar indices. This indicates that the reconstruction of TSI is difficult. The reasonably high correlation, up to 0.9, is dominated by the 11-year variation. Correlations above 11 years are difficult to identify based on the available TSI series covering only three

solar cycles.

Finally, in paper **E**, we derived the magnetic butterfly diagram, using multiresolution analysis, from solar synoptic maps from the Wilcox Solar Observatory. Typically, the magnetic butterfly diagram is derived using longitudinally averaged synoptic maps. The average is based on the 27.2753 days that constitute a Carrington rotation. However, the Sun rotates differentially with a rotation rate of about 25 days at the equator and up to about 35 days at the poles. Later we plan to include synoptic maps from e.g. SOHO/MDI and the Kitt Peak observatory. Data from solar subsurface flows and coronal magnetic fields are also of interest. That will give us a 3-D picture of the solar magnetic field. We also plan to use wavelet filtering based on power spectra to find the fundamental scales for each latitude. We will also examine in more detail the effect of the differential rotation on wavelet filtered time series and compare them with data from other instruments and observatories. The final goal is to try to relate these results to various dynamo models and predictions of the magnetic activity.

Improving understanding of solar physics and the solar magnetic activity helps develop space weather forecasting and thus avoid adverse impacts on space-borne and ground-borne technology. There are several challenges in the future related both to the origin of space weather and to the effects from space weather.

Division of work

Paper **A**:

M. Wik, A. Viljanen, R. Pirjola, A. Pulkkinen, P. Wintoft and H. Lundstedt.
Calculation of geomagnetically induced currents in the 400 kV power grid in southern Sweden.

I did all the analysis of the data. I also contributed to the power grid model and the conductivity model. I made all the figures and wrote most of the manuscript.

Paper **B**:

M. Wik, R. Pirjola, H. Lundstedt, A. Viljanen, P. Wintoft and A. Pulkkinen.
Space weather events in July 1982 and October 2003 and the effects of geomagnetically induced currents on Swedish technical systems.

I did all the analysis of the data. I made all the figures and wrote most of the manuscript.

Paper **C**:

P. Wintoft, M. Wik, H. Lundstedt and L. Eliasson.
Predictions of local ground geomagnetic field fluctuations during the 7–10 November 2004 events studied with solar wind driven models.

I was involved in the discussions about the analysis and the neural network model.

Paper **D**:

P. Wintoft, M. Wik, and H. Lundstedt.
Sunspot records as proxy for total solar irradiance.

I took part in the wavelet analysis. I was also involved in the discussions.

Paper **E**:

M. Wik, H. Lundstedt and P. Wintoft.
Multiresolution analysis of synoptic solar magnetic fields.

I did all the analysis of the data. I made all the figures and wrote the manuscript.

Acknowledgements

This thesis work was carried out at the Swedish Institute of Space Physics (IRF) in Lund. It has been a pleasure, and a great experience, to have had the possibility to do research in solar physics and space weather. The work is, of course, a teamwork. First of all, a big thanks to my supervisor Henrik, for explaining all the fun stuff about the Sun. His enthusiasm, ideas and knowledge have certainly inspired me to continue in this field. I have also learnt that the best place in the world is California, driving a Mercedes while listening to Pavarotti and enjoying California wine, although perhaps not at the same time. Thanks Peter for always helping me with all sorts of things and for rewarding, and fun, discussions about everything from e.g. great Matlab scripts, how to fly, "smoke on the water" and the "death star cantine". Sarah, thank you for all your help. She always keeps a nice atmosphere, helps us with all our problems and makes everything work at IRF-Lund.

At the department of physics I would like to thank my co-supervisor Tomas Brage for all support and help. At IRF I would like to thank Lars Eliasson who accepted me into the Ph.D. programme and to Marta-Lena Antti for being helpful and very supportive in the National Graduate School of Space Technology. I am also grateful to Rick McGregor for reading the thesis. I would also like to thank all the Ph.D. students in the graduate school. I hope to see you all again.

At the Finnish Meteorological Institute (FMI) in Helsinki, Finland, I would especially like to thank Risto Pirjola for excellent collaborative scientific work, many discussions about ground effects and for your special "support" to science. Many thanks also to Ari Viljanen for his knowledge, expertise and help during our scientific studies. Thanks also to Antti Pulkkinen at NASA Goddard Space Flight Center, USA, (earlier at FMI).

I also wish to thank Sture Lindahl (Gothia Power AB, Lund), for useful discussions and advice about power grid modeling in GIC calculations, and Håkan Swahn for providing data.

I would like to thank my parents, Bengt and Anita, for always showing an interest in what I am doing and for all their help and support. A very special thanks to Åse, my own special star and "Princess", for all support and patience (and tasty pies).

Special thanks also to Skrylle, Friskis & Svettis and Krav Maga Malmö for helping me to keep fit. Finally I would like to thank all my friends and relatives for their interest and tricky questions about the Sun and space weather.

Magnus Wik
Lund, Sweden
October, 2008

References

Addison, P.: The Illustrated Wavelet Transform Handbook, Introductory Theory and Applications in Science, Engineering, Medicine and Finance, Institute of Physics Publishing, Bristol, 2002.

Amm, O.: Ionospheric elementary current systems in spherical coordinates and their application, J. Geomagn. Geoelectr., 49, 7, 947– 955, 1997.

Amm, O., and Viljanen, A.: Ionospheric disturbance magnetic field continuation from the ground to ionosphere using spherical elementary current systems, Earth Planets Space, 51, 431–440, 1999.

Ballester, J. L., Oliver, R., and Carbonell, M.: The near 160 day periodicity in the photospheric magnetic flux, Astrophys J, 566, 505–511, 2002.

Bartels, J., Heck, N. H., and Johnston, H. F.: The three-hour-range index measuring geomagnetic activity, J. Geophys. Res., 44, 411–454, 1939.

Bhatnagar, A., and Livingston, W.: Fundamentals of solar astronomy, World Scientific Publishing Co. Pte. Ltd., 2005.

Bolduc, L.: GIC observations and studies in the Hydro-Québec power system. J. Atmos. Sol. Terr. Phys., 64, 16, 1793–1802, 2002.

Boteler, D. H., and Pirjola, R. J.: Modelling Geomagnetically Induced Currents produced by Realistic and Uniform Electric Fields. IEEE Trans Power Delivery, 13, 4, 1303–1308, 1998.

Bothmer, V., and Daglis, I.A.: Space Weather: Physics and Effects, Springer, 476pp, 2007.

Campbell, W. H.: Introduction to geomagnetic fields, Cambridge University Press, 2003.

Charbonneau, P., Dynamo models of the solar cycle, Living Reviews in Solar Physics, Max Planck Institute for solar research, 2005.

Cowley, S. W. H.: Magnetosphere-ionosphere interactions: A tutorial review, Geophysical monograph 118, 91–106, American Geophysical Union, 2000.

Davidson, P.A.: An Introduction to Magnetohydrodynamics, Cambridge University Press, 452 pp, 2001.

Davis, T. N., and Sugiura, M.: Auroral electrojet activity index AE and its universal time variations, J. Geophys. Res., 71, 3, 785–801, 1966.

Elman, J.L.: Finding structure in time, Cognitive Science, 14, 179–211, 1990.

Fleck, B., Domingo, V., Poland, A. I.: The SOHO Mission, Kluwer Academic Publishers, 1995.

Frick, P., Galyagin, D., Hoyt, D. V., Nesme-Ribes, E., Schatten, K. H., Sokoloff, D., and Zakharov, V.: Wavelet analysis of solar activity recorded by sunspot groups, Astron. Astrophys., 328, 670–681, 1997.

Fröhlich, C. and Lean, J.: The Sun's total irradience: cycles, trends and related climate change uncertainties since 1976, Geophys. Res. Lett., 25, 4377–4380, 1998.

Gloeckler G., Cain J., Ipavich F.M., Tums E.O., Bedini P., Fisk L.A., Zurbuchen T.H., Bochsler P., Fischer J., Wimmer-Schweingruber R.F., Geiss J., and Kallenbach R.: Investigation of the composition of solar and interstellar matter using solar wind and pickup ion measurements with SWICS and SWIMS on the ACE spacecraft, Space Sci. Rev., 86, 1–4, 497–539, 1998.

Gonzalez, W. D., Joselyn, J. A., Kamide, Y., Kroehl, H. W., Rostoker, G., Tsurutani, B. T., and Vasyliunas, V. M.: What is a geomagnetic storm?, J. Geophys. Res., 99, 5771–5792, 1994.

Hagan, M.T., Demuth, H.B., and Beale, M.: Neural network design, Thomson Learning, 2002.

Haines, G.V.: Spherical cap harmonic analysis, J. Geophys. Res., 90, 2583–2591, 1985.

Haykin, S.: Neural Networks: A Comprehensive Foundation, Prentice Hall, 1998.

Hoeksema, J. T.: The solar magnetic field since 1976, John M. Wilcox Solar Observatory at Stanford, 1985.

Hoyt, D. V., and Schatten, K. H.: Group sunspot numbers: A new solar activity reconstruction, Sol. Phys., 181, 491–512, 1998.

Häkkinen, L., and Pirjola, R.: Calculation of electric and magnetic fields due to an electrojet current system above a layered earth, Geophysica, 22, 1–2, 31–44, 1986.

Ipavich, F. M., Galvin, A. B., Lasley, S. E., Paquette, J. A., Hefti, S., Reiche, K., Coplan, M. A., Gloeckler, G., Bochsler, P., Hovestadt, D., Grünwaldt, H., Hilchenbach, M., et al.: Solar wind measurements with SOHO: The CELIAS/MTOF proton monitor, J. Geophys. Res., 103, 17205–17213, 1998.

Ippolitov, I. I., Kabanov, M. V., and Loginov, S. V.: Wavelet analysis of hidden periodicities in some indexes of solar activity, Russ. Phys. J., 45, 11, 2002.

Kaufman, A.A., and Keller, G.V.: The Magnetotelluric Sounding Method: Elsevier, Amsterdam, 1981.

Kerridge, D.: INTERMAGNET: Worldwide Near-Real-Time Geomagnetic Observatory Data, British Geological Survey, 2001.

King, J.H.: Availability of IMP7 and IMP8 Data for the IMS Period, IMS Source Book: Guide to the International Magnetospheric Study Data Analysis, Editors: C. T. Russell, David J. Southwood, 304pp, American Geophysical Union, Washington, D.C. 1982.

Koen, J., and Gaunt, C.T.: Disturbances in the Southern African Power Network due to geomagnetically induced currents, Cigré Session, Paris, Paper 36–206, August 2002.

Lehtinen, M., and Pirjola, R.: Currents produced in earthed conductor networks by geomagnetically-induced electric fields, Ann. Geophys., 3, 4, 479–484, 1985.

Lepping, R. P., Acuña, M. H., Burlaga, L. F., Farrell, W. M., Slavin, J. A., Schatten, K. H., Mariani, F., Ness, N. F., Neubauer, F. M., Whang, Y. C., Byrnes, J. B., Kennon, R. S., Panetta, P. V., Scheifele, J., and Worley, E. M.: The Wind Magnetic Field Investigation, Space Sci. Rev., 71, 1–4, 207–229, 1995.

Lilensten, J., and Belehaki, A.: COST 724 final report: Developing the scientific basis for monitoring, modelling and predicting SpaceWeather, The COST 724 members, 2008.

Lindahl, S.: Effect of geomagnetically induced currents on protection systems, Elforsk rapport, Sweden, 2003.

Lundstedt, H., Liszka, L., and Lundin, R.: Solar activity explored with new wavelet methods, Ann. Geophys., 23, 1505–1511, 2005.

Lundstedt, H.: Solar activity modelled and forecasted: A new approach , Adv. Space Res., 38, 862–867, 2006a.

Lundstedt, H.: The sun, space weather and GIC effects in Sweden, Adv. Space Res., 37, 6, 1182–1191, 2006b.

Lundstedt, H., Wintoft, P., Wik, M., Eliasson, L., Pirjola, R., Viljanen, A., Pulkkinen, A., and Sjödin, Å.: Final Report: Real-Time Forecast Service for Geomagnetically Induced Currents, ESA/ESTEC Contract Number 16953/02/NL/LvH, 2007.

Mayaud, P. N.: Derivation, meaning, and use of geomagnetic indices, Geophysical Monograph Series, AGU, 1980.

McComas, D. J., Bame, S. J., Barker, P., Feldman, W. C., Phillips, J. L., Riley, P., and Griffee, J. W.: Solar wind electron proton alpha monitor (SWEPAM) for the Advanced Composition Explorer, Space Sci. Rev., 86, 563–612, 1998.

Mersmann, U., Baumjohann, W., Küppers, F., and Lange, K.: Analysis of an eastward electro jet by means of upward continuation of ground-based magnetometer data, J. Geophys., 45, 281–298, 1979.

Meyer-Vernet, N.: Basics of the solar wind, Cambridge University press, 2007.

Moussas, X., Polygiannakis, J. M., Preka-Papadema, P., and Exarhos, G.: Solar cycles: A tutorial, Adv. Space Res., 35, 725–738, 2005.

Ogilvie, K. W., Chornay, D. J., Fritzenreiter, R. J., Hunsaker, F., Keller, J., Lobell, J., Miller, G., Scudder, J. D., Sittler, Jr., E. C., Torbert, R. B., Bodet, D., Needell, G., Lazarus, A. J., et al.: SWE, a comprehensive plasma instrument for the WIND spacecraft, Space Sci. Rev., 71, 55–77, 1995.

Percival, D. B. and Walden, A. T.: Wavelet methods for time series analysis, Cambridge University Press, 2002.

Pirjola, R.: Geomagnetically Induced Currents During Magnetic Storms. IEEE Trans. Plasma Sci., 28, 6, 1867–1873, 2000.

Pirjola, R.: Effects of space weather on high-latitude ground systems, Adv. Space Res., 36, 12, doi: 10.1016/j.asr.2003.04.074, 2231–2240, 2005.

Pirjola, R., Boteler, D., and Trichtchenko, L.: Ground effects of space weather investigated by the surface impedance, Earth Planets Space, 2008.

Priest, E. R.: Solar Magnetohydrodynamics, D. Reidel Publishing Company, 1982.

Pulkkinen, A., Amm, O., Viljanen, A., and BEAR Working Group: Separation of the geomagnetic variation field on the ground into external and internal parts using the spherical elementary current system method, Earth Planets Space, 55, 3, 117–129, 2003.

Pulkkinen, A., Lindahl, S., Viljanen, A., and Pirjola, R.: Geomagnetic storm of 29-31 October 2003: Geomagnetically induced currents and their relation to problems in the Swedish high-voltage power transmission system, Space Weather, 3, S08C03, doi: 10.1029/2004SW000123, 19 pp., 2005.

Pulkkinen, A., Pirjola, R., and Viljanen A.: Determination of ground conductivity and system parameters for optimal modeling of geomagnetically induced current flow in technological systems, Earth Planets Space, 59, 999–1006, 2007.

Robinson, R. M., and Behnke, R. A.: The US National Space Weather Programme: A Retrospective, Space Weather, AGU Geophysical Monograph 125, 1, 2001.

Scherrer, P. H., Wilcox, J. M., Svalgaard, L., Duvall, T. L., Dittmer, P.H. and Gustafson, E. K.: The mean magnetic field of the sun: Observations at Stanford, Solar Physics, 54, 353–361, 1977.

Schrijver, C.J, and Zwaan, C.: Solar and Stellar Magnetic Activity, Cambridge University Press, 2000.

Schwabe, S.H.: Astronomische Nachrichten, 20, 495, 234–235, 1843.

Smith, C.W., L'Heureux, J., Ness, N.F., Acuña, M.H., Burlaga, L.F., Scheifele J.: The ACE Magnetic Fields Experiment, Space Sci. Rev., 86, 1–4, 613–632, 1998.

Sugiura, M.: Hourly values of equatorial Dst for IGY, pp. 945–948, in Annals of the International Geophysical Year, vol. 35, Pergamon Press, Oxford, 1964.

Syrjäsuo, M.T., Pulkkinen, T.I., Janhunen, P., Viljanen, A., Pellinen, R.J., Kauristie, K., Opgenoorth, H.J., Wallman, S., Eglitis, P., Karlsson, P., Amm, O., Nielsen, E., and Thomas, C.: Observations of substorm electrodynamics using the MIRACLE network, in: Proceedings of the International Conference on Substorms-4, Editors: S. Kokubun and Y. Kamide, Astrophysics and Space Science Library, vol. 238, Terra Scientific Publishing Company/Kluwer Academic Publishers, 111–114, 1998.

Vanlommel, P., Cugnon, P., Van Der Linden, R. A. M., Berghmans, D. and Clette, F.: The SIDC: World data center for the sunspot index, Solar Physics, 224, 1–2, 113–120, 2005.

Viljanen, A.: The relation between geomagnetic variations and their time derivatives and implications for estimation of induction risks, Geophys. Res. Lett., 24, 631–634, 1997.

Viljanen, A., Pulkkinen, A., Amm, O., Pirjola, R., Korja, T., and BEAR Working Group: Fast computation of the geoelectric field using the method of elementary current systems and planar Earth models, Ann. Geophys., 22, 101–113, 2004.

Waldmeier, M.: The sunspot-activity in the years 1610-1960, Schulthess & Co. AG, Zürich, 1961.

Wintoft, P.: Study of the Solar Wind Coupling to the Time Difference Horizontal Geomagnetic Field, Ann. Geophys., 23, 1949–1957, SRef-ID: 1432-0576/ag/2005-23-1949, 2005.

Zharkov, S.I., and Zharkova, V.V.: Statistical analysis of the sunspot area and magnetic flux variations in 1996–2005 extracted from the Solar Feature Catalogue, Adv. Space Res., 38, 5, 868–875, 2006.

Paper A

Calculation of geomagnetically induced currents in the 400 kV power grid in southern Sweden

SPACE WEATHER, VOL. 6, S07005, doi:10.1029/2007SW000343, 2008

Calculation of geomagnetically induced currents in the 400 kV power grid in southern Sweden

M. Wik,[1,2] A. Viljanen,[3] R. Pirjola,[3] A. Pulkkinen,[4,5] P. Wintoft,[1] and H. Lundstedt[1]

Received 13 June 2007; revised 12 April 2008; accepted 25 April 2008; published 31 July 2008.

[1] Sweden has experienced many geomagnetically induced current (GIC) events in the past, which is obviously due to the high-latitude location of the country. The largest GIC, almost 300 A, was measured in southern Sweden in the earthing lead of a 400 kV transformer neutral during the magnetic storm on 6 April 2000. On 30 October 2003, the city of Malmö at the southern coast suffered from a power blackout caused by GIC, leaving 50,000 customers without electricity for about 20–50 min. We have developed a model that enables calculation of GIC in the southern Swedish 400 kV power grid. This work constitutes the first modeling effort of GIC in Sweden. The model is divided into two parts. The electric field is first derived using a ground conductivity model and geomagnetic recordings from nearby stations. The conductivity model is determined from a least squares fit between measured and calculated GIC. GIC are calculated using a power grid model consisting of the topology of the system and of the transformer, transmission line, and station earthing resistances as well as of the coordinates of the stations. To validate the model, we have compared measured and calculated GIC from one site. In total, 24 events in 1998 to 2000 were used. In general the agreement is satisfactory as the correct GIC order of magnitude is obtained by the model, which is usually enough for engineering applications.

Citation: Wik, M., A. Viljanen, R. Pirjola, A. Pulkkinen, P. Wintoft, and H. Lundstedt (2008), Calculation of geomagnetically induced currents in the 400 kV power grid in southern Sweden, *Space Weather*, *6*, S07005, doi:10.1029/2007SW000343.

1. Introduction

[2] Geomagnetically induced currents (GIC) are the ground end of the space weather chain that originates at the Sun. During a geomagnetic storm, intense currents are produced in the magnetosphere and ionosphere creating time-dependent magnetic fields. At the Earth's surface, a geoelectric field is induced as expressed by Faraday's law of induction. The electric field drives currents in the ground and in man-made technological conductor networks, such as power grids, oil and gas pipelines, telecommunication cables, and railway equipment [e.g., *Pirjola*, 2000]. This paper focuses on power grids.

[3] GIC enter a power grid through earthed transformer neutrals ("earthing currents") and flow along transmission lines ("line currents") to other transformers, at which they go back to the ground. A GIC path between two transformers is shown in Figure 1. The characteristic times of GIC and geoelectromagnetic fields vary from seconds to days with 1 Hz regarded as the upper limit of the relevant frequencies involved. GIC flowing in power grids are thus DC-like compared to the 50/60 Hz frequency used for electricity. When GIC flow in transformer windings, a DC magnetic field is created that can saturate the core. This leads to a nonlinear operation of the transformer [e.g., *Kappenman and Albertson*, 1990; *Kappenman*, 1996; *Bolduc*, 2002; *Molinski*, 2002; *Lindahl*, 2003, and references therein]. The magnetizing current much increases during every half-cycle resulting in an excessive amount of harmonics. Protective relays may suffer from malfunction and parts of the system can be disconnected. Together with increased reactive power demands these effects may cause a collapse of the whole system. The most famous GIC event is the blackout in Québec, Canada, in March 1989 [e.g., *Bolduc*, 2002]. In a saturated transformer, the magnetic flux can spread out through structural members producing eddy currents, which in turn may cause hotspots possibly with permanent damage.

[4] In theory, GIC problems may be avoided by trying to block the flow of GIC by series capacitors or to decrease the magnitudes of GIC by additional resistances, also provided, e.g., by reactors in transformer neutral leads.

[1]Swedish Institute of Space Physics, Lund, Sweden.
[2]Department of Physics, Lund University, Lund, Sweden.
[3]Finnish Meteorological Institute, Helsinki, Finland.
[4]NASA Goddard Space Flight Center, Greenbelt, Maryland, USA.
[5]Goddard Earth Sciences and Technology Center, University of Maryland, College Park, Maryland, USA.

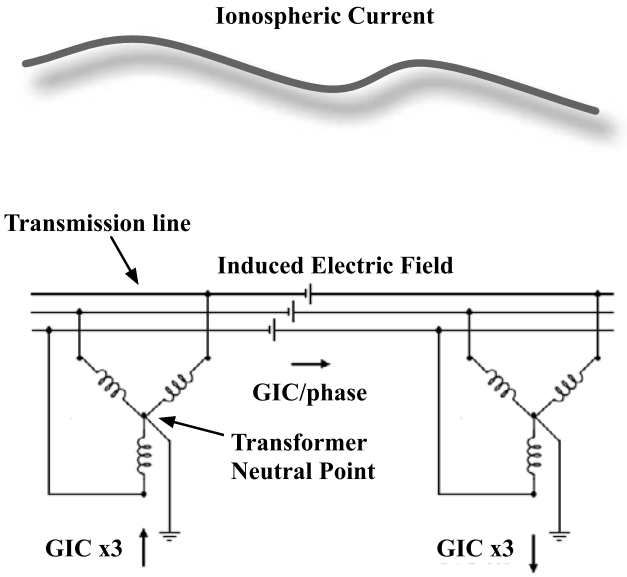

Figure 1. Geomagnetically induced currents (GIC) flowing along the transmission line between two transformers. A time-varying ionospheric current, i.e., the primary driver of GIC, is also schematically shown.

However, studies show that unless the locations are very carefully chosen, such devices may in fact increase GIC and the risks [*Erinmez et al.*, 2002a; *Pirjola*, 2002, 2005a]. Another approach to mitigate GIC effects is to use forecasting and nowcasting techniques of space weather events, so that the users of the systems may take suitable protective actions.

[5] GIC are mainly (but not only) a high-latitude phenomenon. Sweden has experienced many GIC problems in power systems [e.g., *Elovaara et al.*, 1992] as well as in telecommunication systems [e.g., *Karsberg et al.*, 1959] and even on railways [*Wallerius*, 1982]. A well-known GIC event is the power blackout in the city of Malmö at the southern coast of Sweden on 30 October 2003 [*Lindahl*, 2003; *Pulkkinen et al.*, 2005]. This outage affected 50,000 customers and lasted between 20 and 50 min. Furthermore, the largest measured GIC value that to our knowledge has ever been reported also refers to Sweden, where a current of almost 300 A, i.e., 100 A per phase, was measured in the earthing lead of a 400 kV transformer at the eastern coast of southern Sweden on 6 April 2000 [*Erinmez et al.*, 2002b].

[6] In spite of the many GIC problems that the Swedish high-voltage power grid has experienced, modeling of GIC in the system has not been performed until now. During the recent ''Space Weather Applications Pilot Project'' of the European Space Agency (ESA) a real-time forecast service for GIC was developed [*Wintoft*, 2005; *Lundstedt*, 2006]. In this paper we present results of model calculations of GIC in the southern Swedish 400 kV power grid, together with comparisons to measured GIC data at one site. Before a discussion of examples for several events (section 3), we summarize the GIC calculation technique (section 2) that includes geomagnetic data and network parameters as the input.

2. Calculation of GIC in a Power Grid

[7] Modeling of GIC in a power grid (or any other network) is conveniently divided into two independent steps: (1) calculation of the horizontal geoelectric field and (2) computation of GIC using this field. These two steps are usually referred to as the ''geophysical step'' and the ''engineering step.'' The former is more difficult since, in principle, it requires knowledge of magnetospheric-ionospheric currents and the Earth's conductivity distribution, both of which are complicated and not known accurately. On the basis of Maxwell's equations and boundary conditions, *Häkkinen and Pirjola* [1986] present exact formulas for calculating the electric and magnetic fields at the surface of a layered Earth due to a general three-dimensional magnetospheric-ionospheric current system. Numerical computations to perform the geophysical step are however laborious and slow. *Viljanen et al.* [2004] show that in practice the most appropriate method to determine the geoelectric field is to use ground-based geomagnetic data and the plane wave relation between the horizontal electric and magnetic fields at the Earth's surface:

$$E_x(\omega) = Z(\omega)B_y(\omega)/\mu_0,\ E_y(\omega) = -Z(\omega)B_x(\omega)/\mu_0 \qquad (1)$$

where $Z(\omega)$ is the (local) surface impedance and μ_0 is the vacuum permeability. The x and y axes point to the north and east, respectively. The impedance $Z(\omega)$ depends on the angular frequency ω and characterizes the Earth's conductivity structure. The use of equation (1) thus requires a Fourier transform between the time (t) and frequency (ω) domains. Usually, measured geomagnetic data are not available from a dense array of stations. Therefore the data have to be interpolated onto a grid covering the network (see Figure 2). This can be done by utilizing the Spherical Elementary Current System (SECS) method, which first includes the determination of equivalent ionospheric currents based on magnetic recordings [*Amm*, 1997; *Pulkkinen et al.*, 2003]. The magnetic field produced by these currents can then be computed at any point on the ground.

[8] The engineering step is more straightforward and can in principle be carried out exactly based on Ohm's and Kirchhoff's laws and on Thévenin's theorem. Owing to the low frequencies compared to 50/60 Hz, a dc treatment is sufficient. *Lehtinen and Pirjola* [1985] derive the formula

$$I_e = (U + Y_n Z_e)^{-1} J_e \qquad (2)$$

for the $N \times 1$ matrix I_e consisting of GIC flowing into the Earth at the N earthing points of the power grid considered. In equation (2), U is the $N \times N$ unit matrix and Y_n and Z_e are the $N \times N$ network admittance matrix

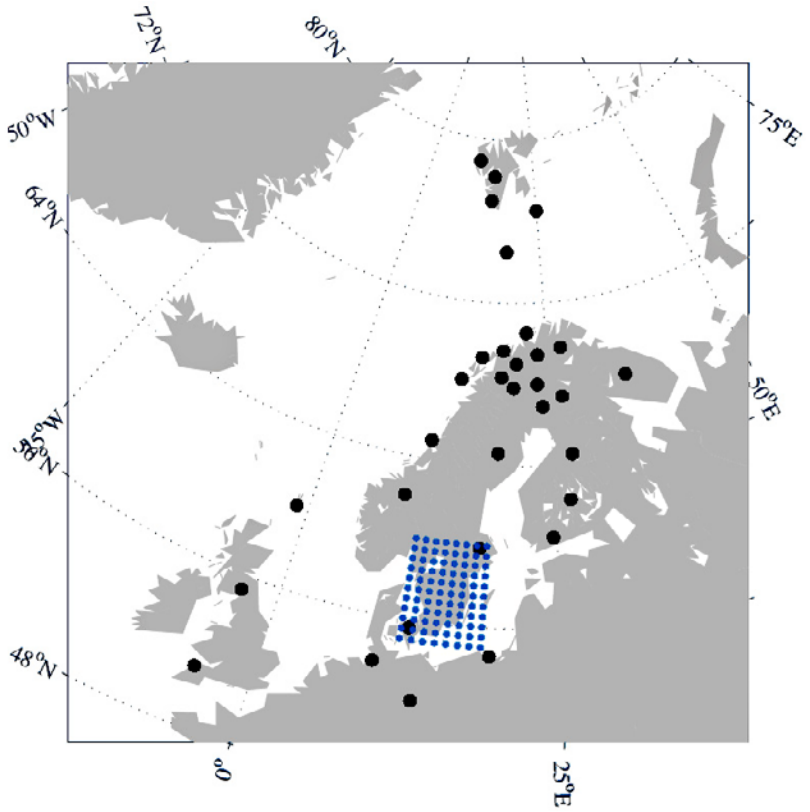

Figure 2. Magnetometer observatories (black) and a dense grid for the interpolation (blue). The observatories in the SW and NE corners of the grid are Brorfelde and Uppsala.

and the $N \times N$ earthing impedance matrix, respectively. The matrices Y_n and Z_e are real and depend on the resistances in the system. The $N \times 1$ matrix J_e involves the (geo)voltages obtained by integrating the geoelectric field along the paths defined by the transmission lines in the power grid. It is important to stress that the geoelectric field is generally rotational. This means that no single valued potential at the Earth's surface exists and the induced voltage between any two points depends on the integration path of the electric field [e.g., *Pirjola*, 2000]. The driver, or "battery," for GIC must then be treated as induced voltages in the transmission lines and not in the ground [*Boteler and Pirjola*, 1998]. A power system uses three-phase conductors. GIC flowing in a network will be divided equally between the phases. When calculating GIC, all three phases are therefore convenient to be handled as one conductor with a resistance of one third of that of a single phase.

3. Calculation of GIC in the 400 kV Power Grid

[9] We will consider the 400 kV system in southern Sweden with special attention to the site Simpevarp-2 (site 21 in Figure 3), at which GIC is recorded. To calculate GIC, we need the geoelectric field together with resistance, configuration and coordinate data of the whole power network (Figure 3).

[10] GIC have been recorded in the Swedish 400 kV power system since 1998. The recordings take place at a transformer neutral, Simpevarp-2 (site 21 in Figure 3), at the east coast close to the nuclear power plant OKG in Oskarshamn. In this study we refer to measured GIC data, recorded instantaneously every minute, from 1998 to 2000. At the end of 2000, a resistor was installed in the earthing lead of the transformer neutral of Simpevarp-2 to decrease GIC. Therefore it is not reasonable to include data later than 2000 in this study. The coordinates for OKG and the measurement site are approximately 57.4 N and 16.7 E.

[11] We start with an empirical approach and then present results by the full modeling. As a measure of success, we use the relative error, RE (%), between the measured (GIC_{meas}) and modeled GIC (GIC_{mod}) defined by

$$RE = 100 \cdot |GIC_{meas} - GIC_{mod}|/|GIC_{meas}| \quad (3)$$

where all timesteps with $|GIC_{meas}|$ exceeding a given threshold are included. We also use the linear correlation between measured and modelled GIC.

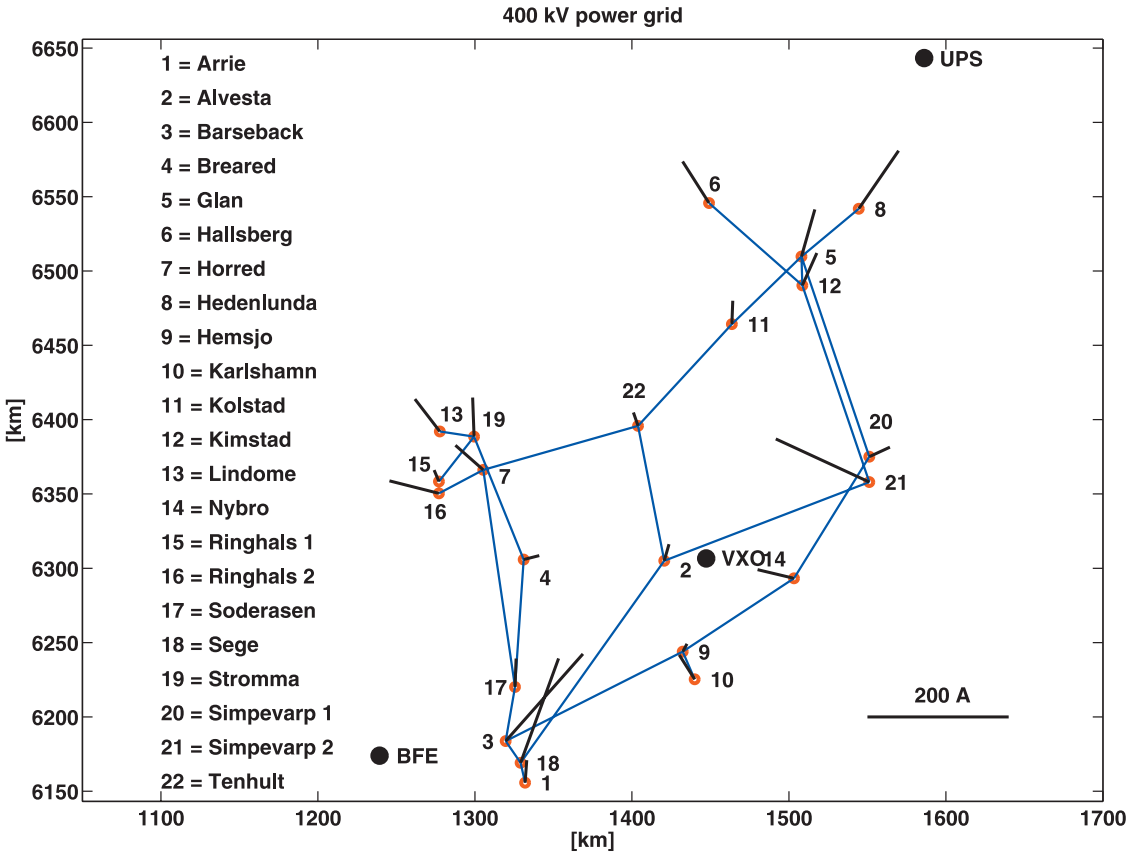

Figure 3. Southern Swedish 400 kV power grid model. The coordinates for Ringhals 1 and 2 and Simpevarp 1 and 2 are modified to better resolve them on the map. GIC is recorded at Simpevarp-2 (site 21). The black line segment gives the direction of a uniform electric field (1 V/km) which creates the largest GIC at each station. The amplitude of GIC is proportional to the length of the line segment. At Simpevarp-2, the maximum GIC is reached if the electric field points to, or from, west-northwest. The magnetic observatories, Brorfelde (BFE) and Uppsala (UPS), are also shown together with the new magnetometer station in Växjö (VXO) being installed into operation. The coordinates are given in the RT90 reference system.

3.1. Empirical Relation Between the Electric Field and GIC

[12] It is possible to try to relate the measured GIC directly to the modeled electric field without the DC description of the power grid. The simplest assumption is that the electric field is spatially uniform. Then GIC is simply:

$$GIC(t) = \alpha E_x(t) + \beta E_y(t) \tag{4}$$

where (E_x,E_y) are the modeled values close to the GIC site. The electric field is determined from a model of the Earth's conductivity. This is described in more detail in section 3.2.2. The coefficients (α,β) are determined by a least squares fit. Table 1 shows examples of the values. As seen, the ratio β/α depends on the selected threshold value of GIC as well as on the location of the point where the electric field is calculated. The ratio varies between -1.5 and -4.9, and its absolute value decreases with an increasing GIC threshold.

[13] The empirical approach is valid only for the specific GIC site with an additional assumption that the power grid remains unchanged. Consequently, the preferred modeling method is to use the DC description.

3.2. Full Network Modeling

[14] The full network GIC model is divided into a power grid model and an electric field model. We start with the power grid model and a comparison with the results in the previous section. We then determine the Earth's conductivity, in the electric field model, by comparing measured and modeled GIC.

3.2.1. 400 kV Power Grid

[15] The full approach requires a DC model of the power grid. The power grid data were obtained from

Table 1. Empirical Coefficients (α,β) From Equation (4)[a]

α	β	corr	MRE	GIC_0	long/lat	N
−31.0	137.5	69.6	56.3	5	16/57	3372
−28.9	137.3	69.6	56.3	5	17/57	3372
−31.7	134.2	69.6	56.3	5	16/57.5	3372
−28.8	134.1	69.6	56.3	5	17/57.5	3372
−59.3	151.5	72.7	53.5	10	16/57	1493
−54.9	152.1	72.7	53.5	10	17/57	1493
−57.7	147.6	72.7	53.5	10	16/57.5	1493
−52.5	148.3	72.7	53.5	10	17/57.5	1493
−94.2	163.2	74.9	52.5	15	16/57	843
−87.4	164.7	74.9	52.5	15	17/57	843
−90.4	158.8	74.9	52.5	15	16/57.5	843
−82.8	160.2	74.9	52.5	15	17/57.5	843
−113.0	171.9	76.1	54.0	20	16/57	554
−103.5	173.9	76.1	54.0	20	17/57	554
−107.6	167.6	76.1	54.0	20	16/57.5	554
−97.4	169.4	76.1	54.0	20	17/57.5	554

[a]Correlation between measured and modeled geomagnetically induced currents (GIC) is given by corr. The median relative error (%) between measured and modeled GIC is given by MRE. GIC_0 is the threshold value in amperes of measured GIC taken into account, long/lat is the electric field grid point in longitude and latitude, and N gives the number of available timesteps.

Svenska Kraftnät, SVK. They include the network topology, station coordinates, transformer resistances, transmission line resistances, and station earthing resistances. At some stations the 400 kV network is connected to the 130 kV system by autotransformers. The effect of autotransformers on GIC in the 400 kV system is approximately taken into account by decreasing the corresponding earthing resistance values. The grid considered contains 22 stations and 24 lines (Figure 3). We assume the lines to be straight between the stations. However, their correct resistance values, which take into account the real lengths of the lines, are used.

[16] To get a general idea about the distribution of GIC in the network, we first calculated GIC due to a uniform electric field of 1 V/km having any direction. In such a case, GIC is obtained from the electric field by

$$GIC(t) = a \cdot E_x(t) + b \cdot E_y(t) \quad (5)$$

where the multipliers (a,b) can be calculated based on the power grid data. Figure 3 shows the field directions that give the largest GIC, proportional to the black line segment, at each station. The scaling in the figure corresponds to the electric field magnitude 1 V/km. It is clear from the figure that the largest GIC are found at the corners and ends of the network [cf. *Viljanen and Pirjola*, 1994], and the sites most prone to experience large GIC can be identified.

[17] The coefficients of equation (5) for Simpevarp-2 are (a,b) = (−62.2,133.2) Akm/V. So the ratio b/a is about −2, which should be compared to the empirical ratio β/α. In an ideal case of a uniform electric field and a completely described power grid, these two ratios should be equal. We emphasize that (α,β) in equation (4) are not necessarily equal to (a,b) in equation (5). The former depend on both the power grid data and the selected conductivity model, whereas the latter depend only on the power grid data.

[18] There are some differences between the two approaches, whose explanations are as follows: The electric field is not spatially uniform in the whole power grid. Additionally, the closest magnetic observatories are quite distant, so the electric field calculated close to Simpevarp has some uncertainty. We will discuss the DC modeling problems in more detail in section. 3.4.

3.2.2. Geoelectric Field Model

[19] The next step in the full approach is to determine the model of the Earth's conductivity. This is performed by comparing the measured GIC to the modeled one.

[20] The geomagnetic field is recorded continuously at several sites in northern Europe. In this study we use stations in and near Sweden. They include all IMAGE magnetometer array sites and seven INTERMAGNET stations. By applying the SECS method, the geomagnetic data, with 1-min resolution, were interpolated to a dense grid, covering the area of the power grid (Figure 2). The surface electric field was then calculated, using equation (1), by multiplying the interpolated geomagnetic field by the surface impedance at each grid point.

[21] In the initial model, the Earth was uniform having the resistivity 40 Ωm. The resistivity was then optimized using a correction factor calculated from a least squares fit between measured and calculated GIC. With the correction factor equal to 1, the new value for the resistivity was 550 Ωm. This value was then used as a starting point for a second model consisting of two layers (one layer above a half-space). A table consisting of several hundred combinations of thicknesses and resistivities was then used to calculate, for each combination, the above correction factor again, together with the median relative error and the sum of the absolute errors. The final model, or combination, was based on a correction factor very close to 1, a low median error and a low sum of absolute errors. The final conductivity model has a thickness of 230 km, a resistivity of the upper layer 800 Ωm and a resistivity of the lower layer 250 Ωm (which we term 230/800/250). This is mainly in agreement with magnetotelluric measurements in southern Sweden (G. Schwarz, Swedish Geological Survey, private communication, 2007).

[22] It should be noted that in GIC calculations the geoelectric field is integrated along power transmission lines, so small horizontal details in the scale of 10 km or less of the ground conductivity can be neglected. A two-layer ground model has been used successfully for southern Finland as well [*Viljanen et al.*, 2006]. Here we assume that the same conductivity model can be used in the whole region of study. The simplest choice would be a uniform Earth only. However, the lower layer with a larger conductivity simulates better the general increase of the conductivity as a function with depth.

Table 2. Events Used in This Study[a]

	Event	Values	Maximum |*GIC*|	Correlation
01	19980924	35	38	0.40
02	19980925	472	77	0.67
03	19981002	82	25	0.34
04	19990815	63	19	0.91
05	19990820	53	24	0.80
06	19990830	21	21	0.83
07	19990922	207	73	0.86
08	19990926	52	19	0.81
09	19991010	53	27	0.67
10	19991012	73	25	0.23
11	19991022	310	67	0.64
12	19991028	42	29	0.68
13	20000122	49	30	0.66
14	20000224	90	19	0.68
15	20000406	321	269	0.55
16	20000523	71	31	0.90
17	20000608	290	63	0.70
18	20000710	22	23	0.91
19	20000711	77	44	0.79
20	20000713	129	21	0.71
21	20000714	147	49	0.92
22	20000715	469	222	0.81
23	20000719	12	39	0.43
24	20000812	232	34	0.76

[a]Listed in the table are the day of the event, number of values with |*GIC*| > 5 A, measured maximum |*GIC*|, and correlation between measured and calculated GIC. There are, in total, 3372 values used.

[23] Using equation (2), we then calculated GIC at Simpevarp-2 for 24 events in 1998 to 2000, i.e., at the previous sunspot maximum. The 24 events used here are listed in Table 2. The results, obtained by using the 230/800/250 model, for three of these events are shown in Figure 4. Also listed in the table are the correlation coefficients for measured (above 5 A) and modeled GIC for each event.

3.3. Error Analysis

[24] In this study we used data points with measured |*GIC*| > 5 A. The total number of values for all 24 events are then equal to 3372.

[25] The median relative error between measured and calculated GIC is 56.4 percent. For these events the correlation between measured and calculated GIC is about 0.7 (Figure 5).

[26] We then examined the relationship between the relative error and measured GIC. For practical applications it is significant to know if large relative errors tend to occur at large or small measured GIC values. Figure 6 shows that the relative error is smaller for large values of measured GIC, and vice versa, which is good for practical applications.

[27] For all events, in general, the modeled GIC follows qualitatively well the measured one, but there are times when the deviations in magnitude are quite large, e.g., for

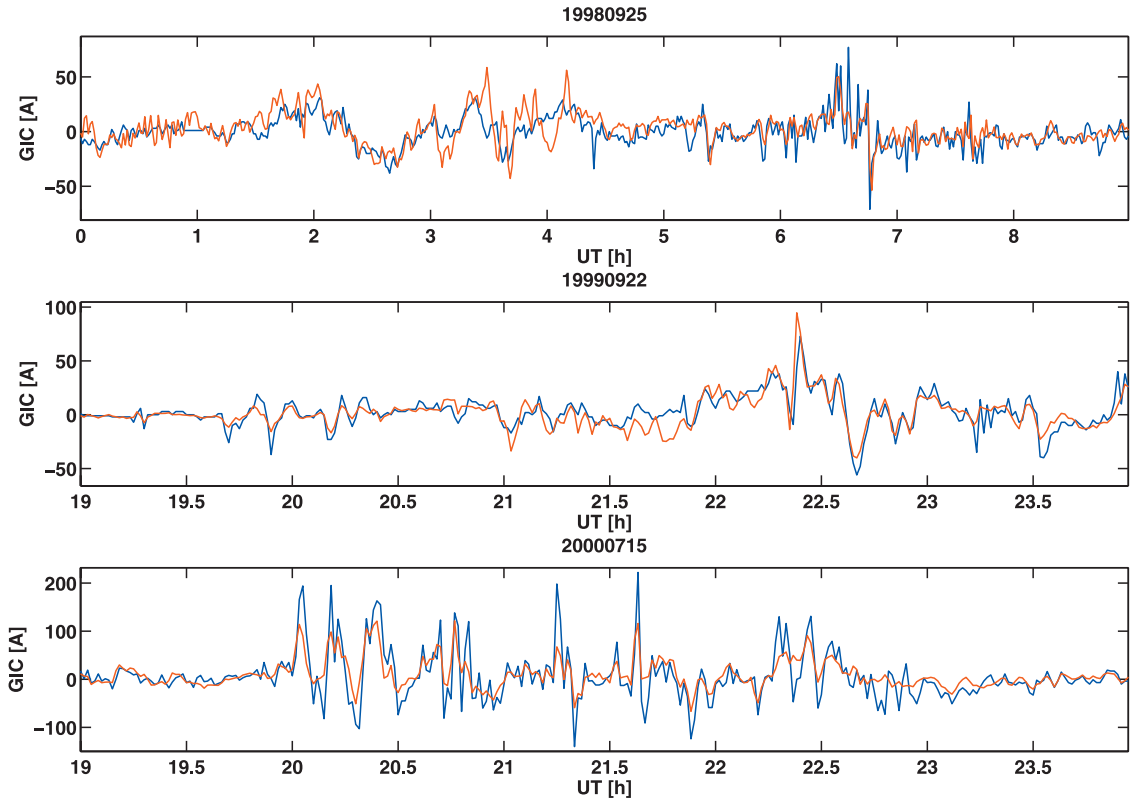

Figure 4. Measured (blue) and calculated (red) GIC at Simpevarp-2 for three events in 1998 to 2000.

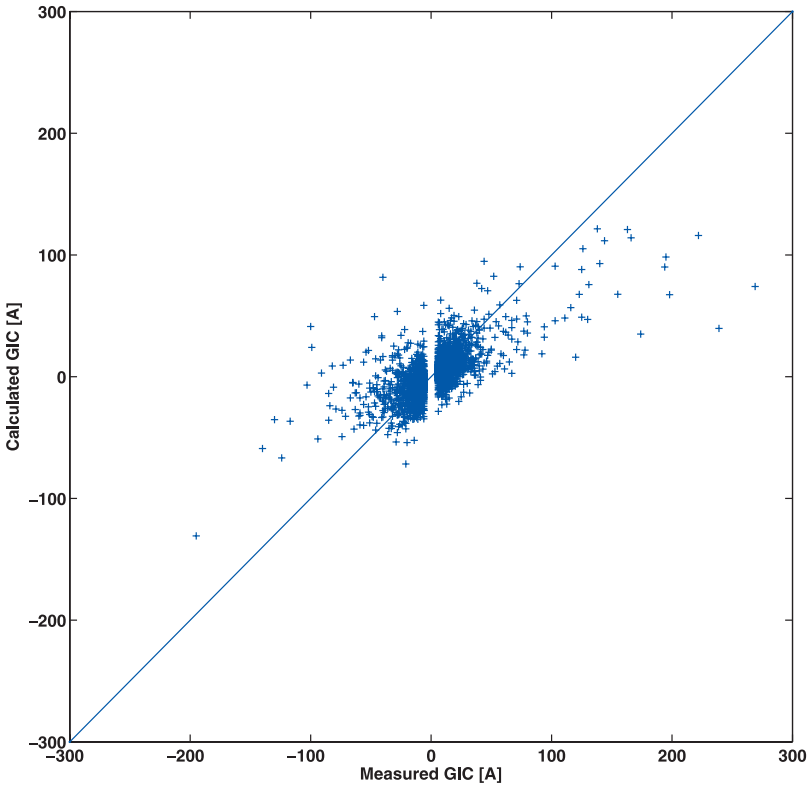

Figure 5. Calculated GIC (equation (5)) as a function of measured GIC at Simpevarp-2. The straight line indicates a perfect fit between measured and calculated GIC. The correlation is about 0.7. Data points with the absolute value of the measured GIC exceeding 5 A are considered. The total number of values is 3372.

the 6 April 2000 event. A possible reason for these differences is the large distance from Simpevarp-2 to the nearest magnetic observatory. In this study the closest magnetic observatories (Uppsala and Brorfelde) are situated about 280 km north of and 360 km southwest of the GIC measurement site, respectively. The variation of the magnetic field with latitude will therefore not be captured exactly [*Viljanen et al.*, 2004; *Pulkkinen et al.*, 2007].

[28] We examine the 6 April 2000 event (Figure 7) in some more detail. At the start of this event, the modeled GIC is in good agreement with the measured GIC, but later on the difference between them increases. One possibility is that the calculated geoelectric field does not capture the variation of the magnetic field at the end of the event.

[29] We therefore examined the magnetic field data from Uppsala and Brorfelde. The correlation for the magnetic field, B_x, between Uppsala and Brorfelde is about 0.9. This means that the magnetic field is rather homogenous during the event. The correlation for the derivative of the magnetic field, dB_x/dt, is, however, only 0.1. The magnetic field variation, dB_x/dt, is shown in the lower part of Figure 7. The negative of the derivative, $-dB_x/dt$, is related to the eastward geoelectric field [*Viljanen et al.*, 2001]. The geomagnetic variation is therefore a good indicator of the electric field and GIC at Simpevarp.

[30] Since Simpevarp is located about halfway between Uppsala and Brorfelde, it is reasonable to assume that the variation of the interpolated magnetic field, and therefore the electric field, close to Simpevarp-2, will have some degree of uncertainty. However, by comparing the measured GIC with dB_x/dt from Uppsala and Brorfelde, we see that the highest values of the derivative also occur when we have the highest values of GIC. It is likely that we would achieve a better agreement by using a 2-D/3-D conductivity model in combination with measurements of the magnetic field closer to Simpevarp. However, the use of such conductivity models would require much more CPU time, so they would be quite impractical in studies of long time series.

[31] For testing purposes of the effects of the time resolution we also calculated GIC based on 10 s geomagnetic data from Uppsala during the same event. Since we only used data from one magnetometer station, there is no interpolation of the magnetic field. Instead we choose the magnetic field from Uppsala to be the same all over the

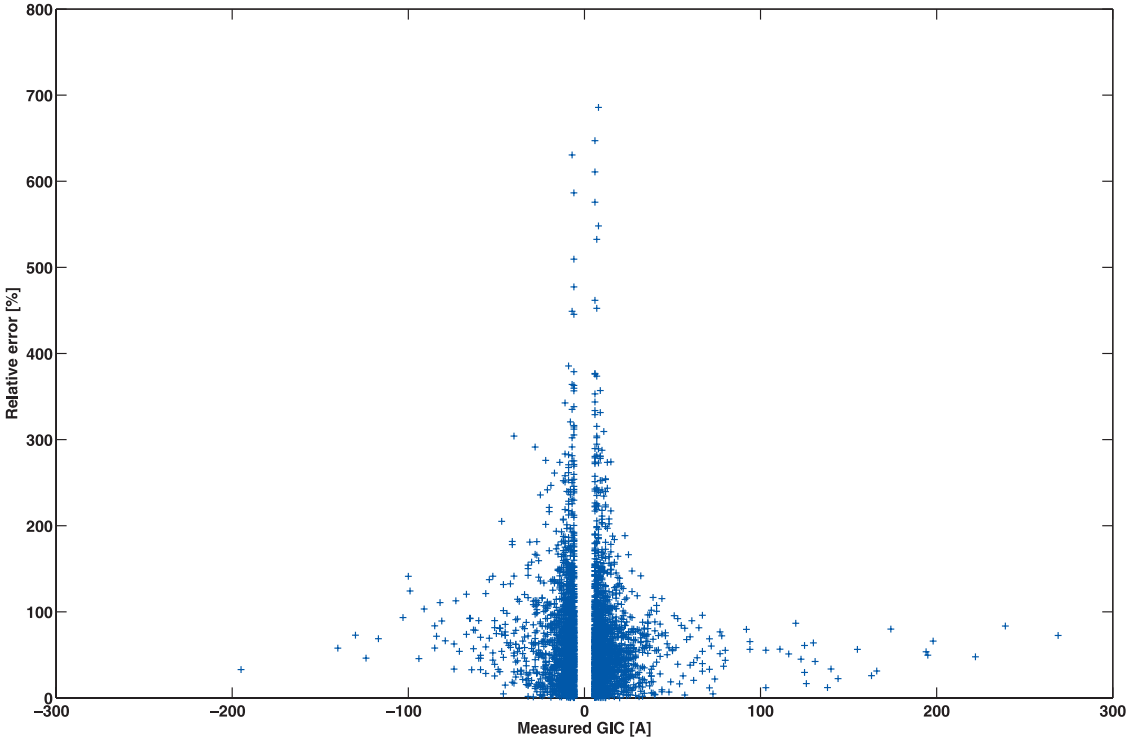

Figure 6. The relative error as a function of measured GIC at Simpevarp-2. Data points with the absolute value of the measured GIC exceeding 5 A are considered.

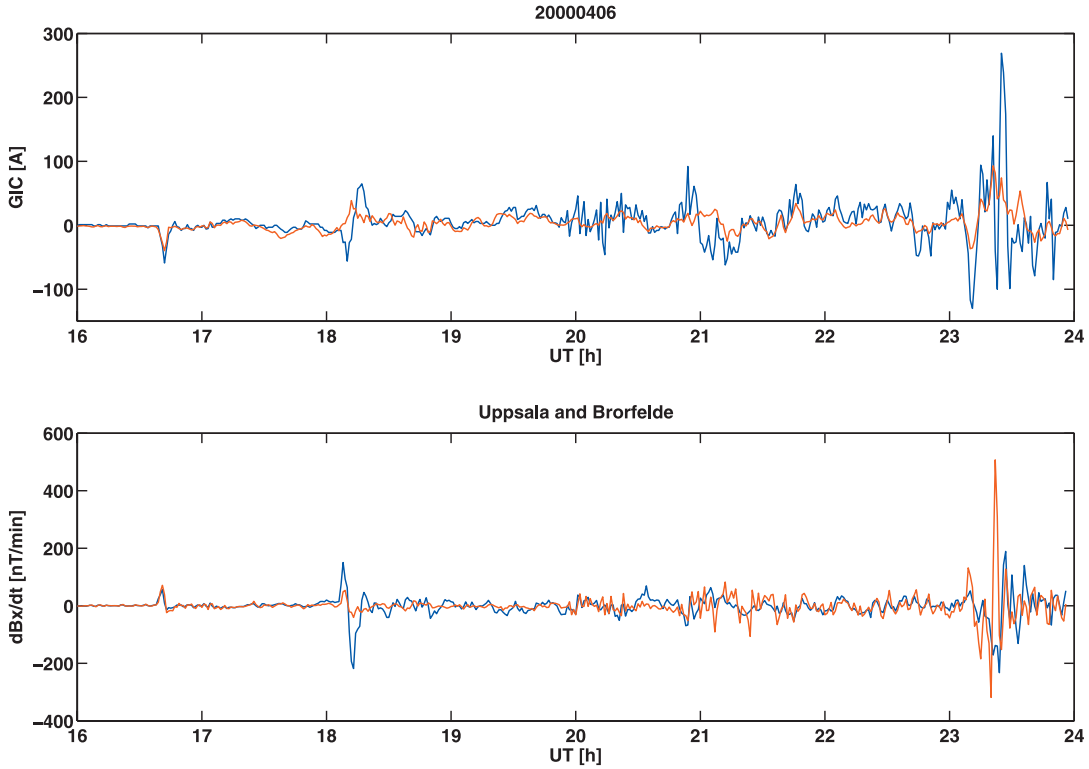

Figure 7. The top curve shows the measured (blue) and calculated (red) GIC at Simpevarp-2 (6 April 2000). The bottom curve shows dB_x/dt from Uppsala (blue) and Brorfelde (red).

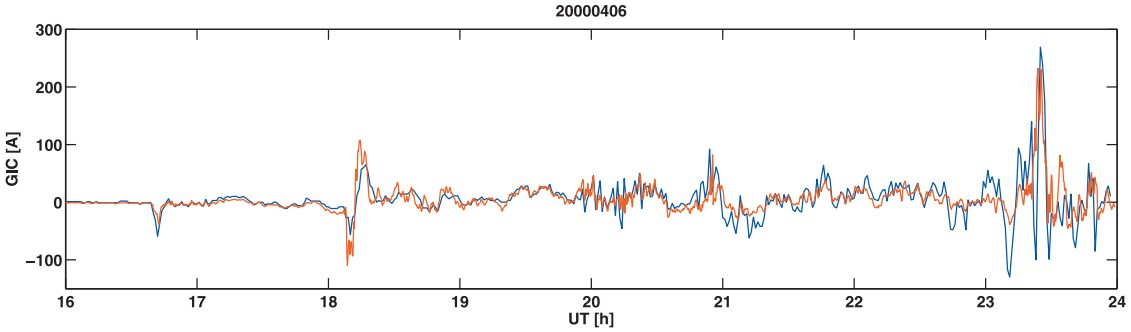

Figure 8. Measured (blue) and calculated (red) GIC at Simpevarp-2 (6 April 2000). Calculated GIC has a resolution of 10 s.

grid. The electric field was then calculated as before. The results are shown in Figure 8. In this case the calculated GIC correlates better with measured GIC. Using the same time stamps, we achieve a correlation of 0.59 between 1 min measured GIC and 10 s calculated GIC. Although not conclusive, this indicates that at times it might be necessary to use higher time resolution for the geomagnetic field. Unfortunately, 10 s data are not available for all magnetometer stations in the period 1998–2000. However, the use of 10 s data, for both GIC and geomagnetic data, should be considered for future studies.

[32] The results presented in this paper should also be compared with the nowcasting service of the Finnish natural gas pipeline system. In that study the distance between the GIC measurement site and the magnetic observatory is only about 30 km, giving a median error of about 30% [*Viljanen et al.*, 2006].

3.4. About Errors Caused by Deficiencies in the Power Grid Model

[33] In principle, the engineering step of a GIC calculation can be performed exactly based on Ohm's and Kirchhoff's laws and Thévenin's theorem and by combining geoelectric data with the power grid model, which includes the resistance values and the configuration of the system. In practice, however, power grid data are never perfect, and so GIC calculations necessarily involve approximations. The values of station earthing resistances provided by power companies usually refer to measured 50/60 Hz ac data while dc resistances are needed for GIC computations. Furthermore, earthing resistances of some stations often even remain completely unknown and thus have to be replaced by average estimates. Effects of networks with voltages less than 400 kV, not included in the present study, are approximated by changing the effective earthing resistances met by GIC at stations with autotransformers. These problems with earthing resistances are, however, not important in practice since the impacts of uncertainties in those data on GIC have been shown to be insignificant [e.g., *Kappenman et al.*, 1981, p. 4–10; *Pirjola*, 2008].

[34] Larger and more serious errors may occur in the calculation of GIC if possible additional resistances in earthing leads of transformer neutrals or some transmission lines are excluded from the power grid model. *Pirjola* [2005b] has shown that when focusing on GIC at a particular site it is sufficient to consider a smaller grid in the vicinity of the site. Therefore, regarding GIC at Simpevarp-2, only stations in the eastern part of the power grid and lines entering Simpevarp-2 are important to be modeled correctly. We are not able to extract completely certain and precise information about all details and about possible temporary changes in the southern Swedish 400 kV grid from the power company, so this may be a reason for some of the discrepancies between measured and computed GIC data. However, in general, our calculations of GIC can obviously be considered correct and reliable.

4. Discussion and Conclusions

[35] Geomagnetically induced currents constitute the ground end of the space weather chain. They have been known since the mid-1850s, i.e., for a much longer time than the actual history of modern space weather research. GIC are a potential source of problems to technological systems. Today electric power transmission systems, discussed in this paper, are the most important regarding GIC, which can saturate transformers with harmful consequences extending from an increased harmonic content in the electric power to a blackout of the entire network and permanent damage of transformers. Several GIC events and effects on the power system have occurred in Sweden in the past.

[36] On the basis of theoretical modeling and measured data, this paper provides an analysis of GIC in the southern Swedish 400 kV system, and is thus the first quantitative modeling of GIC in Sweden. The input used in the study consists of magnetic data from several sites in northern Europe, especially from Brorfelde, Denmark, and Uppsala, Sweden, located southwest and northeast of the network, of power grid data and of GIC recordings

in the Simpevarp-2 transformer neutral at the eastern edge of the network.

[37] Altogether 24 GIC events in 1998 to 2000 are investigated in this paper. After adjusting the initial conductivity model, a satisfactory agreement between modeled and measured GIC at Simpevarp-2 is obtained. For other sites, where GIC recordings are not available, we cannot estimate the accuracy of the model. However, for Simpevarp-2, the accuracy of the calculations is sufficient for practical purposes in which the levels of GIC rather than precise values should be known.

[38] A specific storm studied separately in this paper occurred on 6 April 2000, during which an extremely large GIC of almost 300 A was measured at Simpevarp-2. This is, as far as we know, the largest measured GIC ever reported. However, in this case the modeled GIC much differs from the measured data. A probable reason for this is that the calculated electric field is too smooth or that the time resolution is too low during the most extreme part of the event. This conclusion is in agreement with the results shown in Figure 8. It is also of interest to see that the modeled GIC appears to be systematically lower then the measured GIC, at least for larger GIC values (Figure 5). The large number of small GIC values makes a bias to the fit so that the results underestimate large GIC. This deviation becomes less prominent if we use a larger threshold for GIC. In general, we suspect that the largest GIC values are related to the most rapid magnetic field variations which are not captured by the 1 min data. For this reason, 10 s data of the magnetic field should be considered in future studies. Other reasons could be effects of the lower voltage systems, not included in the calculation, or some changes in the power grid configuration occurring every now and then.

[39] *Viljanen et al.* [2004] show that the spatial variation of the electric field due to the corresponding variation of ionospheric currents is rather uniform in southern Finland when considering length scales of the order of 100–200 km. Owing to the location even farther from the auroral region, a similar result is evident for southern Sweden. A practical consequence of this is that even a single magnetometer located close to Simpevarp-2 would provide good estimates of GIC there. However, the calculation results presented in this paper show that a reasonable modeling of GIC is possible even though the closest magnetometers are located in Brorfelde and Uppsala (see Figure 3). A new magnetometer is being installed in Växjö, Sweden. It is located about 120 km from Simpevarp-2 and 30 km east of station Alvesta (site 2 in Figure 3). With this magnetometer we expect to get a better accuracy of the magnetic field and electric field.

[40] In this study we use a simple two-layered Earth model. This is reasonable since GIC at a given site is not only related to the local electric field at the same site, but to the regional average. To obtain the voltages, driving GIC in the network, the electric field is integrated along the paths defined by the transmission lines. Since this is a spatially smoothing operation, small-scale Earth conductivity anomalies are not significant. Also, for GIC at any given site, it is not necessary to know the electric field in very distant regions, but the nearest part of the network is dominating [see *Pirjola*, 2005b].

[41] In the future, we plan to improve the GIC model. This includes a refinement of the conductivity model of the Earth and the incorporation of data from the new magnetometer in Växjö. So far we have basically ignored the lower voltage grids (130 and 220 kV) when considering GIC in the 400 kV network. At the next stage we plan to estimate the effects of the lower voltage systems on GIC magnitudes more precisely. A final aim is to include all relevant voltage levels accurately in the GIC computations. An extension to other parts of the Swedish high-voltage system is also straightforward. Combining the GIC calculation with solar observations and space weather forecasting will enable the development of a GIC warning service to the power industry [*Wintoft*, 2005].

[42] **Acknowledgments.** We wish to thank Sture Lindahl (Gothia Power AB, Lund, Sweden) for useful discussions and advice about power grid modeling in GIC calculations. We are grateful to ELFORSK, E.ON, and Svenska Kraftnät (SVK) for supporting our studies and for providing power grid data to us. This study is partly included in the ESA pilot project SDA, ''Real-time forecast service for geomagnetically induced currents,'' supported by ESA and ELFORSK. That study was a joint collaboration between the Swedish Institute of Space Physics (IRF) and the Finnish Meteorological Institute (FMI). We also thank all institutes providing magnetometer data to IMAGE and INTERMAGNET.

References

Amm, O. (1997), Ionospheric elementary current systems in spherical coordinates and their application, *J. Geomagn. Geoelectr.*, *49*(7), 947–955.

Bolduc, L. (2002), GIC observations and studies in the Hydro-Québec power system, *J. Atmos. Sol. Terr. Phys.*, *64*(16), 1793–1802.

Boteler, D. H., and R. Pirjola (1998), Modelling geomagnetically induced currents produced by realistic and uniform electric fields, *IEEE Trans. Power Delivery*, *13*(4), 1303–1308.

Elovaara, J., P. Lindblad, R. Pirjola, S. Larsson, and B. Kielén (1992), Geomagnetically induced currents in the Nordic power system and their effects on equipment, control, protection and operation, paper presented at CIGRE Session 1992, Int. Counc. on Large Electr. Syst., Paris.

Erinmez, I. A., J. G. Kappenman, and W. A. Radasky (2002a), Management of the geomagnetically induced current risks on the national grid company's electric power transmission system, *J. Atmos. Sol. Terr. Phys.*, *64*(5–6), 743–756.

Erinmez, I. A., S. Majithia, C. Rogers, T. Yasuhiro, S. Ogawa, H. Swahn, and J. G. Kappenman (2002b), Application of modelling techniques to assess geomagnetically induced current risks on the NGC transmission system, paper presented at CIGRE Session 2002, Int. Counc. on Large Electr. Syst., Paris.

Häkkinen, L., and R. Pirjola (1986), Calculation of electric and magnetic fields due to an electrojet current system above a layered earth, *Geophysica*, *22*(1–2), 31–44.

Kappenman, J. G. (1996), Geomagnetic storms and their impact on power systems, *IEEE Power Eng. Rev.*, *16*(5), 5–8.

Kappenman, J. G., and V. D. Albertson (1990), Bracing for the geomagnetic storms, *IEEE Spectrum*, *27*(3), 27–33.

Kappenman, J. G., V. D. Albertson, and N. Mohan (1981), Investigation of geomagnetically induced currents in the proposed Winnipeg-Duluth-Twin Cities 500-kV transmission line. Res. Proj. 1205-1, Final Rep. EL-1949, 171 pp., Electr. Power Res. Inst., Palo Alto, Cali.

Karsberg, A., G. Swedenborg, and K. Wyke (1959), The influences of earth magnetic currents on telecommunication lines (English edition), *Tele*, *1*, 1–21.

Lehtinen, M., and R. Pirjola (1985), Currents produced in earthed conductor networks by geomagnetically-induced electric fields, *Ann. Geophys.*, *3*, 479–484.

Lindahl, S. (2003), Effect of geomagnetically induced currents on protection systems, report, Elforsk, Stockholm, Sweden.

Lundstedt, H. (2006), The sun, space weather and GIC effects in Sweden, *Adv. Space Res.*, *37*(6), 1182–1191.

Molinski, T. S. (2002), Why utilities respect geomagnetically induced currents, *J. Atmos. Sol. Terr. Phys.*, *64*(16), 1765–1778.

Pirjola, R. (2000), Geomagnetically induced currents during magnetic storms, *IEEE Trans. Plasma Sci.*, *28*(6), 1867–1873.

Pirjola, R. (2002), Fundamentals about the flow of geomagnetically induced currents in a power system applicable to estimating space weather risks and designing remedies, *J. Atmos. Sol. Terr. Phys.*, *64*(18), 1967–1972.

Pirjola, R. (2005a), Averages of geomagnetically induced currents (GIC) in the Finnish 400 kV electric power transmission system and the effect of neutral point reactors on GIC, *J. Atmos. Sol. Terr. Phys.*, *67*(7), 701–708.

Pirjola, R. (2005b), Effects of space weather on high-latitude ground systems, *Adv. Space Res.*, *36*(12), 2231–2240, doi:10.1016/j.asr.2003.04.074.

Pirjola, R. (2008), Study of effects of changes of earthing resistances on geomagnetically induced currents in an electric power transmission system, *Radio Sci.*, *43*, RS1004, doi:10.1029/2007RS003704.

Pulkkinen, A., O. Amm, A. Viljanen, and BEAR Working Group (2003), Ionospheric equivalent current distributions determined with the method of spherical elementary current systems, *J. Geophys. Res.*, *108*(A2), 1053, doi:10.1029/2001JA005085.

Pulkkinen, A., S. Lindahl, A. Viljanen, and R. Pirjola (2005), Geomagnetic storm of 29–31 October 2003: Geomagnetically induced currents and their relation to problems in the Swedish high-voltage power transmission system, *Space Weather*, *3*, S08C03, doi:10.1029/2004SW000123.

Pulkkinen, A., R. Pirjola, and A. Viljanen (2007), Determination of ground conductivity and system parameters for optimal modeling of geomagnetically induced current flow in technological systems, *Earth Planets Space*, *59*(9), 999–1006.

Viljanen, A., and R. Pirjola (1994), Geomagnetically induced currents in the Finnish high-voltage power system: A geophysical review, *Surv. Geophys.*, *15*(4), 383–408.

Viljanen, A., H. Nevanlinna, K. Pajunpää, and A. Pulkkinen (2001), Time derivative of the horizontal geomagnetic field as an activity indicator, *Ann. Geophys.*, *19*, 1107–1118.

Viljanen, A., A. Pulkkinen, O. Amm, R. Pirjola, T. Korja, and BEAR Working Group (2004), Fast computation of the geoelectric field using the method of elementary current systems and planar Earth models, *Ann. Geophys.*, *22*, 101–113.

Viljanen, A., A. Pulkkinen, R. Pirjola, K. Pajunpää, P. Posio, and A. Koistinen (2006), Recordings of geomagnetically induced currents and a nowcasting service of the Finnish natural gas pipeline system, *Space Weather*, *4*, S10004, doi:10.1029/2006SW000234.

Wallerius, A. (1982), Solen gav Sverige en strömstöt (in Swedish), *Ny Tek.*, *29*, 3.

Wintoft, P. (2005), Study of the solar wind coupling to the time difference horizontal geomagnetic field, *Ann. Geophys.*, *23*, 1949–1957.

H. Lundstedt, M. Wik, and P. Wintoft, Swedish Institute of Space Physics, Scheelevägen 17, SE-22370, Lund, Sweden. (magnus@lund.irf.se)

R. Pirjola and A. Viljanen, Finnish Meteorological Institute, P. O. Box 503, FIN-00101 Helsinki, Finland.

A. Pulkkinen, NASA Goddard Space Flight Center, Greenbelt, MD 20771, USA.

Paper B

Space weather events in July 1982 and October 2003 and the effects of geomagnetically induced currents on Swedish technical systems

Manuscript prepared for Ann. Geophys.
with version 1.3 of the LaTeX class copernicus.cls.
Date: 21 October 2008

Space weather events in July 1982 and October 2003 and the effects of geomagnetically induced currents on Swedish technical systems

M. Wik[1,2], R. Pirjola[3], H. Lundstedt[1], A. Viljanen[3], P. Wintoft[1], and A. Pulkkinen[4,5]

[1]Swedish Institute of Space Physics, Scheelevägen 17, SE-22370, Lund, Sweden
[2]Department of Physics, Lund University, Box 118, SE-221 00 Lund, Sweden
[3]Finnish Meteorological Institute, P. O. Box 503, FI-00101 Helsinki, Finland
[4]NASA Goddard Space Flight Center, Greenbelt, Maryland, USA
[5]Goddard Earth Sciences and Technology Center, University of Maryland, Baltimore County, Maryland, USA

Abstract.

In this paper, we analyse in detail two famous space weather events; a railway problem on 13–14 July 1982 and a power blackout on 30 October 2003. Both occurred in Sweden during very intensive space weather storms and each of them a few years after the sunspot maximum. This paper provides a description of the conditions on the Sun and in the solar wind leading to the two GIC events on the ground.

By applying modelling techniques introduced and developed in our previous paper, we also calculate the horizontal geoelectric field at the Earth's surface in southern Sweden during the two storms as well as GIC flowing in the southern Swedish 400 kV power grid during the event in October 2003. The results from the calculation agree with all measured data available.

In the July-1982 storm, the geomagnetic field variation, ΔB, reached values up to $\sim$2500 nT/min and the geoelectric field reached values in the order of several volts per kilometer. In the October-2003 storm, the geomagnetic field fluctuations were smaller. However, GIC of some hundreds of amperes flowed in the power grid during the October-2003 event. Technological issues related to the railway signalling in July 1982 and to the power network equipment in October 2003 are also discussed.

1 Introduction

"Space Weather" can harmfully affect technological systems in space and at the Earth's surface. The origin of space weather is in the activity of the Sun. A comprehensive understanding of space weather storms and their impacts requires observations and knowledge of the whole chain of phenomena extending from the Sun to the Earth's surface. This is important both scientifically and practically when trying to avoid problems due to space weather.

"Geomagnetically induced currents (GIC)" flowing in networks, such as electric power transmission grids, oil and gas pipelines, telecommunication cables and railway systems, are ground effects of space weather. GIC impacts have already been known for about 150 years (e.g. Boteler et al. (1998); Lanzerotti et al. (1999); and references therein). The flow of GIC can easily be explained based on Faraday's and Ohm's laws: Time-varying currents in the near-Earth space create temporal variations of the geomagnetic field. They induce a (geo)electric field, which drives currents in conductors. Besides technological networks, the Earth is a conductor as well. Currents in the ground also contribute to geomagnetic variations and to induced geoelectric fields occurring at the Earth's surface (e.g. Watermann (2007)).

Electric power transmission systems constitute the most critical technological infrastructures regarding GIC today. Transformers can be saturated due to the flow of a dc-like GIC in the windings possibly leading to problems that may even extend to a collapse of the whole system or to permanent transformer damage (e.g. Kappenman and Albertson (1990); Kappenman (1996); Bolduc (2002); Molinski (2002); and references therein). Two famous GIC-produced blackouts have occurred, one in Québec, Canada, in March 1989 and the other in southern Sweden in October 2003 during the so-called Halloween storms. They have also been thoroughly analysed and reported (Bolduc (2002); Pulkkinen et al. (2005); Kappenman (2005)).

Swedish ground-based technological networks have suffered from GIC impacts several times (e.g. Elovaara et al. (1992); Boteler et al. (1998); Lundstedt (2006)). Observed problems are listed in Table 1 (with some minor uncertainties resulting from the lack of precise data). The fact that Sweden has experienced GIC impacts is understandable due to the high-latitude location of the country.

However, the proximity to the auroral zone is not the only

Correspondence to: Magnus Wik
(magnus@lund.irf.se)

Table 1. Problems due to GIC in ground-based technological systems in Sweden.

Date	Effects
2 Sept 1859	Problems with the telegraph system in Gothenburg
13–15 May 1921	Fires in telegraph equipment
11 Feb 1958	Fires with severe damage in telegraph equipment
13 Nov 1960	30 line circuit breakers tripped in the high-voltage power network
13–14 July 1982	4 transformers and 15 lines tripped in the high-voltage power system. Railway traffic lights turned erroneously to red. Telecommunications were also affected.
8–9 Feb 1986	5 events in the high-voltage power system, 1-3 lines tripped per event
13–14 March 1989	5 130 kV lines tripped, 5-degree temperature increase in a generator
24 March 1991	9 220 kV lines and a transformer tripped
9 Nov 1991	One 220 kV line tripped. Large pipe-to-soil voltages in a pipeline
1999	Radio communication for protection lost in the power system
2000	Voltage drop in the 400 kV system
6 April 2000	Largest ever GIC measured in a transformer (about 300 A)
30 Oct 2003	Power blackout in Malmö, excess heating in a transformer
8 Nov 2004	GIC of over 100 A measured in a transformer in southern Sweden

criterion for estimating the GIC risk. Both the magnitudes of GIC and the sensitivity of a system to experience problems depend much on the structure, resistances and other technical details of the network and its equipment.

Although GIC have possibly affected railway equipment several times in the past, only a few documented and published cases exist in the world. The Swedish railway problem in July 1982 is summarized by Wallerius (1982), and other examples refer to railways in Russia (Belov et al. (2007); Ptitsyna et al. (2007); Kasinskii et al. (2007); and Ptitsyna et al. (2008)).

The GIC impacts on the southern Swedish power system, resulting in the blackout in Malmö in October 2003, as well as the prevailing space and geophysical conditions then are described by Pulkkinen et al. (2005) and also discussed by Lundstedt (2006). A similar case study of other space weather events was analysed by Lam et al. (2002).

In Section 2, we describe the data used for both events in July 1982 and October 2003. This is followed by a description of the conditions on the Sun and in the solar wind leading to the railway signal malfunction in Section 3. Geoelectric field calculations are also compared to measured voltages in two communication cables. In Section 4, we give a similar description of the conditions on the Sun and in the solar wind leading to the power blackout in Malmö. Additional information is given by calculating the exact values of GIC that flowed in the 400 kV system during the event. Finally, in Sections 5 and 6 we discuss and compare both events.

2 Data

2.1 Solar data

Solar data and information were chosen from various sources including Solar-Geophysical Data Prompt Reports and Comprehensive Reports (published by NOAA National Geophysical Data Center, Boulder, USA). Solar images were captured by the solar telescope at the National Astronomical Observatory of Japan. Solar magnetograms were captured by the MDI instrument (Michelson Doppler Imager) onboard the SOHO (Solar Heliospheric Observatory) spacecraft. SOHO is in orbit around the Lagrangian point L1, between the Sun and the Earth, at a distance of about 1.5 million km from the Earth.

2.2 Solar wind data

Solar wind data were measured onboard the IMP8 (Interplanetary Monitoring Platform 8) spacecraft and the ACE (Advanced Composition Explorer) spacecraft. The IMP8 data were collected from the MAG instrument and the LANL experiment. It consists of the solar wind magnetic B_z component, the solar wind density and the speed. The ACE data consists of 4–minute averages of the solar wind magnetic B_z component and of the absolute magnetic field measurements collected from the MAG instrument, and 1–hour average helium ion bulk speed collected from the SWICS instrument. ACE is located in orbit around the L1 point and IMP8 is in an elliptical orbit around the Earth. The ACE/SWEPAM plasma measurements were unavailable during the Halloween events due to contamination.

2.3 Geomagnetic field data and indices

Geomagnetic field data, for both events, were collected from several sites in and near southern Sweden. They include data from IMAGE magnetometer array sites and from INTERMAGNET stations. Quiet-day values were subtracted from all data sets. As can be seen in Figure 1, there are several magnetometers in and around southern Sweden. For the July-1982 storm, we, however, used data only from three sites in the vicinity of southern Sweden, i.e. Wingst (Germany), Brorfelde (Denmark) and Lovö (Sweden), whereas for the October-2003 storm, magnetic recordings from altogether 35 stations were applied. This means that the accuracy of the calculations based on ground-based magnetic data is higher for the October-2003 event than for the July-1982 event.

The geomagnetic data, with a 1-minute resolution, were interpolated to a dense grid (88 points) covering southern Sweden (see Wik et al. (2008) for further details). From here on, all plots showing interpolated geomagnetic data (as well as geoelectric data) refer to two specific grid points. The first is situated near the city of Stockholm close to the site of a voltage recording in July, 1982 (see Section 3.2).

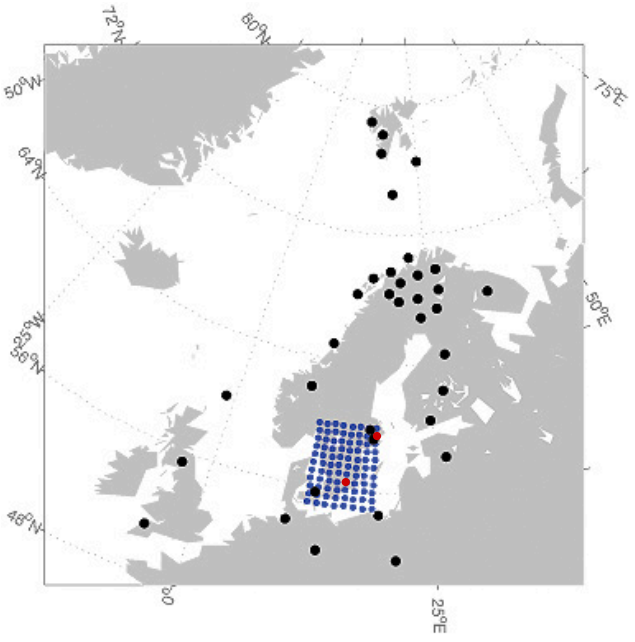

Fig. 1. Magnetometer stations (black) and a dense grid for the interpolation (blue). The observatory in the SW corner of the grid is Brorfelde, and the two observatories in the NE corner of the grid are Lovö and Uppsala. The two grid points, coloured in red, correspond to the locations for which the geoelectric and geomagnetic fields are plotted in figures 4, 5, 7 and 8. The more northern is for the July-1982 event, and the more southern is for the October-2003 event.

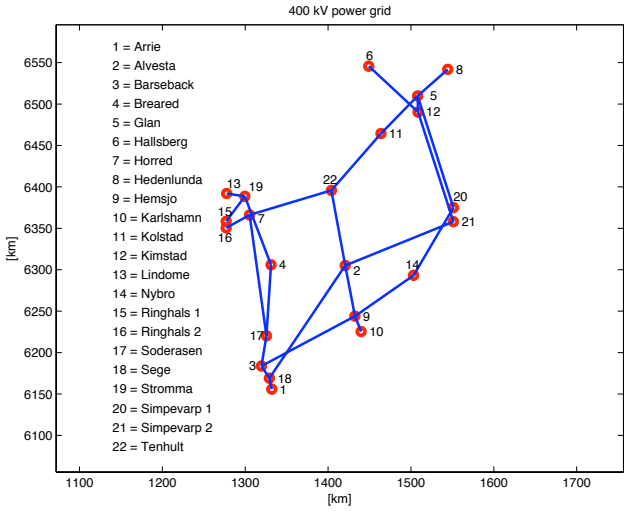

Fig. 2. Southern Swedish 400 kV electric power transmission grid. The transmission lines shown in blue colour are approximated to be straight.

The second is about halfway between the 400 kV power stations Simpevarp-1 and Sege (#20 and #18 in Figure 2). These two gridpoints, as well as all other gridpoints, are shown in Figure1.

Geomagnetic indices Dst and Kp are included as indicators of the global geomagnetic activity. The Kp index (Bartels et al. (1939)) is obtained from a number of magnetometer stations at mid-latitudes whereas the hourly Dst index (Sugiura (1964)) is obtained from magnetometer stations close to the equator. The AE index, which describes the auroral electrojet, is obtained from a number of stations distributed in the auroral zone in the northern hemisphere (Davis and Sugiura (1966)). The Dst and Kp indices were collected from the Space Physics Interactive Data Resource (SPIDR) within the NOAA National Geophysical Data Center in Boulder, USA. The AE index was collected from the World Data Center (WDC) for Geomagnetism in Kyoto, Japan.

2.4 Geoelectric field and voltage data

The geoelectric field was calculated at the same 88 grid points as the interpolated geomagnetic field. A two-layer Earth conductivity model, derived previously by Wik et al. (2008), was used all over the grid. It consists of a top layer with a thickness of 230 km and a resistivity of 800 Ωm above a half-space having a resistivity of 250 Ωm. The surface impedance is the transfer function between horizontal perpendicular magnetic and electric fields in the frequency domain, so that the Fourier-transform of B_x, multiplied by the surface impedance, and taking the inverse Fourier transform give the geoelectric field E_y in the time domain. Here we use the standard orthogonal coordinate system XYZ, where the x, y and z axes point northwards, eastwards and downwards, respectively.

Voltage data consist of recorded voltages from a southwest-directed telecommunication cable of about 28.7 km between Stockholm and Södertälje and from a northwest-directed telecommunication cable of about 28.0 km between Stockholm and Bro. The data consist of chart plots only since digital data are not available.

2.5 Geomagnetically Induced Currents

GIC are continuously measured, with a 1–minute resolution, at one of the Simpevarp 400 kV transformer neutrals. For the Halloween storms, measured data concern Simpevarp-1 (#20 in Figure 2) and are limited to October 29 and the morning of October 30 (see Figure 8). There are no other measurements due to problems with the monitoring system [private communication with Håkan Swahn]. Measured GIC data, during this event, consist of chart plots since digital data are not available.

To calculate GIC in the southern Swedish 400 kV power system, we used a model developed previously by Wik et al. (2008). It consists of the station coordinates and of the network configuration, topology and resistance values, and

it has been validated by comparing measured and calculated GIC at Simpevarp-2 (#21) for many events in 1998 to 2000. GICs were computed for all sites of the 400 kV network using geoelectric data at the grid points. The power grid map in figure 2 shows the present network configuration. During 1998 to 2000 the transmission line between Alvesta (#2) and Hemsjö (#9) did not exist.

As the power network model only concerns the 400 kV system, the possibility of a GIC flow between the 400 kV and 130 kV systems is only taken into account approximately by decreasing the 400 kV earthing resistance values at stations with autotransformers (Wik et al. (2008)). In practice, this means that the calculated GIC flowing between the 400 kV network and the Earth at a station with an autotransformer also includes GIC to (or from) the 130 kV system.

During October 2003, the power grid configuration was exceptional and slightly different from that shown in Figure 2 since Simpevarp-2 (#21) was not used at all and the lines from Alvesta (#2) and Kimstad (#12) were connected to Simpevarp-1 (#20).

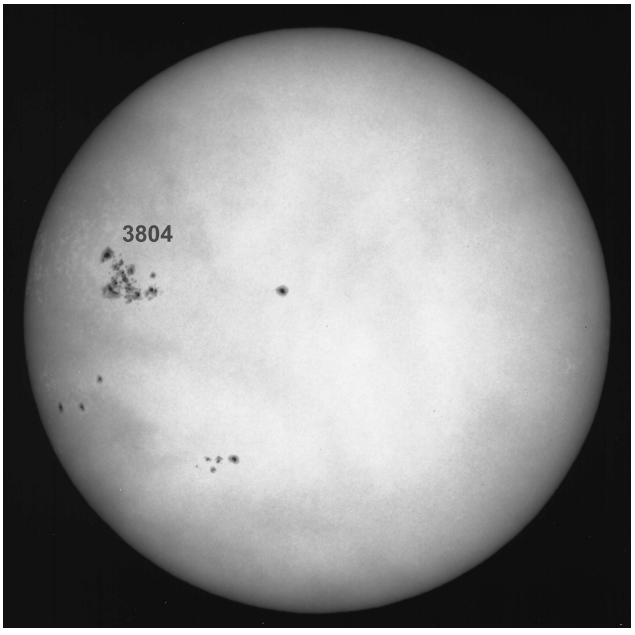

Fig. 3. White-light full disc image of the Sun at 09:18 UT on 12 July 1982, from the National Astronomical Observatory of Japan, Tokyo. The active region 3804, responsible for the geomagnetic storm on 13–14 July 1982, is clearly visible (Courtesy NAOJ).

3 The event of July-1982

3.1 Conditions on the Sun and in the solar wind

The July-1982 event started with a proton event registered at 07:00 UT on 11 July. It reached its maximum on 13 July at 16:15 UT with a proton flux of 2900 pfu. This is an indication of a CME approaching and, possibly, a geomagnetic storm (Gleisner and Watermann (2006)). The CME was perhaps related to a disappearing filament, from region 3804 located close to the solar equator but about 20–40 degrees east of the central meridian. The active region is shown in Figure 3 where east is to the left. A flare was also observed beginning at 05:03 UT on 12 July and ending at 06:30 UT the same day. The July-1982 event is also described by e.g. Mavromichalaki et al. (1991) and by Stüdemann et al. (1986).

The solar wind magnetic field is shown in Figure 4 together with e.g. the geomagnetic data and the calculated geoelectric field. The solar wind magnetic field component B_z was moderate until about 17–18 UT, on 13 July, when large negative values were detected. Later, at about 00:30 UT on 14 July, after a period of missing data, the instrument again detected large values, close to -40 nT, increasing to positive values. We believe that a CME, that arrived sometime after 16 UT on 13 July, was the cause. There is a large gap of missing data for the solar wind density and speed until about 04:00 UT on 14 July when high values were detected. This is also an indication of a CME.

3.2 Ground-Based Geomagnetic and Geoelectric Fields

The horizontal magnetic variations close to Stockholm, as indicated by the northern red grid point in Figure 1, are shown in Figure 4. Since the rate-of-change of the horizontal geomagnetic field, dB/dt, is related to the electric field it is also useful to examine the time derivatives of B_x and B_y. Here we simply use ΔB=$B(t+1)$-$B(t)$ as an approximation for dB/dt.

The geomagnetic storm on 13 July 1982, reached a peak intensity in ΔB_x of more than 2500 nT/min at midnight when the north component B_x was reduced by almost -5000 nT around midnight. The simultaneous peak intensity in ΔB_y was about -700 nT/min. This should be compared to the largest value at Nurmijärvi, in southern Finland, observed the same day, when ΔB_x reached 40 nT/s (Viljanen (1997)). During the blackout in Québec, Canada, in March 1989, the geomagnetic storm reached an intensity of $\sim$480 nT/min (Kappenman (2006)).

At around 16 UT on 13 July the shock front from the CME arrived causing a sudden storm commencement (SSC) and the compression of the magnetosphere on the dayside (see Mavromichalaki et al. (1991);Stüdemann et al. (1986)). After 18 UT the Dst index decreased to negative values indicating the injection of particles into the equatorial ring current. The main phase reached at minimum at Dst=-325 nT. The Kp index reached values of 8 to 9 until the early hours next day. The AE index reached values up to almost 2000 nT, indicating an increased activity of the electrojets corresponding to negative values in the solar wind B_z component (e.g. Davis and Sugiura (1966)). Since the electrojets were

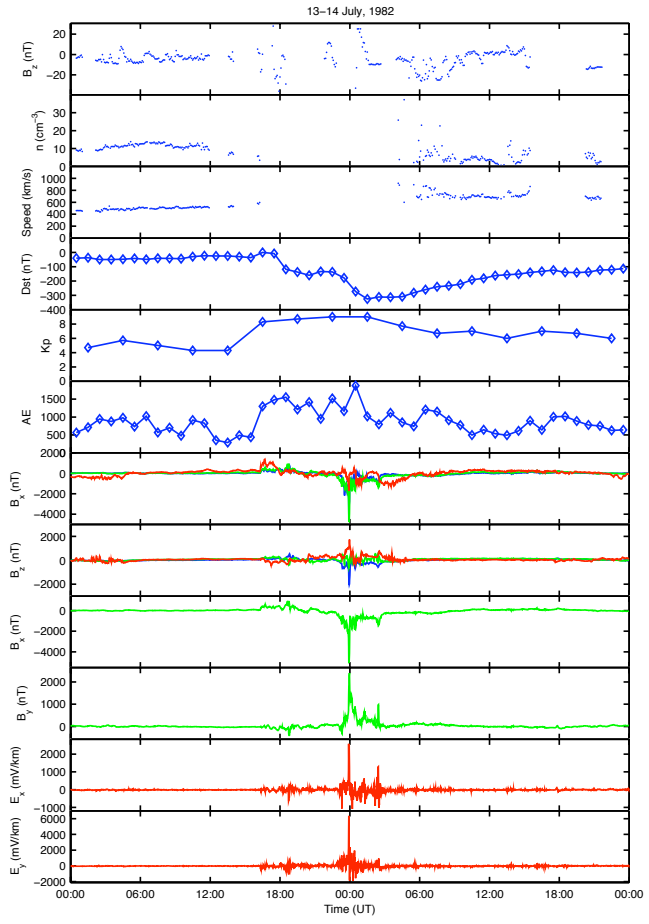

Fig. 4. Stack plot of IMP8 solar wind data, geomagnetic indices, geomagnetic data and geoelectric data for 13-14 July 1982. The IMP8 data, in the top panels, include solar wind magnetic field component B_z, the solar wind density, and the speed. The following panels show the geomagnetic indices Dst, Kp and AE. Measured geomagnetic components, B_x and B_z, are shown for Brorfelde (blue), Lovö (green) and Sodankylä (red). Interpolated geomagnetic north B_x and east B_y components are shown next. These data refer to the more northern red grid point in Figure 1 (see additional details in the text). Below the geomagnetic data are the calculated geoelectric north E_x and east E_y components at the same point.

occasionally located at very southern latitudes, the AE stations did not properly observe them. This is the reason why AE can be much smaller than the ground-based B_x value at subauroral sites.

In 1982 the magnetometer network was sparse. However, we can qualitatively estimate the location of the westward electrojet. The negative variation of B_x around the midnight of 13-14 July at Lovö was ∼5000 nT and Brorfelde ∼4000 nT, whereas at Sodankylä (lat 67.37 N) it was "only" ∼2000 nT. This suggests that the location of the centre of the electrojet was obviously near and a little south of the latitude of Lovö (see the middle panels in 4). Using data from only these three observatories does not enable a more precise determination of the position of the electrojet (see e.g. Maurer and Theile (1978);Bolduc et al. (1998);Bolduc et al. (2000)).

Two voltage recordings, together with electric field calculations (i.e. at the more northern red grid point in Figure 1), around midnight on 13-14 July 1982 are shown in figure 5. The first voltage recording is from an approximately southwest-directed telecommunication cable, from Stockholm to Södertälje, with a length of about 28.7 km. The second voltage recording is from an approximately northwest-directed cable, from Stockholm to Bro, with a length of about 28.0 km. These cables belonged to the Swedish railway system [private communication with Bertil Artelius]. The peak value, for both recordings, around 84 V thus means a horizontal geoelectric field of about 3 V/km, so that the total east-west geoelectric field reached a value of approximately 4–5 V/km. This event is also described by Kappenman (2006), who refers to a geoelectric field magnitude of 9.1 V/km. However, the value represents a very local electric field because it is based on a recording with the line length of only 0.921 km [private communication with Bertil Artelius]. Thus our data based on the Stockholm-Södertälje and Stockholm-Bro measurements are more representative in the evaluation of space weather impacts on large-scale networks.

3.3 Railway Effects

A description of the technological impact that resulted in a traffic light problem on the Swedish railways on 13-14 July 1982, is provided by Wallerius (1982). Supplemented by additional information [private communication with Bertil Artelius], the event is summarised in this section.

In the night between 13 and 14 July 1982, the traffic lights turned red without any obvious reason in a railway section of about 45 km in length in the southern part of Sweden (a little north of the centre of the grid shown in Figure 1). After a while the lights turned green and back to red again later. The reason was that the geoelectric field affected the relays as follows.

In normal conditions, in the absence of a train, a battery maintains a dc voltage of 3 to 5 V between the rails and over a relay, which is thus energised. A second circuit affected by the relay is connected to the traffic lights, which implies that the light is green when the relay is energised, whereas a de-energised relay produces a red light. When a train is present, the axles of the train short-circuit the rails making the voltage zero thus de-energising the relay leading to a red light.

During this event, the voltage between the rails associated with the induced geoelectric field had magnitudes in the order of volts. Consequently, it was large enough to affect the above-mentioned voltage of 3-5 V. At times when the induced voltage was opposite to the battery voltage, the latter was cancelled (at least partly) resulting in a de-energisation of the relay, which thus reacted as if the rails were occupied

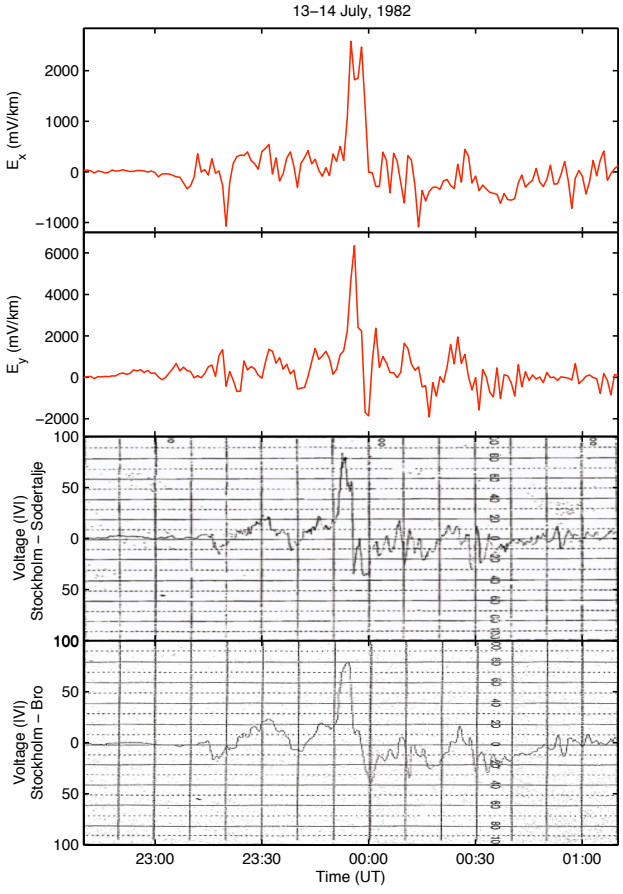

Fig. 5. Two voltage recordings (lower panels), together with electric field calculations (upper panels), from about 22:40 UT on 13 July to about 01:00 UT on 14 July 1982. The first recording is from an approximately southwest-directed telecommunication cable of about 28.7 km between Stockholm and Södertälje. The second recording is from an approximately northwest-directed telecommunication cable of about 28.0 km between Stockholm and Bro. The calculated electric field data refer to the more northern red grid point in Figure1.

and caused the traffic lights to turn red. When the induced voltage was reversed the lights became green again.

Geoelectric field values of about 4-5 V/km were observed in Sweden during the July-1982 storm (Section 3.2), which means that voltages of about 3-5 V are already obtained at length scales of one to two kilometers or even less, which can explain the railway traffic light malfunction. In the absence of an accurate technical description and diagram of the operation of the battery, the relay and the associated circuits, a detailed model calculation of the induced voltages in the equipment is neglected in this paper.

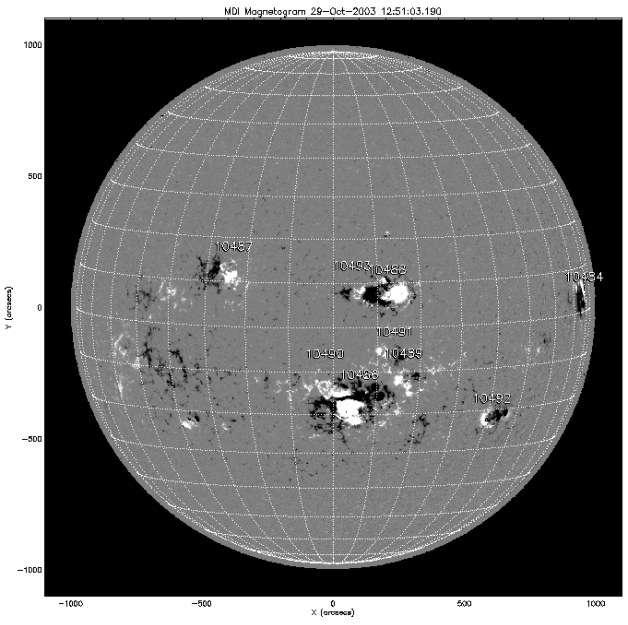

Fig. 6. Magnetogram showing the solar magnetic field on 28 October 2003, at about 12:51 UT. The huge active region 486, responsible for the space weather event resulting in the blackout in Malmö, is located in the middle just south of the solar equator (Courtesy MDI/SOHO team).

4 The event of October 2003

4.1 Conditions on the Sun and in the solar wind

Around 18 October 2003, the Sun showed signs of unusually high activity with the emergence of the active region 484. On 22 October, the large and complex active region 486 appeared on the east limb. During the period 26 October to 5 November a total of five full halo-CMEs arrived at the Earth with two of them producing geomagnetic storms with Kp=9. The active region 486 was responsible for both of them (see e.g. Weaver et al. (2004) and references therein). The active region 486 is shown in Figure 6. From here on we focus mainly on the time period from 28 to 30 October.

The Sun-Earth events of October 2003, whose solar and solar wind characteristics are depicted by the stackplot in Figure 7, began on 28 October at 11:10 UT with an X17 flare from the region 486. This was followed by a proton event at around 12 UT reaching the maximum of 29500 pfu at around 06:15 UT on the following day, when a CME driven shock arrived at L1. The halo-CME, from the region 486 located almost at the centre of the solar disc, had a speed close to 2000 km/s. At the same time the magnetic field magnitude $|\mathbf{B}|$ increased to about 60 nT and the B_z component reached about -50 nT. The propagation time for this CME was around 19 hours. The B_z component then turned northwards until $\sim$18:00 UT when it rotated southwards to negative values of

about -25 nT. It then stayed negative until about 02:40 UT on 30 October.

On 29 October at 20:49 UT an X10 flare event was observed, perhaps associated with the second halo-CME, with a speed ∼2000 km/s. The travel time for this CME was about the same and it reached the Earth on 30 October around 16:20 UT. A shock was then observed, as indicated by the rapid increase in $|\mathbf{B}|$. At around 18:20 UT the B_z component turned southwards, reaching -35 nT, until it turned northwards again after midnight (Skoug et al. (2004); Zurbuchen et al. (2004)).

On 4 November, when the active region 486 had reached the western limb of the Sun, it produced an X28 flare (the largest ever recorded) and a CME moving outward with a speed above 2300 km/s. However, this time the CME headed in a direction almost perpendicular to the Sun-Earth direction leading to only a minor geomagnetic storm.

4.2 Ground-Based Geomagnetic and Geoelectric Fields

The interpolated horizontal geomagnetic and calculated horizontal geoelectric fields are shown in figures 7 and 8 during the storm events on 29-30 October 2003. The fields presented concern the more southern red grid point shown in Figure 1 located approximately halfway between Sege and Simpevarp (#18, #20 and #21 in Figure 2).

At 6:15 UT on 29 October, a geomagnetic disturbance first occurred due to the solar wind shock, as seen in figures 7 and 8. The geomagnetic field was highly disturbed until 07 UT when the solar wind magnetic field component B_z turned positive. At around 19 UT the geomagnetic disturbance again increased. This lasted until ∼3 UT on 30 October.

With the arrival of a second CME on 30 October, another geomagnetic storm began in the evening. The highest intensity of ΔB_x was around 400 nT/min at 20:04 UT and the geomagnetic field deviated up to ∼2000 nT from the quiet day values. The electric field reached the value of 2 V/km at ∼20:04 UT. At this point scientists of IRF in Lund were already in contact with the operators of the E.ON power company to give them the latest update about the geomagnetic storm. Despite this, a blackout occurred at 20:07 UT in the city of Malmö. High intensity levels of ΔB_x around 350 nT/min also occured at 20:25 UT and 21:18 UT. The highest intensity of ΔB_y, with values of -470 nT/min and 573 nT/min, occurred on 29 October at around 06:45 UT and 15:00 UT. High values of about 400 nT/min also occurred on 30 October at ∼21:30 UT.

The first CME resulted in an extreme geomagnetic storm, with Kp=9. The geomagnetic storm intensity stayed at levels above Kp=7, even when the solar wind B_z-component was positive, until the morning of 30 October. The second CME also resulted in an extreme storm, with Kp=9, on 30 October (see Figure7). The AE index reached high values when the solar wind B_z component reached high negative values. This corresponds to the southward movement and enhancement of the auroral oval. This is also seen in the plots of the electrojet latitude and current density. The Dst index indicate that the equatorial ring current evolved during the event starting with the initial phase at around 06:15 UT and reached a minimum at midnight. The recovery phase continued until about 18 UT on 30 October when the second geomagnetic storm began.

To determine the location of the electrojet we used the method of spherical elementary current systems (SECS; Amm and Viljanen (1999)). We calculated the equivalent current density at the ionospheric altitude of 100 km along the meridian 22.06 deg E at the latitude range 59.02-79.42 deg N with a 0.6 degree step. The centre of the eastward electrojet is at the latitude of the maximum eastward current density, and the westward electrojet is centred at the minimum, respectively. The result is shown in the middle panels in Figure 7.

4.3 Calculation of GIC causing the Malmö Blackout

The power blackout that occurred in the city of Malmö in southern Sweden on 30 October 2003, began at 20:07 UT and lasted for 20 to 50 minutes affecting about 50000 customers (analysed in detail by Pulkkinen et al. (2005)). The blackout was caused by the tripping of a 130 kV line. It resulted from the operation of a relay that had a higher sensitivity to the third harmonic (=150 Hz) than to the fundamental frequency (=50 Hz). The excessive amount of the third harmonics in the system has been concluded to have resulted from transformer saturation caused by GIC.

Regarding the blackout in Malmö, GIC values at the nearby station Sege (#18) are of particular interest. However, as harmonics can propagate all over the network, large GIC in other transformers have probably also contributed to the adverse effects resulting in the blackout. Therefore we also consider GIC at Arrie (#1) and Barsebäck (#3) located next to Sege, and at Simpevarp-1 (#20). Calculated GIC for these four 400 kV stations on 29 and 30 October 2003, are depicted in Figure 7. A shorter interval of the calculated Simpevarp-1 GIC curve is also shown in Figure 8, which indicates a good agreement between measured and calculated GIC. Unfortunately, there are no measured GIC data available for Simpevarp-1 at times later than 06:00 UT on 30 October.

The GIC magnitudes remain clearly smaller at Sege than at the three other sites, the reason for which is an additional resistor of a few ohms in the earthing lead of the 400 kV transformer neutral at Sege that efficiently reduces GIC. The calculated GIC at Simpevarp-1 reaches a peak value of about 330 A a few minutes before the time of the Malmö blackout (at 20:07 UT on 30 October). The simultaneous GIC values at Arrie and Barsebäck are about 90 A and around 300 A. Calculated GIC data at Sege exhibit small values, around 15 to 20 A, at the time of the blackout although the highest GIC already occurred there in the morning of 29 October.

5 Discussion

In the July-1982 storm, the largest time derivative values of the ground magnetic field was much stronger than in the October-2003 storm. A similar conclusion was also made by Kappenman (2005). The peak value of about 2500 nT/min obtained for the July-1982 event is in agreement with the value of 40 nT/s in southern Finland reported by Viljanen (1997). We also see that, though being very large, the geoelectric field values remained smaller in the Halloween storm than in the July-1982 event.

Unfortunately there are large gaps in the solar wind data for the midnight hours on 13 July 1982. However, a large increase in the solar wind density and speed did occur in the afternoon of 13 July (Stüdemann et al. (1986)). On July 22 there was a second proton event, from the same region, but now 86 degrees west of the central meridian. This time the CME did not cause a significant disturbance, possibly because only the flank of the CME arrived at the Earth.

During 29–30 October 2003 there were two CMEs, resulting in intense geomagnetic disturbances. It is possible that these two CMEs, in combination, were the cause of higher geomagnetic disturbances on October 30. An X28 flare was observed at 19:50 UT on 4 November together with the fastest CME (∼2700 km/s) during October-November 2003 (Gopalswamy et al. (2005)). This time, however, the CME was not geoeffective since it erupted near the west limb of the Sun.

For the July-1982 event, we considered the geoelectric field affecting the railway circuit. We calculated the geoelectric field based on geomagnetic data and a two-layer Earth model and compared with voltage recordings from two telecommunication cables in Sweden. However, we have to take into account that the derivation of the geoelectric field from the chart plots of the voltage recordings is not completely reliable because we do not have exact documents of the recording arrangements in July 1982 including the distance between the measurement electrodes in the ground. This question is related to the fact that, due to the nonconservative, i.e. rotational, nature of the geoelectric field the cable applied to the recording should be straight (see Gomez-Trevino (1987)). A more quantitative calculation including an exact description of the railway circuit belongs to the aims of our future studies.

The calculated geoelectric field values of several volts per kilometer are much larger than the magnitudes calculated by using geomagnetic recordings from the Nurmijärvi Observatory in southern Finland (Pirjola (1985)). An obvious reason is that the uniform-Earth assumption made in those calculations is too rough, which emphasises the importance of an appropriate choice of the ground conductivity model in computations of the geoelectric field and GIC.

The calculated geoelectric field gets higher values than those based on the voltage recordings. A possible reason for this discrepancy is in the use of the two-layer ground conductivity model described in Section 2.4 for the area where the voltage measurements were carried out since the model was derived by comparing calculated and measured GIC data at Simpevarp-2 (#21 in Figure 1) located further south (Wik et al. (2008)).

The July-1982 storm also caused GIC problems in the Swedish high-voltage power system by tripping four high-voltage transformers and fifteen lines (Table 1). Fortunately, however, this happened in a favourable load situation, obviously thanks to the summer night time, and consequently more serious consequences were avoided. The same storm affected the telecommunication system in Sweden as well (Table 1). A lightning protection device was burnt at a station, and at other stations alarms were activated (Wallerius (1982)).

During the October-2003 event, particularly large GIC values could be expected at Simpevarp-1, as it was a corner and end station of altogether four lines. Normally Simpevarp-1 is connected to two stations only (see Figure 2).

The Malmö blackout was definitely caused by the misoperation of a relay too sensitive to the third harmonics of the fundamental frequency of 50 Hz. Since the southern Swedish 130 kV network is connected to the 400 kV system, GIC can easily flow between the two networks. In general, a higher voltage level with smaller resistances of the transmission lines means larger GIC values. Thus, GIC in the southern Swedish 400 kV system played a major role for the blackout in Malmö.

Consequently, there is a good reason to compute GIC in the 400 kV system for the October-2003 event. It is worth emphasising that the geoelectric data shown in figures 7 and 8 refer to a particular grid point indicated in Figure 1 and chosen to be representative for both Malmö/Sege and the GIC recording site at Simpevarp when situated about halfway between them. However, in the calculation of GIC, the spatial variation of the geoelectric field across southern Sweden was taken into account exactly. The calculated GIC values, which extend to a couple of hundreds of amperes, also indicate the intensity of the Halloween storm and provide further evidence that GIC were really the cause of the blackout. In order to evaluate reasons for the blackout, Pulkkinen et al. (2005) also present simulated GIC data for the Halloween storm, and the values obtained extend to hundreds of amperes. However, their power grid model is quite crude as they only consider a single line segment of 100 km in length. Even such a simple model can describe GIC qualitatively but a quantitative estimation requires a full modelling of the real power grid as is done in this paper.

6 Conclusions

The purpose of this study was to describe the two GIC events that occurred in Sweden during 13–14 July 1982 and 29–30

October 2003, both of which occurred a few years after the sunspot maximum.

In the first event, a solar flare was observed on 12 July, perhaps related to a CME from region 3804. The shock arrived at Earth around 16 UT on July 13 causing a SSC. The Dst index decreased to -325 nT and the Kp index reached values of 8 to 9 until the early hours next day, on 14 July.

In Sweden, close to Stockholm, the geomagnetic disturbance reached a maximum intensity around midnight when the north component B_x decreased by almost -5000 nT in a few minutes. The calculated electric field reached a maximum of around 3 and 6 V/km, for the E_x and E_y components. This was large enough to disturb the usual voltage of 3 to 5 V between the rails and over a relay and thus cause a malfunction of the railway signal system.

The second event, in October 2003, started with an X17 flare from the region 486 at 11:10 UT on 28 October. At 06:15 UT, on the following day, a halo-CME driven shock arrived at L1. This resulted in an extreme geomagnetic storm, with Kp=9 and Dst=-353 nT. In southern Sweden, the peak geomagnetic disturbance occurred at around 06:45 UT with B_y=$\sim$-2000 nT.

At 20:49 UT, on 29 October, a new flare, an X10, was observed. The second halo-CME caused a SSC at 16:20 UT on 30 October. The result was another extreme storm, with Kp=9 and Dst=-383 nT. This caused a peak total geomagnetic disturbance of about 2000 nT and a geoelectric field of about 2 V/km at 20:04 UT. The blackout in the city of Malmö, occurred at 20:07 UT and lasted for 20 to 50 minutes affecting about 50000 customers. The cause was a relay too sensitive to the third harmonics of the fundamental frequency. These harmonics were a result from transformer saturation due to GIC. Another peak, in the geomagnetic field, occurred at $\sim$21:20 UT, without any reported problems.

Acknowledgements. We thank Prof. Sture Lindahl (Gothia Power AB, Gothenburg, and Lund University, Sweden) and Mr. Håkan Swahn (E.ON, Sweden) for many useful discussions on GIC effects on power systems. Håkan Swahn is also acknowledged for providing measured GIC data and other important information about the Halloween storm.

We also thank Mr. Bertil Artelius (Banverket, Swedish Rail Administration) for providing us with technical information about GIC impacts on the Swedish railways and about geoelectric recordings in Sweden.

We are grateful to E.ON and Svenska Kraftnät (SVK, Sweden) for providing power grid data to us and for supporting us otherwise. We also thank all institutes providing magnetometer data to IMAGE and INTERMAGNET. We wish to thank Mr. Lasse Häkkinen (FMI, Finland) for helping us in collecting of magnetic data used in the study.

We thank the NOAA National Geophysical Data Center in Boulder, USA, and the World Data Center (WDC) for Geomagnetism in Kyoto, Japan.

We are thankful to NOAA, the ACE/MAG/SWICS teams and the SOHO/MDI team for solar and solar wind data. We also acknowledge the National Astronomical Observatory of Japan, Tokyo (NAOJ).

We acknowledge the IMP8/MIT and IMP8/LANL team and the National Space Science Data Center (NSSDC).

References

Amm, O., and Viljanen, A.: Ionospheric disturbance magnetic field continuation from the ground to the ionosphere using spherical elementary current systems, Earth Planets Space, 51, 431–440, 1999.

Bartels, J., Heck, N. H., and Johnston, H. F.: The three-hour-range index measuring geomagnetic activity, J. Geophys. Res., 44, 411–454, 1939.

Belov, A. V., Gaidash, S. P., Eroshenko, E. A., Lobkov, S. L., Pirjola, R., and Trichtchenko, L.: Effects of strong geomagnetic storms on Northern railways in Russia, Proceedings of the 7-th International Symposium on Electromagnetic Compatibility and Electromagnetic Ecology, Saint-Petersburg, Russia, June 26-29, 2007, 280–282, 2007.

Bolduc, L., Langlois, P., Boteler, D., Pirjola, R.: A study of geoelectromagnetic disturbances in Quebc, 1. General results, IEEE T. Power Delivery, 13, 1251–1256, 1998.

Bolduc, L., Langlois, P., Boteler, D., Pirjola, R.: A study of geoelectromagnetic disturbances in Quebc, 2. Detailed analysis of a large event, IEEE T. Power Delivery, 15, 272–278, 2000.

Bolduc, L.: GIC observations and studies in the Hydro-Québec power system, J. Atmos. Sol-Terr. Phy., 64 (16), 1793–1802, 2002.

Boteler, D. H., Pirjola, R. J., and Nevanlinna, H.: The effects of geomagnetic disturbances on electrical systems at the Earth's surface, Adv. Space Res., 22 (1), 17–27, 1998.

Davis, T. N., and Sugiura, M.: Auroral electrojet activity index AE and its universal time variations, J. Geophys. Res., 71, 3, 785–801, 1966.

Elovaara, J., Lindblad, P., Viljanen, A., Mäkinen, T., Pirjola, R., Larsson, S., and Kielén, B.: Geomagnetically induced currents in the Nordic power system and their effects on equipment, control, protection and operation, CIGRÉ General Session 1992, (CIGRÉ = International Conference on Large High Voltage Electric Systems), Paris, France, August 31 - September 5, 1992, Paper No. 36-301, 10 pp., 1992.

Gleisner, H., and Watermann, J.: Solar energetic particle flux enhancement as an indicator of halo coronal mass ejection geoeffectiveness, Space Weather, 4, S06006, doi:10.1029/2006SW000220, 2006.

Gomez-Trevino, E., Should the electric line be straight in magnetotelluric surveys?, Geophys. Prospect., 35, 920–923, 1987.

Gopalswamy, N., Yashiro, S., Liu, Y., Michalek, G., Vourlidas, A., Kaiser, M.L., and Howard, R.A.: Coronal mass ejections and other extreme characteristics of the 2003 October-November solar eruptions, J. Geophys. Res., 110, A09S15, doi:10.1029/2004JA010958, 2005.

Kappenman, J. G. and Albertson, V. D.: Bracing for the geomagnetic storms, IEEE Spectrum, March 1990, 27–33, 1990.

Kappenman, J. G.: Geomagnetic storms and their impact on power systems, IEEE Power Engineering Review, May 1996, 5–8, 1996.

Kappenman, J. G.: An overview of the impulsive geomagnetic field disturbances and power grid impacts associated with the violent Sun-Earth connection events of 29-31 October 2003 and a comparative evaluation with other contemporary storms, Space Weather, 3, S08C01, doi:10.1029/2004SW000128, 21 pp., 2005.

Kappenman, J. G.: Great geomagnetic storms and extreme impulsive geomagnetic field disturbance events - An analysis of observational evidence including the great storm of May 1921, Adv. Space Res., 38, 188-199, 2006.

Kasinskii, V. V., Ptitsyna, N. G., Lyahov, N. N., Tyasto, M. I., Villoresi, G., and Lucci, L.: Effect of Geomagnetic Disturbances on the Operation of Railroad Automated Mechanisms and Telemechanics, Geomagn. Aeronomy, 47 (5), 676–680, 2007.

Lam, H.-L., Boteler, D. H., and Trichtchenko, L.: Case studies of space weather events from their launching on the Sun to their impacts on power systems on the Earth, Ann. Geophys., 20, 1073–1079, 2002.

Lanzerotti, L. J., Thomson, D. J., and Maclennan, C. G.: Engineering issues in space weather, in Modern Radio Science 1999, edited by M. A. Stuchly, International Union of Radio Science (URSI), Oxford University Press, 25-50, 1999.

Lundstedt, H.: The sun, space weather and GIC effects in Sweden, Adv. Space Res., 37 (6), 1182–1191, 2006.

Maurer, H. and Theile, B.: Parameters of the Auroral Electrojet From Magnetic Variations Along a Meridian. J. Geophys., 44, 415–426, 1978.

Mavromichalaki, H., Belehaki, A., and Serdari, V.: Structure of the July 1982 event in relation to the Magnetosphere's response, Astrophys. Space Sci., 180, 173–183, 1991.

Molinski, T. S.: Why utilities respect geomagnetically induced currents, J. Atmos. Sol.-Terr. Phy., 64 (16), 1765–1778, 2002.

Pirjola, R.: On currents induced in power transmission systems during geomagnetic variations, IEEE T. Power Ap. Syst., PAS-104 (10), 2825–2830, 1985.

Ptitsyna, N. G., Tyasto, M. I., Kassinskii, V. V., Lyakhov, N. N., and Villoresi, G.: Do natural magnetic fields disturb railway telemetry?, Proceedings of the 7-th International Symposium on Electromagnetic Compatibility and Electromagnetic Ecology, Saint-Petersburg, Russia, June 26-29, 2007, 288–290, 2007.

Ptitsyna, N. G., Kasinskii, V. V., Villoresi, G., Lyahov, N. N., Dorman, L. I., and Lucci, N.: Geomagnetic effects on mid-latitude railways: A statistical study of anomalies in the operation of signaling and train control equipment on the East-Siberian Railway, Adv. Space Res., 42 (9), 1510–1514, 2008.

Pulkkinen, A., Lindahl, S., Viljanen, A., and Pirjola, R.: Geomagnetic storm of 29-31 October 2003: Geomagnetically induced currents and their relation to problems in the Swedish high-voltage power transmission system, Space Weather, 3, S08C03, doi: 10.1029/2004SW000123, 19 pp., 2005.

Skoug, R.M., Gosling, J. T., Steinberg, J. T., McComas, D. J., Smith, C. W., Ness, N. F., Hu, Q., and Burlaga, L. F.: Extremely high speed solar wind: 29-30 October 2003. J. Geophys. Res., 109, doi:10.1029/2004JA010494, 2004.

Stüdemann, W., and Wilken, B.: Multispacecraft observations at the compressed magnetopause following the 13 July 1982 interplanetary shock, Planet. Space Sci., 34, 9, 825–833, 1986.

Sugiura, M.: Hourly values of equatorial Dst for IGY, pp. 945–948, in Annals of the International Geophysical Year, vol. 35, Pergamon Press, Oxford, 1964.

Viljanen, A.: The relation between geomagnetic variations and their time derivatives and implications for estimation of induction risks, Geophys. Res. Lett., 24, 631–634, 1997.

Wallerius, A.: Solen gav Sverige en strömstöt (in Swedish), Ny Teknik - Teknisk Tidskrift, 29, 3, 1982.

Watermann, J.: The magnetic environment - GIC and other ground effects, in Space Weather, Research Towards Applications in Europe, edited by J. Lilensten, Springer, Chapter 5.0, 269–275, 2007.

Weaver, M., Murtaugh, W., Balch, C., Biesecker, D., Combs, L., Crown, M., Doggett, K., Kunches, J., Singer, H., and Zezula, D.: Halloween Space Weather Storms of 2003, NOAA Technical Memorandum OAR SEC-88, Department of Commerce, NOAA, Boulder, USA, 2004.

Wik, M., Viljanen, A., Pirjola, R., Pulkkinen, A., Wintoft, P., and Lundstedt, H.: Calculation of Geomagnetically Induced Currents in the 400 kV Power System in Southern Sweden, Space Weather, 6, S07005, doi:10.1029/2007SW000343, 2008.

Zurbuchen, T.H., Gloeckler, G., Ipavich, F., Raines, J., Smith, C. W., and Fisk, L. A.: On the fast coronal mass ejections in October/November 2003: ACE-SWICS results. Geophys. Res. Lett., 31, doi:10.1029/2004GL019461, 2004.

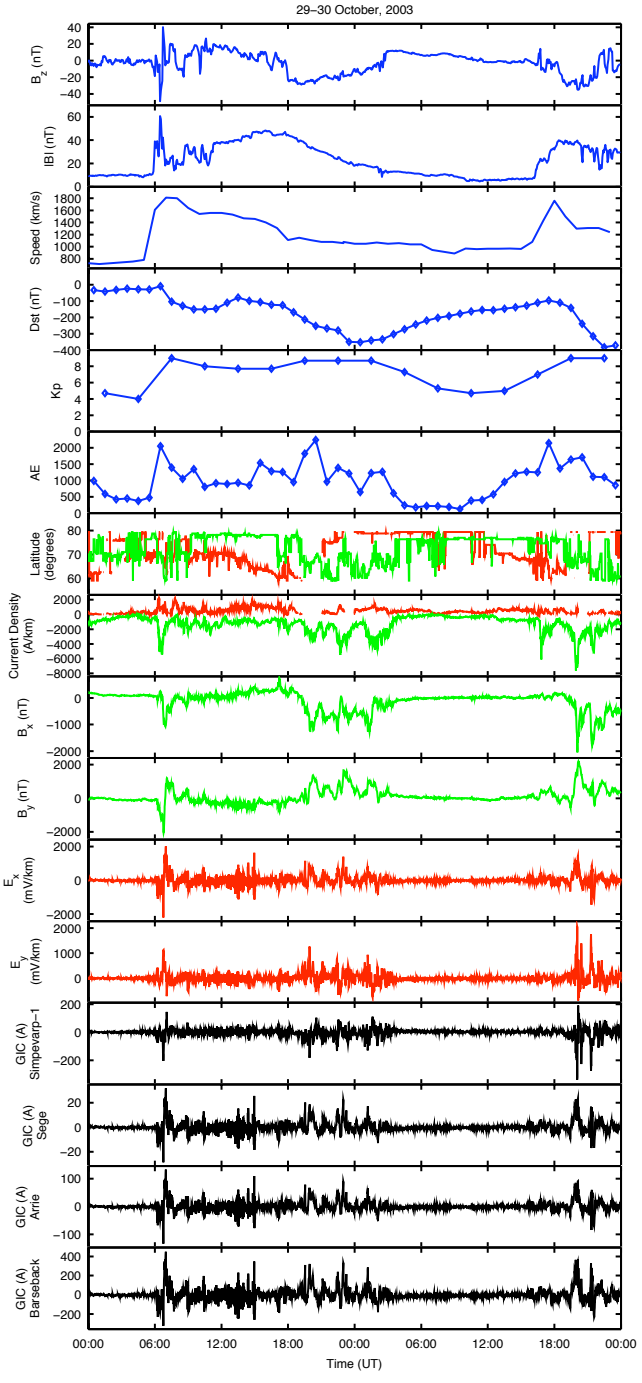

Fig. 7. Stack plot of ACE solar wind data, geomagnetic indices, electrojet parameters, horizontal geomagnetic and geoelectric data and geomagnetically induced currents for 29-30 October, 2003. The three top panels show the solar wind B_z component and magnetic field magnitude $|\mathbf{B}|$ from ACE/MAG and helium ion bulk speed from ACE/SWICS. The next three panels present the Dst, Kp and AE indices. The calculated electrojet latitude and intensity are shown in the next two panels. The interpolated geomagnetic and calculated geoelectric data depicted in the following four panels refer to the more southern red grid point in Figure 1. The four bottom panels present calculated GIC at Simpevarp-1, Sege, Arrie and Barsebäck (stations # 20, # 18, # 1 and # 3 in figure 2).

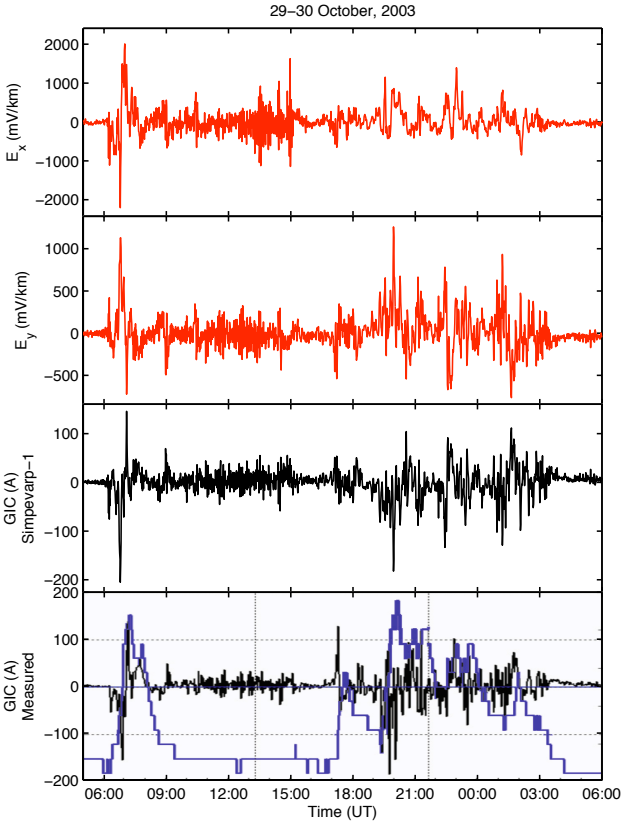

Fig. 8. Measured and calculated GIC at Simpevarp-1 (#20 in Figure 2) from 05 UT on 29 October to 06 UT on 30 October 2003 (black curve). The transformer temperature at Simpevarp-1 is also shown (blue curve). The total range from bottom to top in the figure for the temperature is roughly ten degrees. There are no measurements at later times on 30 October due to a problem with the monitoring system [private communication with Håkan Swahn]. For comparison, the electric field is also shown.

Paper C

Predictions of local ground geomagnetic field fluctuations during the 7-10 November 2004 events studied with solar wind driven models

Annales Geophysicae, 23, 3095–3101, 2005
SRef-ID: 1432-0576/ag/2005-23-3095

Annales Geophysicae

Predictions of local ground geomagnetic field fluctuations during the 7–10 November 2004 events studied with solar wind driven models

P. Wintoft[1], **M. Wik**[1], **H. Lundstedt**[1], **and L. Eliasson**[2]

[1]Swedish Institute of Space Physics, Lund, Sweden
[2]Swedish Institute of Space Physics, Kiruna, Sweden

Received: 22 February 2005 – Revised: 6 July 2005 – Accepted: 13 July 2005 – Published: 22 November 2005

Part of Special Issue "1st European Space Weather Week (ESWW)"

Abstract. The 7–10 November 2004 period contains two events for which the local ground magnetic field was severely disturbed and simultaneously, the solar wind displayed several shocks and negative B_z periods. Using empirical models the 10-min RMS ΔX and ΔY at Brorfelde (BFE, 11.67° E, 55.63° N), Denmark, are predicted. The models are recurrent neural networks with 10-min solar wind plasma and magnetic field data as inputs. The predictions show a good agreement during 7 November, up until around noon on 8 November, after which the predictions become significantly poorer. The correlations between observed and predicted log RMS ΔX is 0.77 during 7–8 November but drops to 0.38 during 9–10 November. For RMS ΔY the correlations for the two periods are 0.71 and 0.41, respectively. Studying the solar wind data for other L1-spacecraft (WIND and SOHO) it seems that the ACE data have a better agreement to the near-Earth solar wind during the first two days as compared to the last two days. Thus, the accuracy of the predictions depends on the location of the spacecraft and the solar wind flow direction. Another finding, for the events studied here, is that the ΔX and ΔY models showed a very different dependence on B_z. The ΔX model is almost independent of the solar wind magnetic field B_z, except at times when B_z is exceptionally large or when the overall activity is low. On the contrary, the ΔY model shows a strong dependence on B_z at all times.

Keywords. Magnetospheric physics (Solar wind-magnetosphere) – Geomagnetism and Paleomagnetism (Rapid time variations) – Ionosphere (Modeling and forecasting)

1 Introduction

The Earth's magnetosphere is a dynamic system that responds to changes in the upstream solar wind. Through complex processes that includes magnetic reconnection and viscous instabilities, energy is transferred from the solar wind into the magnetosphere (Baumjohann and Haerendel, 1987), with subsequent energy dissipation through geomagnetic storms and substorms (Gonzalez et al., 1994). A major fraction of large geomagnetic storms is caused by coronal mass ejections (CME) (Gosling et al., 1991). The CME, and its interplanetary counterpart, the ICME, plows through the ambient solar wind, producing shock waves and following sheath regions (Owens et al., 2005). In some cases the ICME evolves as a magnetic cloud (Burlaga, 1995) with smooth magnetic field line rotation during which the B_z component may be strongly negative for an extended period of time, enabling entry of solar wind energy through magnetic reconnection. Another source for geomagnetic activity, especially during the declining phase of solar activity, is seen in high speed solar wind streams (Richardson et al., 2002). The different structures interact and evolve as they travel from the Sun to the Earth, causing various degrees of geoeffectiveness (Huttunen et al., 2002; Echer and Gonzales, 2004).

During the geomagnetic storm, different current systems are modified, like the ionospheric currents, ring current, and magnetopause current. On the ground the currents are observed as deviations of the local geomagnetic field (Nishida, 1978). Several indices have been derived for various geophysical phenomena (Mayaud, 1980) and their coupling to the solar wind have been extensively studied (Baker, 1986), and especially the D_{st} index (Wu and Lundstedt, 1997; Klimas et al., 1998). The effects of geomagnetic disturbances are observed on technological systems, such as electrical power grids, pipe lines, and telegraph lines (Boteler et al., 1998, Lundstedt, 2004[1]), and are called geomagnetically

Correspondence to: P. Wintoft
(peter@lund.irf.se)

[1]Lundstedt, H.: The Sun, Space Weather and GIC Effects in Sweden, Adv. Space Res, in review, 2004.

induced currents (GIC). There is great interest in modelling GIC, both for post-event analysis and for predictions. As a result there are three parallel GIC studies within the ESA Space Weather Applications Pilot Project and these can be found at the web page http://www.esa-spaceweather.net/.

The GIC can be estimated in different ways. One approach is to use geomagnetic indices, as several can be successfully predicted: AE (Gleisner and Lundstedt, 2001a), D_{st} (Vassiliadis and Klimas, 1999; Lundstedt et al., 2002), and K_p (Boberg et al., 2000). The index is then translated into a physical quantity that is related to GIC. Boteler (2001) showed that there is close to a linear relationship between the 3-h K_p index and the logarithm of the ground electric field. However, the indices have their limitations because they have been derived to capture some specific aspect of the magnetospheric variation. Another approach is to use observed ground geomagnetic field data. The calculation of GIC can then be divided into two steps (Pirjola, 2002) involving a geophysical part to determine the geoelectric field and an engineering part to compute the currents in the technological system. The electric field is computed from the magnetic field by assuming an equivalent ionospheric current system such that the geomagnetic variations at the Earth's surface can be explained by horizontal divergence-free ionospheric currents (Viljanen et al., 2003). Solar wind–magnetosphere coupling models can then be used to predict the local ground magnetic field. In Gleisner and Lundstedt (2001b) a model was developed that predicts the 10-min average local geomagnetic field using solar wind data. But, as the electric field is related to the rate-of-change of the magnetic field (dB/dt) via Faraday's law of induction $\nabla\times E=-\frac{\partial B}{\partial t}$, a more basic quantity to use is the time difference of B, i.e. $\Delta B(t)=B(t+1)-B(t)$ (Viljanen et al., 2001). However, most of the power in ΔB is located at small scales (high frequencies) and therefore a large fraction of the signal will be lost if ΔB is temporally averaged, or if ΔB is formed from a temporally averaged B (Wintoft, 2005). This happens already at 5 to 10 min averages. Therefore, other moments of ΔB should be considered. In the work by Weigel et al. (2002) models were developed that predict the average absolute value of ΔB with a temporal resolution of 30 min. More specifically, they studied the north-south component of the magnetic field, i.e. $\langle|\Delta X|\rangle_{30\mathrm{min}}$. As the average is taken of the absolute value, a large fraction of the variance from the original signal is maintained. The best model reached an overall prediction efficiency of 0.4 based on data from 1998–1999.

The models developed by Wintoft (2005) aims instead at predicting the 10-min root-mean-square (RMS) of ΔX (and ΔY). The motivation of using RMS data is summarised here. The power spectrum of ΔX peaks at small scales and decreases quickly with increasing scale: 83% of the power is located at scales $\tau\leq 8$ min, 99% at $\tau\leq 128$ min. We speak in terms of scales as defined from wavelet analysis, but the scale may be translated into the approximate frequency band $[1/4\tau, 1/2\tau]$ (Percival and Walden, 2002). One may also picture the signal at a certain scale as being the difference between two consecutive averages of width τ. It was found that the RMS data can be used to estimate the power spectra of ΔX and ΔY. This is useful for the subsequent analysis, for example, computing GIC, as both amplitude and scale (frequency) are available. Another issue is that the RMS data captures a major fraction of the variance in ΔX. The relative variance is $\mathrm{Var}(\mathrm{RMS}\Delta X)/\mathrm{Var}(\Delta X)=0.82$. For comparison the 10-min average absolute ΔX has a relative variance of $\mathrm{Var}(\langle|\Delta X|\rangle)/\mathrm{Var}(\Delta X)=0.55$. Finally, any temporal averaging will decrease the forecast lead time. To illustrate this we may consider a time dependent parameter $x(t)$ that is collected with a sampling interval Δt that results in the time series x_i. The corresponding time stamp t_i marks the beginning of the interval so that x_i is the average of $x(t)$ over the interval $t\in[t_i, t_{i+1}]$, where $t_{i+1}=t_i+\Delta t$. Similarly, we may have another variable $y(t)$ sampled to y_i. If we now wish to develop a model that predicts y from x with lead time T we have $\hat{y}(t+T)=f(x(t))$, where $\hat{y}$ is the prediction of y. This leads to the discrete model $\hat{y}_{i+k}=f(x_i)$ where $T=k\Delta t$. Now assume that the current time is t_0. The latest available input is x_{-1} and it has been collected over the time interval $[t_{-1}, t_0]$. With a forecast time of $T=k\Delta t$ we will therefore forecast y_{k-1}, resulting in a true forecast time of $T'=T-\Delta t$. In order for the model to perform actual forecasts, we must have $\Delta t\leq T$.

In this work we will use the previously developed models to predict the disturbed period during 7 to 10 November 2004. The following section describes the observed data, Sect. 3 describes the model, Sect. 4 address forecast errors related to the location of the solar wind monitor and the control of the IMF B_z component. In Sect. 5 the conclusions are given.

2 The 7–10 November 2004 events

The 7–10 November 2004 period contains two events for which the local ground magnetic field was severely disturbed and the solar wind displays several shocks and negative B_z periods. In Fig. 1 the solar wind plasma and magnetic field data are shown, together with the ground magnetic field deviations at Brorfelde (BFE, 11.67° E, 55.63° N). The deviations are the one-minute differences of the north-south (X) and east-west (Y) magnetic field components

$$\Delta X(t) = X(t+1) - X(t), \tag{1}$$

$$\Delta Y(t) = Y(t+1) - Y(t), \tag{2}$$

as approximations to dX/dt and dY/dt. The solar wind data comes from three spacecraft: ACE (blue line), WIND (green line), and SOHO (red dots). The ACE (Smith et al., 1998; McComas et al., 1998) and WIND (Ogilvie et al., 1995) data have been resampled to 10-min averages while the SOHO (Ipavich et al., 1998) data are one-hour averages. The four top panels show the particle density n, the standard deviation σ_n of the density, the B_z magnetic field component in GSM, and the velocity V. The next two panels show the one-minute differences ΔX and ΔY. The two panels also contain the

10-min root-mean-square (RMS) of ΔX and ΔY. The bottom panel shows the north-south magnetic field X, minus 17 150 nT, and the D_{st} index. The five vertical lines indicates the times of solar wind shocks. It is clear that these shocks are followed by sudden increases in $|\Delta X|$ and $|\Delta Y|$. As the geomagnetic storm develops, large variations in ΔX and ΔY are seen. During 8 November, the extreme values reach (ΔX, ΔY)=(140, 116) nT/min and during 9 November (ΔX,ΔY)=(-242, -229) nT/min. The corresponding 10-min RMS extreme values are (96,61) nT/min and (122, 104) nT/min, respectively. We also note that the ratio RMSΔX/RMSΔY decreases from 1.6 for 8 November event to 1.2 for the 9 November event, indicating that the disturbance is more along the north-south direction during the first event. These events have not yet been described in the scientific literature, however, a description can be found at Space Environment Center (http://www.sec.noaa.gov/weekly/).

We see that the Sun was very active with several CMEs. The first shock in early 7 November was probably caused by a CME on 3 November. There was a small increase in the solar wind magnetic field with a negative B_z component. Both ΔX and ΔY display an impulse 66 min later in accordance with the ACE-magnetopause travel time of $t_{\rm ACE}$=68 min at the velocity of 365 km/s. The second shock, caused by a CME on 4 November was accompanied with larger increases in particle density n, σ_n, and B. B_z turned initially northward and later southward. The shock was followed by a magnetic impulse 55 min later, again in agreement with the 420 km/s velocity ($t_{\rm ACE}$=59 min). Both ΔX and ΔY continued to be slightly disturbed and D_{st} showed a weak increase followed by a weak decrease typical for the magnetic storm initial and main phases. At the third shock the velocity jumped from 500 km/s to above 650 km/s, the magnetic field increased to almost 50 nT and B_z turned initially northward and later strongly southward for an extended period of time. The source for this event was probably a series of CMEs that occurred late on 4 and early 6 November. The magnetic impulse took place 33 minutes later, in good agreement with a velocity of 650 km/s ($t_{\rm ACE}$=38 min). The disturbed period continued for about 19 h and D_{st} reached -373 nT on 8 November. What looks like a magnetic impulse early in 9 November is most likely a spurious value, as there are data gaps around that point and other stations show no such feature. The fourth shock, around noon on 9 November shows quite different velocities for ACE/WIND and SOHO. The magnetic impulse occurs 16 min after the shock and is similar in strength to that after the second shock. With a velocity of $V_{\rm ACE}$=790 km/s there should be a delay of $t_{\rm ACE}$=32 min. It is thus difficult to associate this magnetic impulse with the measured solar wind at ACE. The fourth shock shows a jump in velocity from 650 km/s to 800 km/s and a magnetic impulse follows 29 min later, in agreement with $t_{\rm ACE}$=31 min.

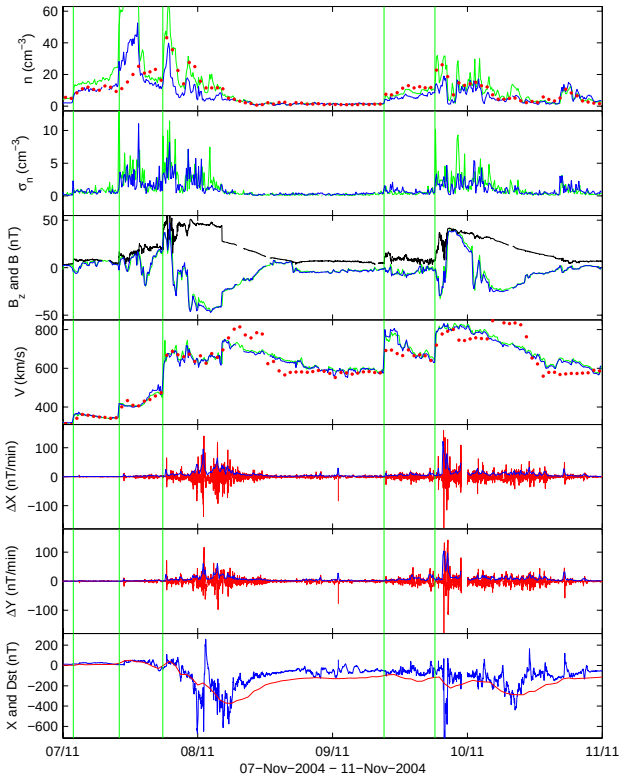

Fig. 1. The panels show, from top to bottom: solar wind density n (ACE–blue, WIND–green, SOHO–red), standard deviation σ_n of the density, B_z magnetic field component in GSM and total field B from ACE (black), velocity V, one-minute ΔX (red) and 10-min RMS ΔX (blue), one-minute ΔY and 10-min RMS ΔY, and one minute X (blue) and hourly D_{st} (red). The period extends over the four days of 7–10 November 2004. The only available data from SOHO are the hourly average density and velocity.

3 Forecasting RMS (ΔX,ΔY) using ACE

The empirical models previously developed predict the 10-min RMS ΔX and ΔY for southern Scandinavia, with a prediction lead time of 30 min (Wintoft, 2005). The models are recurrent neural networks with solar wind plasma and magnetic field data as inputs: 10-min averages of magnetic field B_z, particle density n, velocity V, and standard deviations (σ) of the same parameters. Local time and time of year were also used.

The models were trained and validated on data from the six year period 1998–2003. As the distributions of RMS ΔX and ΔY are dominated by values close to zero only a selected subset was used, in order to avoid the network becoming biased towards quiet conditions. However, large values are still typically underestimated, as they are more infrequent. The prediction horizon of 30 min was selected to enable the models to predict events with a large range of solar wind velocities. A velocity of 830 km/s at L1 takes 30 min to reach the magnetopause. We also studied models where the prediction lead time was increased up to 90 min, but for both ΔX and ΔY the correlation decreased. A large set of neural

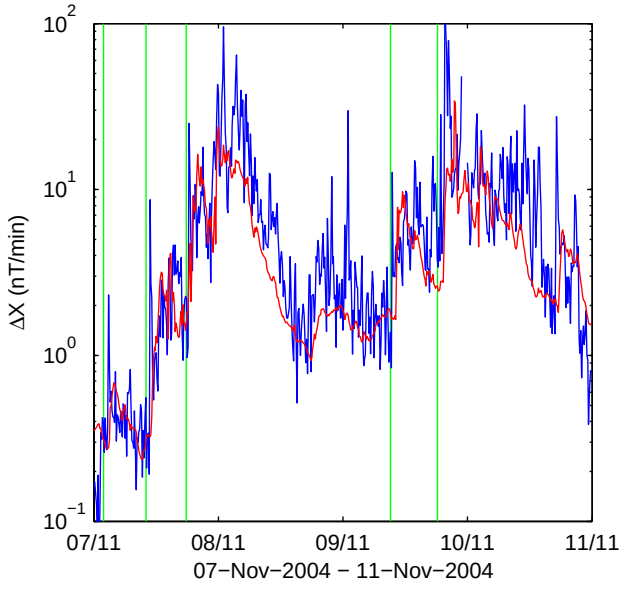

Fig. 2. The figure shows the observed (blue) and predicted (red) 10-min RMS ΔX.

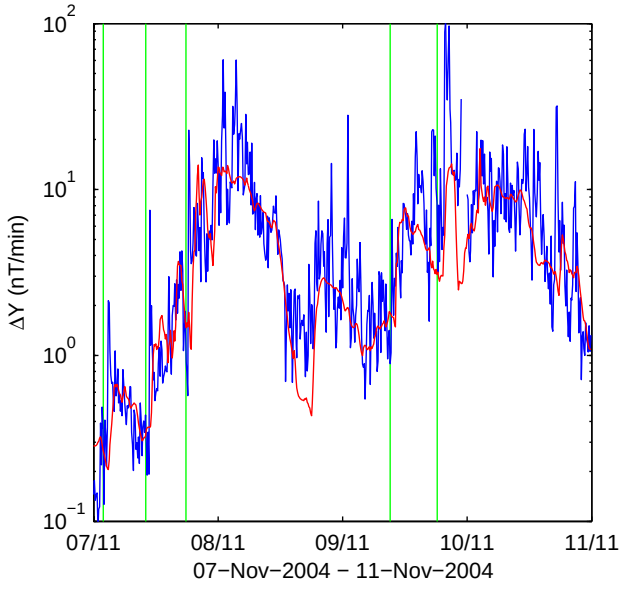

Fig. 3. The figure shows the observed (blue) and predicted (red) 10-min RMS ΔY.

networks were trained and the optimal models gave a correlation of 0.79 and prediction efficiency (Detman and Vassiliadis, 1997) of 0.63 of the logarithm of the RMS data. It is important to notice here that the geomagnetic data are not used as input to the model, only solar wind data, otherwise the correlation could be even higher but not necessarily truly improving the predictions. For example, a simple persistence model, predicting RMS $\Delta X(t+30\,\text{min})$ based on RMS $\Delta X(t)$, would have a correlation of 0.72 but the predictions would consistently lag by 30 min. To verify that the solar wind–ΔX model is actually making 30 min forecasts, with the stated correlation, we may compute the correlation coefficient between the observed ΔX and the predicted ΔX by shifting the predicted ΔX backwards and forwards in time. For a true forecast the maximum correlation should occur at 30 min and decrease for smaller and larger prediction times, and this is also the case for the neural network models.

It was shown that the solar wind influence on ΔX and ΔY were slightly different. The most important inputs for ΔX, in order of increasing importance, were local time, B_z, σ_n, and V. For ΔY it was local time, σ_n, V, and B_z. The other inputs, and mots notably n, had no significant influence. The independence of n was also shown by Weigel et al. (2002). The models have been implemented for real time operation and the forecasts are displayed on a web page (http://www.lund.irf.se/gicpilot/gicforecastprototype/). The predictions of RMS ΔX and ΔY for the November events are shown in Figs. 2 and 3. It is seen that the predictions capture the large-scale variations but not the sample-to-sample variations. The predictions show a good agreement during 7 November, up until around noon on 8 November, after which the predictions become significantly poorer. The correlations between observed and predicted log RMS ΔX is 0.77 during 7–8 November but drops to 0.38 during 9–10 November. For RMS ΔY the correlation for the two periods are 0.71 and 0.41, respectively.

4 Discussion

In the following sections we address the forecast quality in relation to the location of the solar wind monitor and study the coupling to the solar wind B_z component.

4.1 The locations of solar wind monitors

The ACE spacecraft is in orbit around L1 approximately 240 Earth radii (R_E) upstream from Earth. Due to the large distance there may be considerable differences in solar wind properties at ACE and close to Earth. In the study by Dalin et al. (2002) it was shown that the correlation of solar wind plasma data from different spacecraft could, at times, be small and the correlation decreased with increasing (Y,Z)-separation. For the period studied here the ACE spacecraft is located approximately at (X,Y,Z)=(242, 23, −15) R_E in GSE coordinate system. Two other spacecraft are also located around L1, namely SOHO at (218, −104, −3) R_E and WIND at (199, 59, −9) R_E. The spacecraft are almost located in the (X,Y)-plane, with the largest separation of 12 R_E in the Z-direction. However, in the Y-direction the distance is as large as 163 R_E. In the X-direction the separation is about 42 R_E, and with a velocity of 400 km/s or higher the separation in time is less than 11 minutes. From Fig. 1 we see that the B_z magnetic field components for ACE and WIND are very well correlated. There is a shift of $<$10 min, barely visible in the figure, that comes from the separation in X. Studying the velocity, there is again a very good agreement between ACE

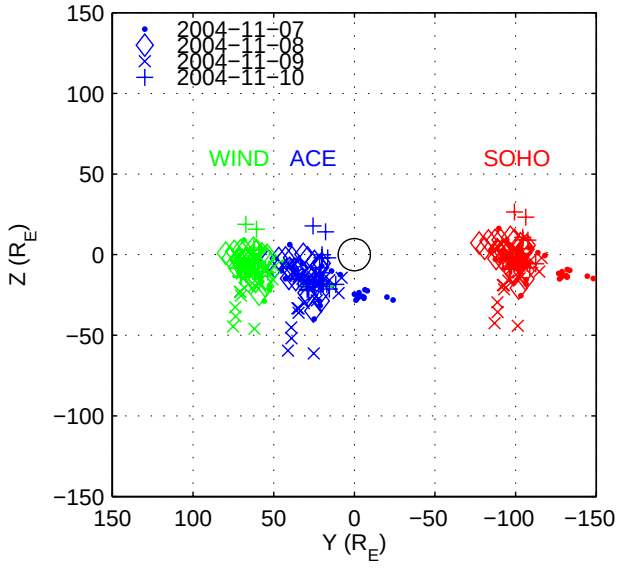

Fig. 4. The figure shows the advected spacecraft locations onto the plane X=10 R_E using hourly average velocity vectors from WIND. The data have been divided into the four days: 7 November (dots), 8 November (diamonds), 9 November (crosses), and 10 November (pluses). The black circle is centred on Earth and has a radius of 10 R_E.

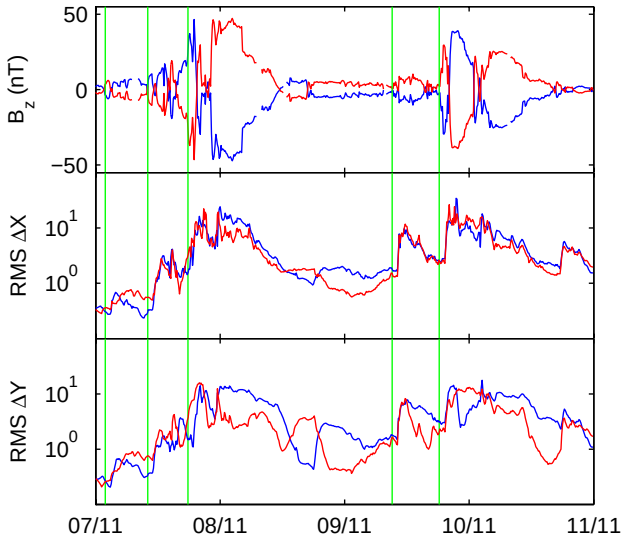

Fig. 5. The three panels show, from top to bottom: solar wind B_z (blue) and $-B_z$ (red), predicted RMS ΔX using B_z (blue) and $-B_z$ (red), and predicted RMS ΔY using B_z (blue) and $-B_z$ (red).

and WIND. The hourly average SOHO velocity data show a good agreement during 7 November, up to 05:00 UT on 8 November, despite its large distance from ACE and WIND. After that, the SOHO velocity deviates significantly most of the time. It thus seems that the velocity structure is homogenous at the beginning of the period and then becomes more fragmented. The ACE and WIND densities show similar temporal variation, although WIND mostly gives higher densities, often by a factor 2 to 3. Except for the first part of 7 November, the SOHO density agrees quite well with the WIND density.

In Fig. 4 the crossing of the solar wind in the (Y, Z)-plane at X=10 R_E (typical megnetopause distance) is shown for the three spacecraft. As we only have all three velocity components for WIND, we have assumed the same velocity for the three spacecraft. The circle in the centre has a radius of 10 R_E. We see that the measurements at ACE advected to X=10 come reasonably close to the Earth during 7 November (dots). The most distant points are the two westerly dots, but simultaneously the WIND measurements come close to the Earth, and as ACE and WIND show a very good agreement for the whole period, we may conclude that the measurements at ACE depicts quite well what the solar wind is like close to the Earth during 7 November. Then, during 8 November, the advected location of ACE (diamonds) moves towards the east and south. During this day the velocities at SOHO and ACE also start to deviate. Then, during 9 November, the advected ACE location turns far south (crosses) of the Earth. It is thus possible that the measurements at ACE from the morning of 8 November through 9 November do not represent accurately the solar wind close to the Earth.

Turning back to the predictions shown in Figs. 2 and 3, it was seen that the correlation was higher during the first two days as compared to the last two days. Thus, this may be the result that the solar wind at ACE correlates well with the solar wind close to the Earth in the early part of the period but not later in the period. The errors are particularly large during the late evening to midnight on 9 November. Studying another model that predicts the geomagnetic index D_{st} (Lundstedt et al., 2002), also using ACE data as input, reveals that the prediction errors are large for the same hours.

4.2 The influence of B_z

Using the prediction models the influence of the solar wind on RMS ΔX and ΔY may be studied. In principal, some interesting artificial values could be selected to represent the solar wind to study the response of the model. However, care has to be taken so that the data represent a valid physical and statistical configuration, otherwise the output from the model will not be correct. One parameter that can be easily studied is B_z. It is perfectly valid to change the sign on B_z and run the models, as we expect that the direction of B is not correlated with density or velocity. For example, a magnetic cloud starts with a simultaneous increase in n, V, and B (Burlaga, 1995). But B_z may initially either turn northward or southward, with the subsequent evolution determined by the cloud topology. The result is shown in Fig. 5. The blue curve represents the original B_z and the red curve $-B_z$ (top panel). The model outputs are shown accordingly, in blue and red (bottom panels). The first apparent observation is that RMS ΔX shows a weak coupling to B_z, as changing the sign has very little effect on the output. On the contrary, RMS ΔY is much more affected.

Looking at the details we note that the variations in the two predictions of RMS ΔX are very similar up to 23:00 UT on 7 November, even though the sign on B_z has been changed. During the following hours, when B_z is strongly negative, up to 05:00 UT on 8 November there is a difference of about a factor 2. Then, the predictions coincide again when B_z goes towards zeros and the velocity decreases. But then, during a period of low activity from 12:00 UT on 8 November to 09:00 UT on 9 November, when B_z is close to zero, there is again a difference of a factor 2, with slightly higher activity when B_z is negative.

5 Conclusions

In this work we have studied the prediction of the 10-min variation of the local ground magnetic field, more specifically, the 10-min RMS ΔX and ΔY. The prediction model uses the solar wind data from the ACE spacecraft. The four-day period extending over 7 November to 10 November 2004 was explored.

It was found that the sample-to-sample variations in RMS ΔX and ΔY are not predicted, but the large-scale variations are predicted. The predictions of the first two days show a higher correlation with the observations than during the last two days. By studying the solar wind data for other L1-spacecraft (WIND and SOHO), it seems that the ACE data have a better agreement to the near-Earth solar wind during the first two days as compared to the last two days. In a study by Dalin et al. (2002) it was also shown that the correlation of solar wind plasma data from different spacecraft decreased with increasing (Y, Z)-separation. Thus, the accuracy of the predictions depends on the location of the spacecraft and the solar wind flow direction.

The models have not been developed to predict the response of ΔX or ΔY for specific solar wind structures; the only criterion used on the data selection is that there should be contiguous data for 48 h, or longer, for which RMS >10 nT/min at least once. This means that solitary peaks in RMS ΔX or ΔY will be difficult to model because of the low relative occurrence rate. However, the peaks may also be related to magnetic impulse events (Kataoka et al., 2003) that show a significant correlation to discontinuities of the interplanetary magnetic field, and not B_z, therefore, additional inputs should be considered in future studies.

By modifying the solar wind input data the response of the model may be studied. Care has to be taken in how the input is modified, but a valid modification from a physical and statistical point of view is to change the sign of B_z. It was found, for the events studied here, that the ΔX and ΔY models showed a very different dependence on B_z. The ΔX model is almost independent of the solar wind magnetic field B_z, except at times when B_z is large or when the overall activity is low. On the contrary, the ΔY model shows a strong dependence on B_z at all times.

In the models developed by Wintoft (2005) the location of ACE was not considered. Thus, it is reasonable to believe that there are data in the solar wind data set used for model development that are poorly correlated to the near-Earth solar wind. The inclusion of such data during the model development has the effect of increased noise. In future work, a more careful selection of data, taking into account the location of ACE, should be considered.

Acknowledgements. We are grateful to the providers of the solar wind and ground magnetic field data: ACE data from CalTech and SEC; the MIT Space Plasma Group for the WIND plasma data and NASA/GSFC for the WIND magnetic field data; the University of Maryland for the SOHO/PM data; the Solar-Terrestrial Physics Division at the Danish Meteorological Institute for the Brorfelde magnetic field data. COST 724 is acknowledged for financial support. This work has been carried out with support from ESA/ESTEC (Contract No. 16953/02/NL/LvH).

Topical Editor T. Pulkkinen thanks J. B. Blake and another referee for their help in evaluating this paper.

References

Baker, D. N.: Statistical analyses in the study of solar wind-magnetosphere coupling, Solar Wind-Magnetosphere Coupling, 17–38, 1986.

Baumjohann, W. and Haerendel, G.: Entry and dissipation of energy in the Earth's magnetosphere, in Space Astronomy and Solar System Exploration: Proceeding of summer school held at aplbach, Austria, 29 July–8 August, 1986, 121–130, ESA, 1987.

Boberg, F., Wintoft, P., and Lundstedt, H.: Real time K_p predictions from solar wind data using neural networks, Physics and Chemistry of the Earth, 25, 275–280, 2000.

Boteler, D.: Assessment of geomagnetic hazards to power systems in Canada, Natural Hazards, 23, 101–120, 2001.

Boteler, D. H., Pirjola, R. J., and Nevanlinna, H.: The effects of geomagnetic disturbances on electrical systems at the Earth's surface, Adv. Space Res., 22, 17–27, 1998.

Burlaga, L. F.: Interplanetary magnetohydrodynamics, Oxford University Press, 1995.

Dalin, P., Zastenker, G., Paularena, K., and Richardson, J.: The main features of solar wind plasma correlations of importance to space weather strategy, J. Atmos. S.-P., 64, 737–742, 2002.

Detman, T. R. and Vassiliadis, D.: Review of techniques for magnetic storm forecasting, 253–266, AGU, 1997.

Echer, E. and Gonzales, W. D.: Geoeffectiveness of interplanetary shocks, magnetic clouds, sector boundary crossings and their combined occurrence, Geophys. Res. Lett., 31, L09 808, 2004.

Gleisner, H. and Lundstedt, H.: Auroral electrojet predictions with dynamic neural networks, J. Geophys. Res., 106, 24 541–24 550, 2001a.

Gleisner, H. and Lundstedt, H.: Neural network-based local model for prediction of geomagnetic disturbances, J. Geophys. Res., 106, 8425–8433, 2001b.

Gonzalez, W. D., Joselyn, J. A., Kamide, Y., Kroehl, H. W., Rostoker, G., Tsurutani, B. T., and Vasyliunas, V. M.: What is a geomagnetic storm?, J. Geophys. Res., 99, 5771–5792, 1994.

Gosling, J. T., McComas, D. J., Phillips, J. L., and Bame, S. J.: Geomagnetic activity associated with Earth passage of interplanetary shock disturbances and coronal mass ejections, J. Geophys. Res., 96, 7831–7839, 1991.

Huttunen, K. E. J., Koskinen, H. E. J., and Schwenn, R.: Variability of magnetospheric storms driven by different solar wind pertubations, J. Geophys. Res., 107, SMP 20–1–8, 2002.

Ipavich, F. M., Galvin, A. B., Lasley, S. E., Paquette, J. A., Hefti, S., Reiche, K., Coplan, M. A., Gloeckler, G., Bochsler, P., Hovestadt, D., Grünwaldt, H., Hilchenbach, M., et al.: Solar wind measurements with SOHO: The CELIAS/MTOF proton monitor, J. Geophys. Res., 103, 17 205–17 213, 1998.

Kataoka, R., Fukunishi, H., and Lanzerotti, L. J.: Statistical identification of solar wind origins of magnetic impulsive events, J. Geophys. Res., 108, SMP 13–1–12, 2003.

Klimas, A. J., Vassiliadis, D., and Baker, D. N.: D_{st} index prediction using data-derived analogues of the magnetospheric dynamics, J. Geophys. Res., 103, 20 435–20 448, 1998.

Lundstedt, H., Gleisner, H., and Wintoft, P.: Operational forecasts of the geomagnetic *Dst* index, Geophys. Res. Lett., 29, 34–1–34–4, 2002.

Mayaud, P. N.: Derivation, meaning, and use of geomagnetic indices, Geophysical Monograph Series, AGU, 1980.

McComas, D. J., Bame, S. J., Barker, P., Feldman, W. C., Phillips, J. L., Riley, P., and Griffee, J. W.: Solar wind electron proton alpha monitor (SWEPAM) for the Advanced Composition Explorer, Space Science Reviews, 86, 563–612, 1998.

Nishida, A.: Geomagnetic Diagnosis of the Magnetosphere, 9 of Physics and Chemistry in Space, Springer-Verlag, 1978.

Ogilvie, K. W., Chornay, D. J., Fritzenreiter, R. J., Hunsaker, F., Keller, J., Lobell, J., Miller, G., Scudder, J. D., Sittler, Jr., E. C., Torbert, R. B., Bodet, D., Needell, G., Lazarus, A. J., et al.: SWE, a comprehensive plasma instrument for the WIND spacecraft, Sp. Sc. R., 71, 55–77, 1995.

Owens, M. J., Cargill, P. J., Pagel, C., Siscoe, G. L., and Crooker, N. U.: Characteristic magnetic field and speed properties of interplanetary coronal mass ejections and their sheath regions, J. Geophys. Res., 110(A01), 105, 2005.

Percival, D. B. and Walden, A. T.: Wavelet methods for time series analysis, Cambridge University Press, 2002.

Pirjola, R.: Review on the calculation of surface electric and magnetic fields and of geomagnetically induced currents in ground-based technological systems, Surv. Geophys., 23, 71–90, 2002.

Richardson, I. G., Cane, H. V., and Cliver, E. W.: Sources of geomagnetic activity during nearly three solar cycles, J. Geophys. Res., 107, SSH 8–1–13, 2002.

Smith, C. W., L'Heureux, J., Ness, N. F., Acuña, M. H., Burlaga, L. F., and Scheifele, J.: The ACE magnetic fields experiment, Space Sci. R., 86, 613–632, 1998.

Vassiliadis, D. and Klimas, A. J.: The $D_s t$ geomagnetic response as a function of storm phase and amplitude and the solar wind electric field, J. Geophys. Res., 104, 24 957–24 976, 1999.

Viljanen, A., Nevanlinna, H., Pajunpää, K., and Pulkkinen, A.: Time derivate of the horizontal geomagnetic field as an activity indicator, Ann. Geophys., 19, 1107–1118, 2001,
SRef-ID: 1432-0576/ag/2001-19-1107.

Viljanen, A., Pulkkinen, A., Amm, O., Pirjola, R., Korja, T., and BEAR Working Group: Fast computation of the geoelctric field using the method of elementary current systems and planar Earth models, Ann. Geophys., 22, 101–113, 2004,
SRef-ID: 1432-0576/ag/2004-22-101.

Weigel, R. S., Vassiliadis, D., and Klimas, A. J.: Coupling of the solar wind to temporal fluctuations in ground magnetic fields, Geophys. Res. Lett., 29, 2002.

Wintoft, P.: Study of the Solar Wind Coupling to the Time Difference Horizontal Geomagnetic Field, Ann. Geophys., 23, 1949–1957, 2005,
SRef-ID: 1432-0576/ag/2005-23-1949.

Wu, J.-G. and Lundstedt, H.: Neural network modeling of solar wind–magnetosphere interaction, J. Geophys. Res., 102, 14 457–14 466, 1997.

Paper D

Sunspot records as proxy for
total solar irradiance

Annales Geophysicae (2008) 0000: 0001–22
SRef-ID: 1432-0576/ag/2008-0000-0001

LOGO

Sunspot records as proxy for total solar irradiance

P. Wintoft, M. Wik, and H. Lundstedt

Swedish Institute of Space Physics, Lund, Sweden

Abstract. The total solar irradiance (TSI) has a direct influence on the Earth's weather and climate. Measurements of TSI extends back to 1978. To reach further back in time different proxies are used to reconstruct TSI. The available solar indices are the group sunspot number (R_g, from 1610), the sunspot number (R_z, from 1749), and the sunspot area (SSA, from 1874). In this work we study the statistical relation between the solar indices and TSI by decomposing the time series using wavelet analysis. We find that TSI is highly correlated with each index on time scales above 1–3 years. On shorter time scales the correlation is more complex. For R_g the correlation drops to zero, while R_z and SSA becomes anti-correlated with maximum strength around 1–4 months, where SSA shows the strongest anti-correlation. This complex behaviour may be explained by the simultaneous effects of brightening and dimming due to faculae and sunspots, respectively, that evolve over different time scales. Thus, to reconstruct TSI the series should be filtered with a cut-off around 1–3 years separating the high frequency component from the low frequency component. Another finding was that it is very difficult to understand the relation on time scales longer than the 11-year cycle because of the limited extent of TSI.

1 Introduction

Solar activity affects the Earth via radiation and plasma processes. The most apparent parameter affecting the Earth's climate and weather is the amount of incoming radiation that reaches the Earth's atmosphere. The total solar irradiation (Fröhlich, 2000), TSI, measures the wavelength integrated radiation outside the Earths atmosphere. Although absolute observations of TSI are difficult the relative observations can be made accurately. The observed TSI varies over all time scales from days to tens of years with a maximum variation of a few percent. Other important effects are the UV radiation heating the stratosphere (Haigh, 2007), magnetospheric processes that couple to the ionosphere and upper atmosphere (Boberg and Lundstedt, 2002; Bochníček and Hejda, 2005), and the modulation of cosmic rays affecting the atmospheric electric field (Tinsley, 2000) and the cloud coverage (Svensmark and Friis-Christensen, 1997). The variability in each of these parameters is much larger than the variability in TSI, but their effects on the Earth's atmosphere is also more complex and not yet well understood.

The observed TSI series extends back to 1978 and builds on several different spacecraft. To extend the series further back in time some proxy data are needed. Several different models exist that reconstruct TSI using the sunspot number (R_z), the group sunspot number (R_g), or the sunspot area (SSA) or a combination of them: Lean et al. (1995); Solanki and Fligge (1999); Sofia and Li (2001); Krivova et al. (2007); Tapping et al. (2007). In Lean et al. (1995) annual TSI and UV are reconstructed using the sunspot record from 1610. The model has two components, one that captures variability of TSI on solar cycle scales and another that captures variability on longer time scales. In addition the reconstruction is different before and after 1876. Before 1876 only the group sunspot number (Hoyt and Schatten, 1998) is used, while after 1876 a two-parameter model is used, sunspot darkening from Greenwich Observatory and facular brightening. The facular brightening is in turn determined from the monthly mean sunspot numbers. The R_g series extends back to 1610, while R_z and SSA go back to 1700 and 1874, respectively.

The Wolf sunspot number (Waldmeier, 1961), or just sunspot number, R_z is a weighted sum according to

$$R_z = k\,(n + 10g) \tag{1}$$

where n is the number of individual spots, g is the number of groups, and k is a correction factor accounting for observational effects. It is important to note that the sunspot number is not simply a count of the number of spots. The equation above was introduced by Rudolf Wolf in the 1850s to emphasise large scale evolution of the magnetic fields.

Correspondence to: P. Wintoft (peter@lund.irf.se)

The group sunspot number R_g (Hoyt and Schatten, 1998) was constructed to be a more internally self-consistent and less noisy than R_z. It is defined as

$$R_g = \frac{12.08}{N} \sum k_i' g_i \tag{2}$$

where g_i is the number of observed groups by observer i and k_i is the ith observer's correction factor. The factor 12.08 is to make R_g numerically equal to R_z. This definition allows more observers to be included and to extend the series further back in time.

The sunspot area SSA is the most physical variable of the three. It relies on measuring the total area covered by sunspots, whereas R_z and R_g build on the more abstract process of identifying spots and groups of spots.

The variation of TSI depends in a complex way on the photospheric magnetic fields such that magnetic flux tubes causing sunspots lead to a dimming in TSI whereas magnetic fields causing faculae lead to a brightening in TSI. In Krivova et al. (2003) a model was suggested that could explain basically all variation in TSI from observed solar surface magnetic fields from daily to solar cycle time scales. However, there are several magnetic field components that enter a magnetic field-TSI model whereas R_z is a single time series. But, as sunspots and faculae evolve on different time scales an R_z-TSI model can be constructed using a combination of different temporal averages to divide R_z into a slow and a fast component (Solanki and Fligge, 1999).

In this work we will study how TSI is related to R_z, R_g, and SSA over different temporal scales. We start with a short description of the data, we then discuss the effect of applying temporal averages before we move on to the wavelet analysis. Then we look at different models to reconstruct TSI, and finally we conclude on our findings.

2 Data

The TSI data were compiled from six different satellites covering the period 1978 to present (Fröhlich and Lean, 1998) and were obtained from NOAA's National Geophysical Data Center[1]. The data set has a temporal resolution of 1 day.

The sunspot area series goes back to 1874 and was obtained from NASA. Data after 1976 include a correction factor.[2] The data set has a temporal resolution of 1 day.

Daily sunspot numbers extend back to 1818, monthly values go back to 1749, and yearly values to 1700. The data were obtained from the Solar Influences Data Center[3] in Belgium.

[1] ftp://ftp.ngdc.noaa.gov/STP/SOLAR_DATA/-SOLAR_IRRADIANCE/composite_d25_07_0310a.dat

[2] http://solarscience.msfc.nasa.gov/greenwch.shtml

[3] http://sidc.oma.be/DATA/dayssn_import.dat

The group sunspot numbers extend back to 1610 and consist of monthly values. The data were obtained from NOAA National Geophysical Data Center.[4]

3 Correlation as a function of averaging window

In studies using solar-terrestrial data some temporal averaging is often applied, like monthly averages, yearly averages, or 13-month running averages. The average is introduced to suppress noise, or details that are not relevant, and to increase the signal strength at longer time scales thus acting as a low-pass filter. However, the average is also affected by higher frequency components. In the next section we will use a more powerful filtering method.

After temporally averaging the data the linear correlation between two time series may be computed, but it is often forgotten, especially for running averages, that the averaging introduces artificial correlation. To address this problem a confidence interval is computed taking into account the number of independent observations (Quenouille, 1952; Wilks, 1995; von Storch and Zwiers, 1999). Using the method by Wilks (1995) we compute the linear correlation between R_z and TSI based on 1 to 365 day running averages. The result is shown in Figure 1 (solid curve) together with the 95% confidence interval (dashed curve). The linear correlation is 0.35 for daily data, and then increases when the averaging window increases. However, the number of independent observations simultaneously decrease making the confidence interval larger. It can be seen from the figure that the lower limit is consistently above zero which may be interpreted as that R_z and TSI are correlated at the 95% confidence level.

In Figure 2 we show the 365-day averages of TSI (blue circles) together with reconstructed ($\overline{\mathrm{TSI}}$, red pluses), where the reconstructed TSI is based on the linear model

$$\overline{\mathrm{TSI}} = a_0 + a_1 Rz. \tag{3}$$

The constants are found using a least squares fit ($a_0 = 1365.4$ W/m^2, $a_1 = 6.99 \cdot 10^{-3}$ W/(m^2·SSN)). The linear correlation between the two data sets is 0.97 which is visually confirmed from Figure 2, especially as we have lines connecting the dots that helps the eye to linearly interpolate between dots. There are 24 data points in the two series, but the number of independent observations is much smaller: we estimate it to be between 1.3 to 4.5 were the smaller number comes from Quenouille (1952) and the larger number from Wilks (1995). To be able to compute a confidence interval we must have at least 4 independent observations. Therefore, assuming 4 independent observations we estimate that the linear correlation lies in the interval $[0.11, 0.97]$ at the 95% confidence level. But, at the 97% level the zero correlation is inside the confidence interval ($[-0.10, 1.00]$).

We will now study the correlation again but on a scale-by-scale basis using wavelet transformations.

[4] ftp://ftp.ngdc.noaa.gov/STP/SOLAR_DATA/-SUNSPOT_NUMBERS/GROUP_SUNSPOT_NUMBERS/

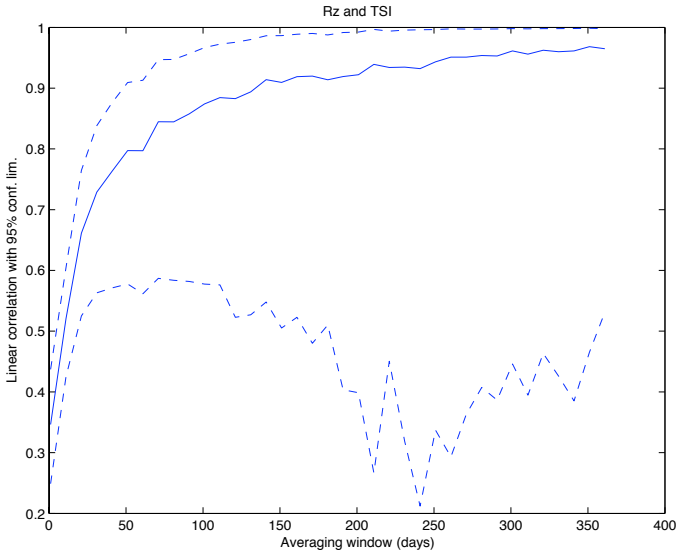

Fig. 1. The linear correlation between R_z and TSI for 1 to 365 day averages. The solid curve is the correlation and the dashed curves are the upper and lower limits of the 95% confidence interval.

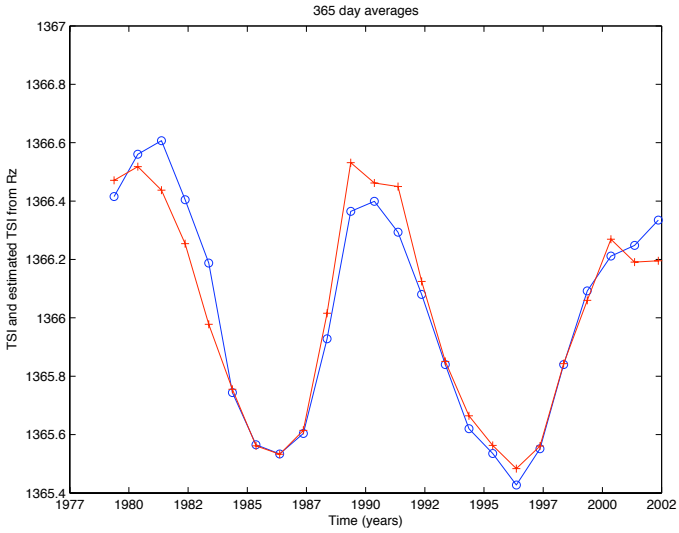

Fig. 2. The 365-day averages of TSI (blue circles) and TSI reconstructed from R_z (red pluses) using a least-squares-fit on the 365-day averages.

4 Wavelet analysis

4.1 Properties

In wavelet analysis a signal is transformed into a set of coefficients that are localised in time and frequency (or scale). The transform relies on a base function with the following properties: It must integrate to zero and the integrated power must be bounded. These two requirements mean that the base function is wavelike and that it has finite extent. This can be compared with the Fourier transform where the base function is the sine function. The sine function integrates to zero but has unlimited integrated power. The wavelet analysis can be performed using either the continuous wavelet transform (CWT) or the discrete wavelet transform (DWT). We will use a DWT called maximal overlap DWT (MODWT) (Percival and Walden, 2002; Cornish et al., 2003). The main advantage of the MODWT is that the transform is invariant under temporal shifts, while the DWT is not.

The MODWT transforms a signal $x(t)$ into a set of wavelet coefficients ($W_j(t)$) and a scaling coefficient ($V_J(t)$)

$$x(t) \rightarrow \{W_1(t), \ldots, W_J(t), V_J(t)\} \tag{4}$$

where the level j goes from 1 to J. The magnitudes of the coefficients reflect the variability of the signal at different levels. The coefficients may then be used in a multi resolution analysis (MRA). The MRA of a signal x is written as

$$x(t) = \sum_{j=1}^{J} D_j(t) + A_J(t) \tag{5}$$

where $D_j(t)$ is the detail at level j and time t, and $A_J(t)$ is the approximation at time t. The highest analysed level is J. Each level captures the variation of x at a scale (we define $\text{scale} = 1/\text{frequency}$) that increases with j. The detail at level j is a bandpass filtered signal in the approximate frequency range

$$f_j = [2^{-j-1}, 2^{-j}]. \tag{6}$$

The approximation A_J is a low-pass filtered signal with cut-off frequency at $1/2^{J+1}$. Thus, with a temporal resolution of days the detail at level 1 (D_1) captures variations in the range $[2, 4]$ days, while A_1 captures variations at periodicities longer than 4 days. In this work we wish to study variability with periods longer than the 11-year cycle which means that we should have $2^{J+1} > 11 \cdot 365$ days, which gives $J > 10.97$. To get well beyond the 11-year cycle we set $J = 12$.

As the wavelet filter has a width, in time domain, that increases with increasing level there is an upper limit of the maximum level J that can be used. An estimate of J is to have (Percival and Walden, 2002)

$$J < \log_2\left(\frac{N}{L-1} + 1\right). \tag{7}$$

where L is the width of the wavelet base filter and N is the length of the time series. A narrow filter (small L) is well localised in time but not in frequency, while the opposite holds for a wide filter. In this study the TSI time series is the shortest with $N = 9085$ days. Using Eq. 7 and with $J = 12$ we get $L < 2.2$. Therefore we choose a wavelet called the Haar wavelet which has $L = 2$.

The width of the filter at level j is

$$L_j = (2^j - 1)(L - 1) + 1 \tag{8}$$

which means that L_j wavelet coefficients will be influenced by edge effects and should not be used in any further analysis. Using the Haar wavelet ($L = 2$) we get $L_j = 2^j$. However,

the edge effects have an even greater influence on the details due to the MODWT algorithm. The number of affected points in the detail and approximation at level j is $2L_j$. Thus, if we study the wavelet coefficients we will have $9085-L_J = 9085 - 2^{12} = 4989$ data values left, while the details or approximation will have $9085 - 2L_J = 9085 - 2 \cdot 2^{12} = 893$ useful values.

4.2 Scale based correlation

Using the wavelet transform we have decomposed the signal $x(t)$, where x is the TSI series, into the thirteen series

$$x(t) \rightarrow \{W_1^{(x)}(t), \ldots, W_{12}^{(x)}(t), V_{12}^{(x)}(t)\} \quad (9)$$

where the superscript (x) indicates series x. Similarly, another series y, where y is one of R_z, R_g, or SSA, is decomposed into $\{W_1^{(y)}(t), \ldots, W_{12}^{(y)}(t), V_{12}^{(y)}(t)\}$. Actually, for R_g we use monthly values and therefore the maximum level becomes J=7 as explained at the end of this section.

We may now compute the correlation scale-by-scale as

$$C_j = \mathrm{corr}(W_j^{(x)}, W_j^{(y)}) \quad (10)$$

where corr is the linear correlation. We also compute the confidence interval of the correlation and in estimating the number of independent observations we compensate for the auto-correlation in the time series (Quenouille, 1952; Wilks, 1995). The correlation between SSA and TSI is shown in Figure 3. The width of each box shows the range of periods that is captured at each level, while the height of the box shows the 95% confidence interval. The figure reveals a complex relation between SSA and TSI as a function of scale. It is seen that on scales of 8 days or less the correlation is weak. Then, with increasing scale SSA and TSI become anti-correlated reaching maximum strength around 32 to 128 days with a correlation of -0.84. The magnitude of the correlation then decreases passing through zero around 1.4 to 2.8 years. Finally, the correlation increases coming very close to 1 around the 11-year period. It is worth mentioning that the correlation at level 12 is based on $N - L_{12} = 9085 - 4096 = 4989$ data points. However, the two series are very smooth and the number of independent observations is estimated to be only 5.9! But even with this small number of independent observations the correlation is so strong making the confidence interval narrow. At scales above 22 years we compute the correlation using the scaling coefficients $V_{12}^{(x)}(t)$ and $V_{12}^{(y)}(t)$. The correlation is somewhat weaker than for W_{12} (Figure 3) but the number of independent observations drops below 4 making it unreliable to estimate the confidence interval. Using $N_e = 4$ the confidence interval is so large that it contains the zero correlation.

We repeat the same analysis but now using R_z and the result is shown in Figure 4. The behaviour is similar to that of SSA but with the main difference in that the anti-correlation at intermediate scales is weaker reaching a strongest correlation of -0.47. The transition from negative to positive correlation is again around 1.4 to 2.8 years and the maximum correlation is also close to 1.

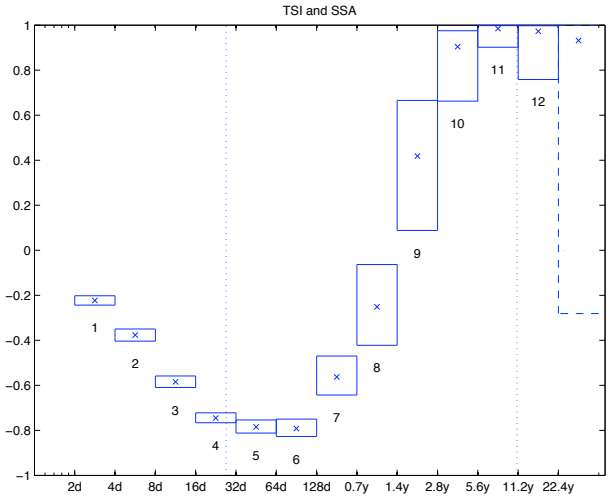

Fig. 3. Linear correlation between SSA and TSI for levels $j = 1, \ldots, 12$. The width of each box shows the approximate wavelength band that is captured. The height of the box shows the 95% confidence interval. The linear correlation is computed on both the wavelet coefficients (solid boxes) and the scaling coefficient (open dashed box). The two vertical dotted lines are at 27 days and 11 years, respectively.

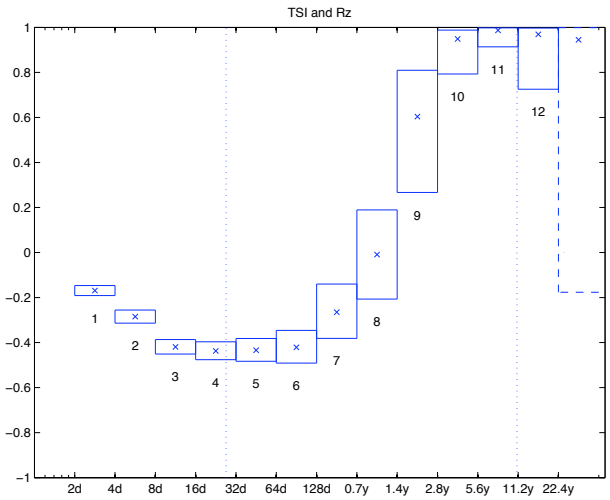

Fig. 4. Linear correlation between R_z and TSI for levels $j = 1, \ldots, 12$. The width of each box shows the approximate wavelength band that is captured. The height of the box shows the 95% confidence interval. The linear correlation is computed on both the wavelet coefficients (solid boxes) and the scaling coefficient (open dashed box). The two vertical dotted lines are at 27 days and 11 years, respectively.

Finally, we correlate the group sunspot number R_g with TSI. As the R_g time series consists of monthly data we first compute monthly averages of TSI. The result is shown in Figure 5. Level 1 now corresponds to the interval 2 to 4 months which is close to level 6 for the SSA and R_z analyses. It is seen that R_g is uncorrelated with TSI below 1.3 years, then the correlation becomes strongly positive.

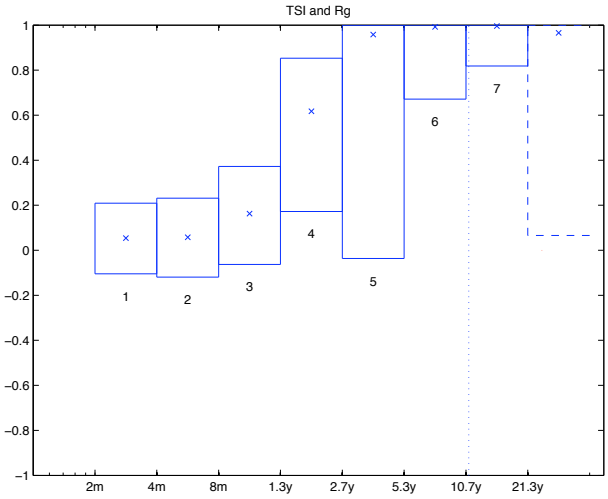

Fig. 5. Linear correlation between R_g and TSI for levels $j = 1, \ldots, 12$. The width of each box shows the approximate wavelength band that is captured. The height of the box shows the 95% confidence interval. The linear correlation is computed on both the wavelet coefficients (solid boxes) and the scaling coefficient (open dashed box). The vertical dotted line is at 11 years.

The confidence interval is, however, much larger because the temporal overlap for the R_g and TSI series is shorter compared to both R_z and SSA and thus the number of independent observations is smaller.

We now turn to discussions of these results and the reconstruction of TSI.

5 Reconstruction of TSI

The physics behind the variation in TSI can be explained by two competing effects: dimming by the appearance of dark sunspots and the brightening from faculae. Both effects can be related to the surface magnetic fields (Krivova et al., 2003). The brightening and dimming components of TSI can be expressed by the equation (Lockwood, 2005)

$$\mathrm{TSI} = Q_0 + f_b - \mathrm{PSI} \tag{11}$$

where Q_0 is the quiet level free from magnetic features, f_b is the brightness contribution from faculae, and PSI is the photometric sunspot index (Fröhlich et al., 1994) representing the darkening due to sunspots. There is a strong linear relationship between PSI and SSA (Lockwood, 2005). However, we also know that TSI and SSA are positively correlated (Fig. 1) which at first glance contradicts Eq. 11. But, as the brightening (f_b) from faculae appear in active regions and thus are to a great extent associated with sunspot groups there will be a statistical positive correlation between f_b and PSI. Therefore, it is not trivial to statistically separate the brightening and dimming effects when the only available series is a single series like SSA, R_z, or R_g. But as the temporal evolution of sunspots and bright regions are different we should expect to be able to separate the dimming and brightening by looking at different frequency components of the time series. This was basically the approach by Solanki and Fligge (1999) who divided R_z into a slow and a fast component.

We now study the reconstruction of monthly TSI based on the wavelet details and approximation using monthly average data. It should be noted that Figures 3 and 4 are based on an analysis using daily data. But level 6 (64 to 128 days) using daily data corresponds approximately to level 1 (2 to 4 months) using the monthly data. Thus, to compare Figure 5 to Figures 3 and 4 we simply add 5 to the level index.

5.1 One-component model

It is seen in Figure 5 that TSI and R_g are uncorrelated for levels 1 to 3 and that the correlation is positive for levels 4 and up. However, although the correlation at level 5 is above 0.9 the confidence interval is very large including the zero correlation. But it still seems reasonable to low-pass filter the series so that at least levels 1 to 3 are excluded. The cut-off could thus be set at 1.3 years but we will instead place it at 2.7 years. We do this because we want to as much as possible remove the anti-correlated component from the filtered signal, and because there is a small amount of power leaking between the levels we do not use D_4. Therefore we use the approximation A_4 at level $J = 4$. The linear fit is made according to

$$y = a_0 + a_1 x + \epsilon = \hat{y} + \epsilon \tag{12}$$

where $x = A_4(\mathrm{SSA}, R_z, \text{or } R_g)$, $y = \mathrm{TSI}$, and ϵ is the error. Minimising the squared error gives the constants shown in Table 1. As the numerical values of SSA and R_z are different we can not directly compare the values of a_1, instead we also compute the coefficient a_1 times the standard deviation of x (σ_x). It is seen that $a_1\sigma_x$ is very similar in value for the three reconstructions. The reconstructed series are shown in Figure 6 for the extent of the TSI series. In Figure 7 the reconstructed TSI is shown from 1600.

Table 1. The table shows the constants in Eq. 12 found from minimising the summed squared errors. The standard deviation of x times a_1 ($a_1\sigma_x$) and the correlation between reconstructed and observed TSI (C) are also shown.

Index	a_0	a_1	$a_1\sigma_x$	C
SSA	1365.47	$0.44 \cdot 10^{-3}$	0.354	0.83
R_z	1365.41	$7.33 \cdot 10^{-3}$	0.354	0.83
R_g	1365.42	$7.11 \cdot 10^{-3}$	0.345	0.81

5.2 Two-component model

As we saw from Figures 3 and 4 both SSA and R_z show an anti-correlation at scales shorter that about 1 year. We may therefore separate the low- and high-frequency components

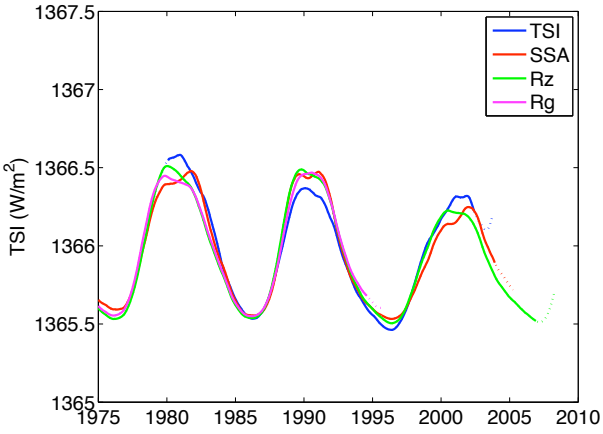

Fig. 6. The figure shows the filtered monthly TSI at level 4 (blue) together with the reconstructed TSI using Eq. 12 based on SSA (red), R_z (green), and R_g(magenta), respectively. The dotted parts of the curves indicate data affected by edge effects.

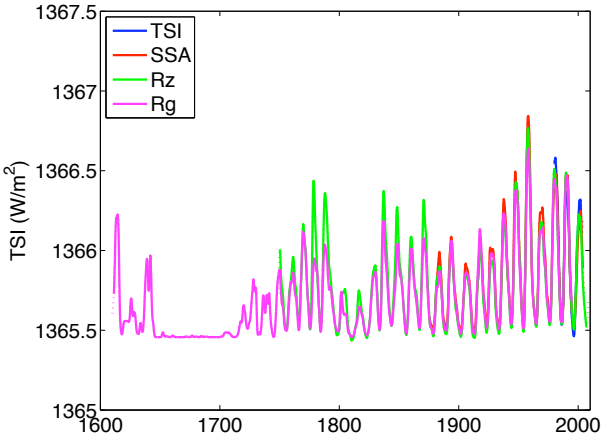

Fig. 7. The figure shows the same data as Figure 6 but extending back to 1610.

for the reconstruction. We use again a cut-off at level $J = 4$ and the equations now become

$$x_1 = A_4 \tag{13}$$

$$x_2 = \sum_{j=1}^{4} D_j \tag{14}$$

$$y = b_0 + b_1 x_1 + b_2 x_2 + \epsilon = \hat{y} + \epsilon \tag{15}$$

After minimising the summed squared errors we get the result shown in Table 2. We see that the constant terms (a_0 and b_0, respectively) are very similar between the two models. The slow term coefficient does, however, show an increase of about 7% when SSA is used ($b_1/a_1 \approx 1.07$). This is an effect of that the fast component (b_2) is now modelled separately. There is a similar effect for R_z although weaker (4%) due to the less accurate modelling of the fast component. Finally, R_g shows basically no change in the slow component coefficient. We also see that the variability of the fast component $b_2\sigma_{x2} = -0.157$ W/m^2 using SSA is twice as large

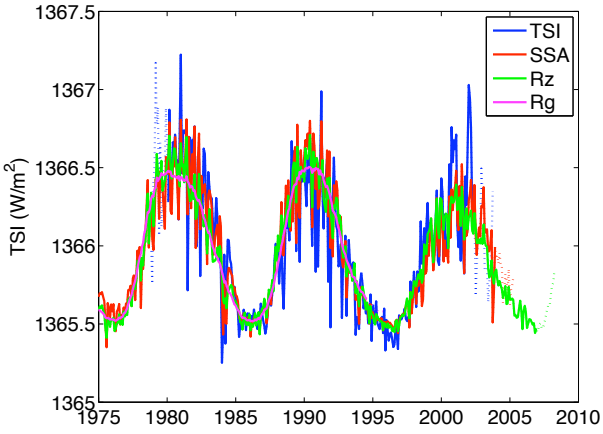

Fig. 8. The figure shows the observed monthly TSI (blue) together with the reconstructed TSI using Eq. 15 based on SSA (red), R_z (green), and R_g(magenta), respectively. The dotted parts of the curves indicate data affected by edge effects.

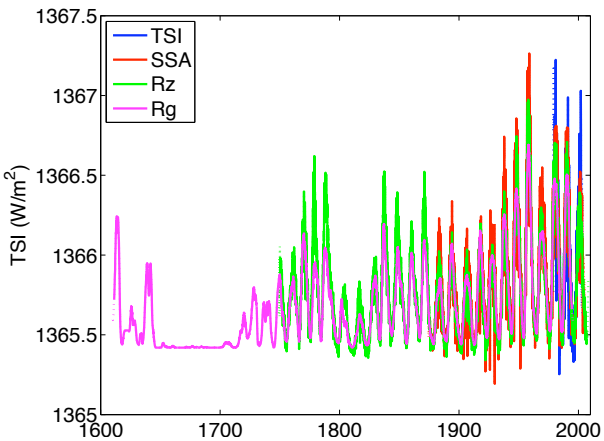

Fig. 9. The figure shows the same data as Figure 8 but extending back to 1610.

compared to when R_z is used. The variability of the fast component using R_g is negligible. The reconstructed TSI is shown in Figures 8 and 9.

6 Discussion and conclusions

In this work we have analysed time series of the total solar irradiance (TSI), the sunpot area (SSA), the sunspot number (R_z), and the group sunspot number (R_g) in the context of TSI reconstruction. There are two competing effects leading to the variability of TSI, namely darkening due to sunspots and brightening due to faculae (Lockwood, 2005). When detailed solar magnetic field observations exist the TSI variability can be successfully modelled from the magnetic features (Krivova et al., 2003). For reconstructions further back in time indices like SSA, R_z, and R_g are used instead. As sunspots and faculae evolve on different time scales we applied a wavelet analysis, called the maximal overlap discrete

Table 2. The table shows the constants in Eq. 15 found from minimising the summed squared errors. The standard deviation of x_1 times a_1 ($a_1\sigma_{x1}$), and x_2 times a_2 ($a_2\sigma_{x_2}$) and the correlation between reconstructed and observed TSI (C) are also shown.

Index	b_0	b_1	b_2	$b_1\sigma_{x1}$	$b_2\sigma_{x2}$	C
SSA	1365.44	0.47 $\cdot 10^{-3}$	-0.34 $\cdot 10^{-3}$	0.374	-0.157	0.91
R_z	1365.38	7.61 $\cdot 10^{-3}$	-4.87 $\cdot 10^{-3}$	0.368	-0.085	0.86
R_g	1365.42	7.15 $\cdot 10^{-3}$	-0.68 $\cdot 10^{-3}$	0.347	-0.011	0.82

wavelet transform (MODWT) (Percival and Walden, 2002), and studied the correlation as function of temporal scale. The correlation analysis based on the MODWT showed a complex relationship over different scales between TSI and the solar indices (Fig. 3, 4, and 5).

Studying SSA first we see that at small scales (days) the correlation is weak, then at intermediate scales (months) there is a strong anti-correlation, and finally at solar cycle scales there is a strong positive correlation. The strongest anti-correlation is reached at level 6 corresponding to periods of 64 to 128 days. The correlation is -0.84 which means that 71% of the variance in TSI can be modelled by SSA at that scale. The strong anti-correlation between SSA and TSI may be interpreted as the sunspot dimming effect being dominant in SSA around these time scales. Then, at levels 11 and 12, which captures the 11-year variation, the correlation is above 0.93. On these temporal scales large scale magnetic features dominate that may be associated to features like faculae and that are statistically linked to SSA.

A similar relation is seen between R_z and TSI (Fig. 4). The small scale anti-correlation and large scale positive correlation also explains the steep increase in correlation seen in Figure 1: as the averaging window is increased the small scale anti-correlation is removed leaving only the long scale solar cycle variation. A notable difference between R_z and SSA is that the anti-correlation at intermediate scales is much weaker. Thus, the dimming due to sunspots is much weaker represented in the sunspot number time series. This can be explained from how R_z is constructed. R_z contains two terms: the number of sunspots, and the number of sunspot groups. We expect that first term should be associated with the dimming while the second term should be associated with the brightening. But as the groups are weighted by a factor of 10 over the sunspots this means that the dimming effect will be weaker in R_z than in SSA.

Finally, R_g shows no correlation at intermadiate scales (Fig. 5) and following the arguments about R_z this may be explained by that individual sunspots have not been used in deriving R_g only sunspot groups have been used.

Based on the results above we then reconstruct TSI by separating the short term from the long term variation. At first a linear model using only the long term variation were used (Eq. 12) which shows that any of the three indices SSA, R_z, and R_g may be used (Tab. 1). The three reconstructed TSI (Fig. 7) are in reasonable agreement back to about 1880, but going further back in time the differences become larger (only R_z and R_g available) due to differences between the R_z and R_g series. It may be argued that R_g is more accurate than R_z because R_g is constructed from a database containing more observations (Hoyt and Schatten, 1998).

When we also include the short term variations (Eq. 15) the correlation between the reconstructed and observed TSI increases from 0.83 to 0.91 (Tab. 2) using SSA. We also see again that the dimming effect is more poorly captured in R_z as the reconstructed variability is only half of the value from SSA. The increase in correlation is also smaller (from 0.83 to 0.86). Finally, there is no improvement, as expected, when the high frequency component is included using R_g.

Now we return to Figure 6. We see that the observed maximum TSI is about 0.07 W/m^2 higher than any of the reconstructions around 1980. In the next maximum, around 1990, the observed TSI is instead about 0.14 W/m^2 lower, and around the 2001-maximum the observed TSI is again higher by about 0.05 W/m^2. These are actually quite large errors considering that the variation over a cycle is about 1 W/m^2. Thus, from this relatively short time series we see that the trend in observed TSI is completely different from the trends in the reconstructions. This is also in agreement with the finding that the TSI series has properties that are fundamentally different from all other series of solar indices (Dudok de Wit et al., 2008) suggesting that any reconstruction of TSI might be difficult. This is also indicated by the zero correlation lies within the 95% confidence interval of the approximation at level 12 (Fig. 3). Thus, the reasonably high correlation that we reach (up to 0.91) is dominated by the 11-year variation and what the relations between the solar indices and TSI are on time scales above 11 years is difficult to conclude due to the (relatively) short extent of the TSI series.

Acknowledgements. This work has been partly funded by the ESA/ESTEC Contract "ESA ITT AO/1-4618/NL/AR".

References

Boberg, F. and Lundstedt, H.: Solar wind variations related to fluctuations of the North Atlantic Oscillation, Geophysical Research Letters, 29, 2002.

Bochníček, J. and Hejda, P.: The winter NAO pattern changes in association with solar and geomagnetic activity, Journal of Atmospheric and Solar-Terrestrial Physics, 67, 17–32, 2005.

Cornish, C. R., Percival, D. B., and Bretherton, C. S.: The WMTSA Wavelet Toolkit for Data Analysis in the Geosciences, Eos Trans. AGU, 84, fall Meet. Suppl., Abstract NG11A-0173, 2003.

Dudok de Wit, T., Kretzschmar, M., Lilensten, J., Amblard, P. O., Moussaoui, S., Aboudarham, J., and Auchère, F.: Can the Total Solar Irradiance be reconstructed from solar activity proxies?, in Solar Variability, Earth's Climate and the Space Environment, June 1 – 6, 2008, Montana State University, Bozeman, USA, 2008.

Fröhlich, C.: Observations of irradiance variations, Space Science Reviews, 94, 15–24, 2000.

Fröhlich, C. and Lean, J.: The Sun's total irradiance: Cycles, trends and related climate change uncertainties since 1976, Geophysical Research Letters, 25, 4377–4380, 1998.

Fröhlich, C., Pap, J. M., and Hudson, H. S.: Improvements of the photometric sunspot index and changes of the disk-integrated sunspot contrast with time, Solar Physics, 152, 111–118, 1994.

Haigh, J. D.: The Sun and the Earth's Climate, Living Reviews in Solar Physics, 4, 1–64, http://www.livingreviews.org/lrsp-2007-2, 2007.

Hoyt, D. V. and Schatten, K. H.: Group sunspot numbers: A new solar activity reconstruction, Solar Physics, 181, 491–512, 1998.

Krivova, N. A., Solanki, S. K., Fligge, M., and Unruh, Y. C.: Reconstruction of solar irradiance variations in cycle 23: Is solar surface magnetism the cause?, Astronomy and Aastrophysics, 399, L1–L4, 2003.

Krivova, N. A., Balmaceda, L., and Solanki, S. K.: Reconstruction of solar total irradiance since 1700 from the surface magnetic flux, Astron. Astrophys., 467, 335–346, 2007.

Lean, J., Beer, J., and Bradley, R.: Reconstruction of solar irradiance since 1610: Implications for climatre change, Geophysical Research Letters, 22, 3195–3198, 1995.

Lockwood, M.: Solar outputs, their variations and their effects on Earth, pp. 109–306, Saas-Fee Aadvanced Course 34 2004, Springer-Verlag Berlin Heidelberg, 2005.

Percival, D. B. and Walden, A. T.: Wavelet methods for time series analysis, Cambridge University Press, 2002.

Quenouille, M. H.: Assoicated measurements, Butterworths Scientific Publications, 1952.

Sofia, S. and Li, L. H.: Solar variability and climate, Journal of Gephysical Research, 106, 12,969–12,974, 2001.

Solanki, S. K. and Fligge, M.: A reconstruction of total solar irradiance since 1700, Geophysical Research Letters, 26, 2465–2468, 1999.

Svensmark, H. and Friis-Christensen, E.: Variation of cosmic ray flux and global cloud coverage - a missing link in solar-climate relationships, Journal of Atmospheric and Solar-Terrestrial Physics, 59, 1225–1232, 1997.

Tapping, K. F., Boteler, D., Charbonneau, P., Crouch, A., Manson, A., and Paquette, H.: Solar magnetic activity and total irradiance since the Maunder minimum, Solar Physics, 246, 309–326, 2007.

Tinsley, B. A.: Influence of solar wind on the global electric circuit, and inferred effects on cloud microphysics, temperature, and dynamics in the troposphere, Space Science Reviews, 94, 231–258, 2000.

von Storch, H. and Zwiers, F. W.: Statistical analysis in climate research, Cambridge University Press, 1999.

Waldmeier, M.: The sunspot-activity in the years 1610-1960, Schulthess & Co. AG, Zürich, 1961.

Wilks, D. S.: Statistical Methods in the Atmospheric Sciences: an Introduction, vol. 59 of *International Geophysics Series*, Academic Press, 1995.

Paper E

Multiresolution analysis of
synoptic solar magnetic fields

Manuscript prepared for Ann. Geophys.
with version 1.3 of the LaTeX class copernicus.cls.
Date: 21 October 2008

Multiresolution analysis of synoptic solar magnetic fields

M. Wik[1], **H. Lundstedt**[1], **and P. Wintoft**[1]

[1]Swedish Institute of Space Physics, Lund, Sweden

Abstract. Solar synoptic maps of the photospheric magnetic field provide an important visualization of the global evolution of the Sun over time. In this study we have performed a multiresolution analysis (MRA) of a series of photospheric synoptic magnetograms. Magnetograms from Wilcox Solar Observatory (WSO), at Stanford University, were used. WSO data enabled a study of cycles 21, 22 and 23. Multiresolution analysis reveals a complex picture of the solar magnetic activity. Using MRA we decomposed the 2-D data into wavelet approximations and details. For each approximation and detail we see regular patterns as standing waves on different latitude bands. These waves are occasionally broken by asymmetries between solar northern and southern hemispheres. This method can also be used as an alternative way to derive the longitudinally averaged solar magnetic field.

1 Introduction

Solar magnetic activity is the driver of space weather. Space weather can have a severe effect on technological systems ((Lundstedt, 2005a)). Not only space-borne systems are affected, but terrestrial systems such as electrical power distribution grids and terrestrial communications as well.

To mitigate these effects, predictions of solar activity play an important role. In Lundstedt (2001) predictions of solar activity based on Artificial Intelligence (Fu (1994)) methods is reviewed. A new approach of exploring, understanding and predicting solar activity was introduced in (Lundstedt, 2006b). It is based on newly developed wavelet methods and physics-based neural networks. The developed wavelet methods were applied to short-term and mid-term solar activity indicators (Lundstedt, 2005b).

Wavelet techniques is today a common method of analysing solar-terrestrial data. Good introductions to the use of wavelet transforms are given by Daubechies (1992), Torrence and Compo (1998) and Addison (2002). Wavelet analysis is a powerful tool both to find the dominant mode of variation and also to study how it varies with time, by decomposing a non-linear time series into time-frequency space. Long-term solar magnetic activity were studied by wavelet methods in (Lundstedt, 2006c).

Many have modeled the distribution and changes of magnetic flux as seen in the longitudinally averaged synoptic maps. Either through the description of the photospheric flux dispersal by a diffusion equation (Wang et al., (2000)) or also including the three-dimensionality of the magnetic and velocity fields (Dikpati et al., (2006), Tobias et al., (1997), Tobias et al., (2005)). Harmonic analysis have also been performed (Stenflo (1988), Stenflo and Gudel (1988), Cadavid et al. (2005), Knaack and Stenflo (2005) and Knaack et al. (2005)). Another method used is spectral analysis together with autocorrelation (Gavryuseva, E., and Godoli, G., (2006)). In Obridko et al., (2006) they performed a wavelet analysis on longitudinelly averaged synoptic maps.

In solar dynamo theory, the induction equation gives the kinematics of the field

$$\frac{\partial \mathbf{B}}{\partial t} = \nabla \times (\mathbf{v} \times \mathbf{B}) + \eta \nabla^2 \mathbf{B} \tag{1}$$

and the dynamics of the field is given by the Lorenz force

$$\mathbf{j} \times \mathbf{B} = \mu_0^{-1}(-\nabla(\frac{1}{2}|\mathbf{B}|^2) + (\mathbf{B} \cdot \nabla)\mathbf{B}). \tag{2}$$

E. Parker suggested already in 1955 (Parker (1979)) that the magnetic fields and velocity exist in two separate scales l and $L \gg l$. In large-scale or mean field dynamos we write $\mathbf{B} =< \mathbf{B} > + \mathbf{b}$ and for the velocity $\mathbf{V} =< \mathbf{V} > + \mathbf{v}$. $\mathbf{B}$ is devided into a poloidal and a toroidal part. The velocity $\mathbf{V}$ is divided into a meridional flow and a differential rotation part. However, also small-scale dynamos (Cattaneo and Hughes (2001)) operate and likely also together with large

Correspondence to: Magnus Wik (magnus@lund.irf.se)

scale dynamos. The dynamo picture is thus dependent on both the spatial and time resolution. A multiresolution analysis gives us a possibility to study the synoptic solar magnetic fields at several resolutions at the same time. This should be compared with the typical magnetic butterfly diagram.

In section 2 we descibe the data. This is followed by a multiresolution analysis of synoptic maps in section 3. Finally, in sections 4 and 5, we discuss and compare the results.

2 Data - Synoptic maps

Many indicators exist of solar magnetic activity (Lundstedt (2006b)), e.g. the sunspot number, F10.7 solar radio flux and C^{14} proxies. However they are one-dimensional indicators. Synoptic maps give us a method to visualize 2D solar magnetic activity, a much richer picture of the solar magnetic activity. In this study we use photospheric magnetic field synoptic charts from WSO.

We used synoptic charts calculated from the line-of-sight photospheric magnetic fields, of 3 arcmin resolution, observed at Wilcox Solar Observatory (WSO) (Scherrer et al., (1977), Hoeksema (1984), Hoeksema (1985)) at Stanford University. The noise level, for the magnetograph, is about 10 μT. The WSO data cover three cycles from 1976 (CR 1642) up to 2006 (CR 2050). The data for each Carrington rotation consists of 72x30 values (longitude and latitude) and was first corrected for missing and unusually high values. The resolution, in both longitude and latitude, is 5^0. The regions from 70^0 to the poles are not resolved. The time between successive data points is therefore about 27.2753/72=0.4 days.

For each Carrington rotation we first calculated the average magnetic flux density for each latitude. This results in a 30x409 matrix (latitude x carrington rotations). The result is the typical "magnetic butterfly diagram" as seen in Fig. 1. In the next section we will describe a different approach, using wavelet analysis, to derive the butterfly diagram. For the wavelet analysis we use a series of synoptic maps. This results in a 30x29448 matrix (409·72=29448 values).

3 Multiresolution analysis

A moving average filter averages the data and removes the high frequency components present in the signal. Moving average filters are normally used as low pass filters. By calculating the average over a Carrington rotation we therefore filter the data. Since the average span 27.2753 days, we apply a low-pass filter, essentially removing periods in the data below a Carrington rotation. However, it is not strictly a low-pass filter since a moving average is not derived. For many data series, especially if the signal is close to stationary, Fourier analysis is useful when searching for the frequency content. However, if we also want to know the timing of an event, wavelet analysis is often more suitable. In this paper we use the method of multiresolution analysis (MRA).

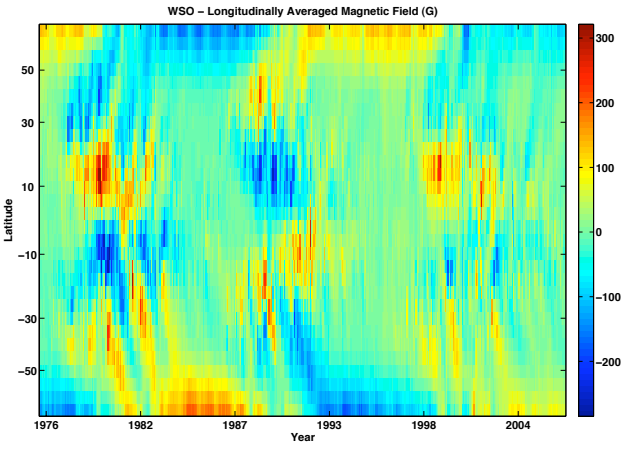

Fig. 1. shows the longitudinally averaged line of site magnetic fields (in μT) observed at WSO, Stanford. The data cover cycle 21, 22 and 23.

3.1 Properties

In MRA, the signal is decomposed into a principal (approximation or low pass) and a residual (detail or high pass) part. The approximations are the high scale (or low "frequency") part and the details are the low scale (or high "frequency") part. This process can then be applied again to both parts. The discrete wavelet transform coefficients, $C(j,k)$, are derived similar to the fourier transform but with a wavelet function instead.

The decomposition of a signal $s(t)$ is described mathematically by

$$s(t) = A_J(t) + \sum_{j \leq J} D_j(t) \tag{3}$$

where $s(t)$ is the sum of two signals: the approximation $A_J(t)$ (at resolution level J) and the detail $D_j(t)$ (at level j). The approximations are related to one another by

$$A_{J-1}(t) = A_J(t) + D_J(t) \tag{4}$$

$$D_j(t) = \sum_{k=Z} C(j,k)\psi_{j,k}(t) \tag{5}$$

where $C(j,k)$ is the wavelet coefficient and $\psi_{j,k}(t)$ the wavelet function.

The wavelet used in this study is a Daubechies of order six where $s(t)$ represents the solar magnetic flux density. The different scales are related to the so called pseudo-period which are listed in table 1. The pseudo-period is defined as the scale divided by the sampling period and center frequency of the wavelet. The purpose of the pseudo-period is

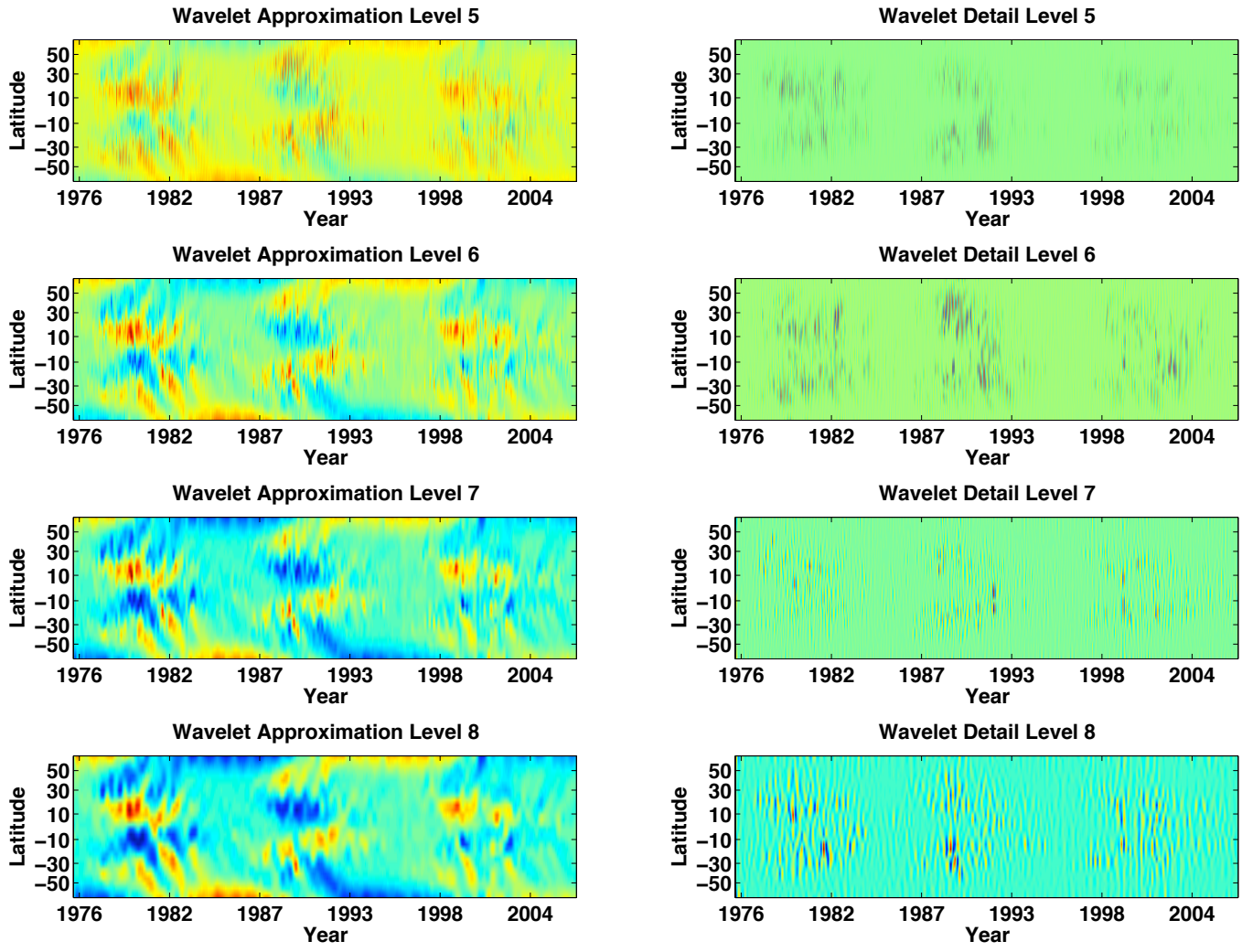

Fig. 2. MRA approximations and details for levels 5–8 (13 days to 0.3 years) of synoptic WSO magnetic fields.

to be able to relate to the Fourier period. From here on, for ease of use, we simply use period, but it is important to remember that the meaning are not exactly the same.

3.2 Results

MRA was carried out, for each latitude, for WSO synoptic maps. This reveals how the magnetic flux varies on different scales. The distribution of the magnetic field in time and latitude is shown in Figures 2 to 4. The synoptic maps of the approximations and details show less and less details going from level 5 (about a day) to level 14 (about 18 years).

The transport of flux to the poles are clearly seen in approximation levels 5 to 9. We also see a clear distribution of flux in two latitude bands: equator – 30 degrees and 30 degrees – 75 degrees. The first band basically shows the emergence of active regions moving towards the equator whereas in the second latitude band magnetic flux is transported to the

Table 1. The relationship between the level, scale and pseudo-period. The pseudo-period are listed in days and years.

Level	Scale	Period (days/years)
1	2	0.8 d
2	4	1.6 d
3	8	3.2 d
4	16	6.4 d
5	32	13 d
6	64	26 d
7	128	51 d
8	256	0.3 y
9	512	0.6 y
10	1024	1.1 y
11	2048	2.2 y
12	4096	4.5 y
13	8192	9 y
14	16384	18 y

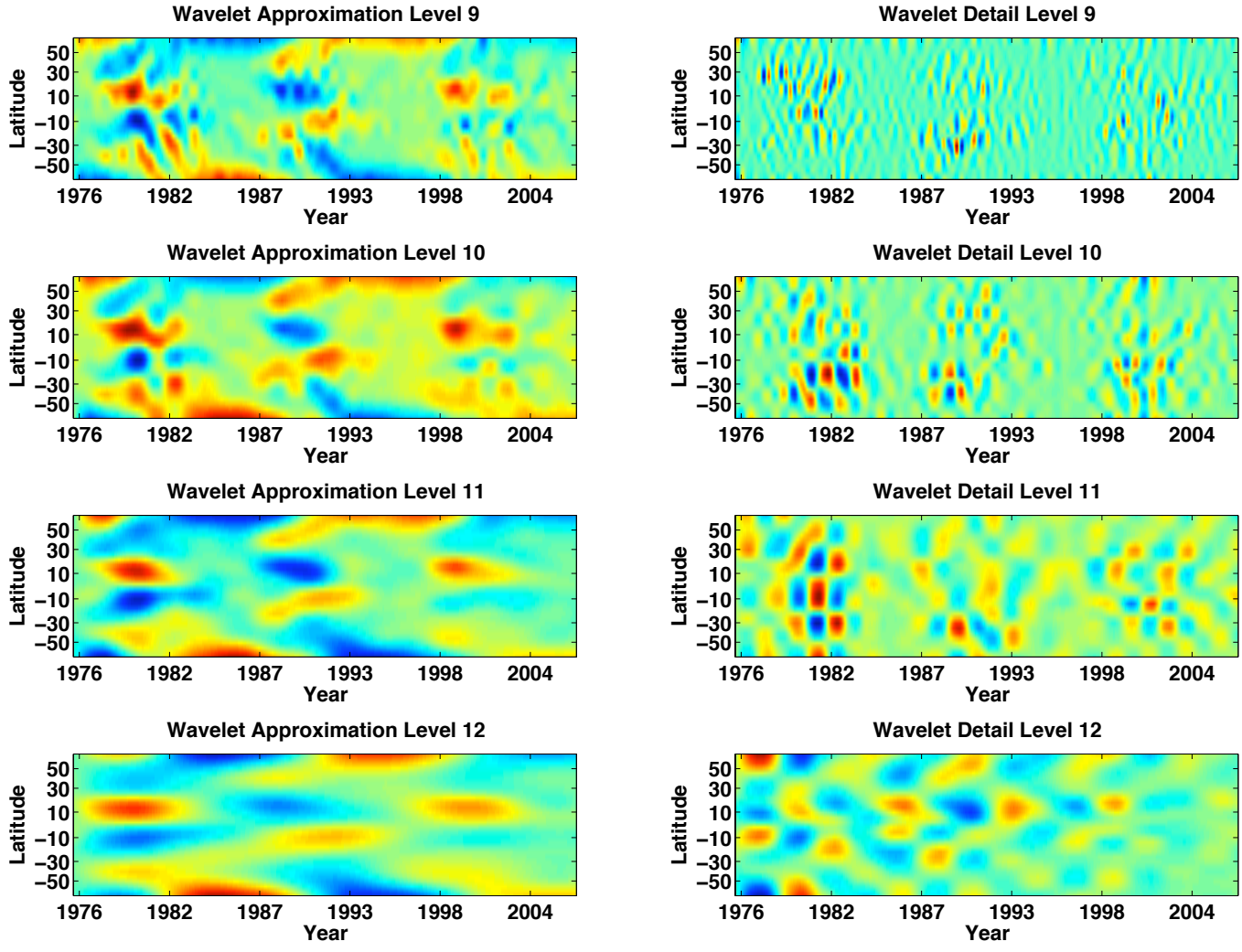

Fig. 3. MRA approximations and details for levels 9–12 (0.6 to 4.5 years) of synoptic WSO magnetic fields.

poles. In the second latitude band, moving from level 1 to higher levels is similar to observing the magnetic flux higher up in the solar atmosphere (dipole approximation). At level 13 (about 9 years) we observe a very regular pattern, almost like a standing wave. During cycle 23 the activity is higher for the northern hemisphere. This is seen e.g. in approximation level 11 and 13.

The detail maps show the difference between the resolutions. The first detail map shows a similarity to the Butterfly diagram, since it is produced by the short lived (couple of CR) active regions. The regular changes of polarity at the poles are also seen, as well as the decrease of the polar magnetic field since cycle 21 (Svalgaard et al., (2005)). It is also interesting to notice that even if we carried out the study at different resolutions of time, we again see coherent spatial structures. Large range of latitudes vary in phase.

The synoptic map of longitudinally averaged magnetic field, in Figure 1, is very similar to the wavelet approximation level 6. This level corresponds to a period of about 26 days which is close to the Carrington rotation period of 27.2753 days.

4 Discussion

The results depend on the solar resolution and type of wavelet. In this case, the lowest scale correspond to about 2.6 days.

We relate the different wavelet "bands" to especially two different motions on the Sun. the first is the meridional circulation that transports flux from the sunspot regions to the poles. The second band is perhaps related to the movement of sunspots to the equator, which in turn is related to the subsurface flow. These are also connected to the solar dynamo mechanism.

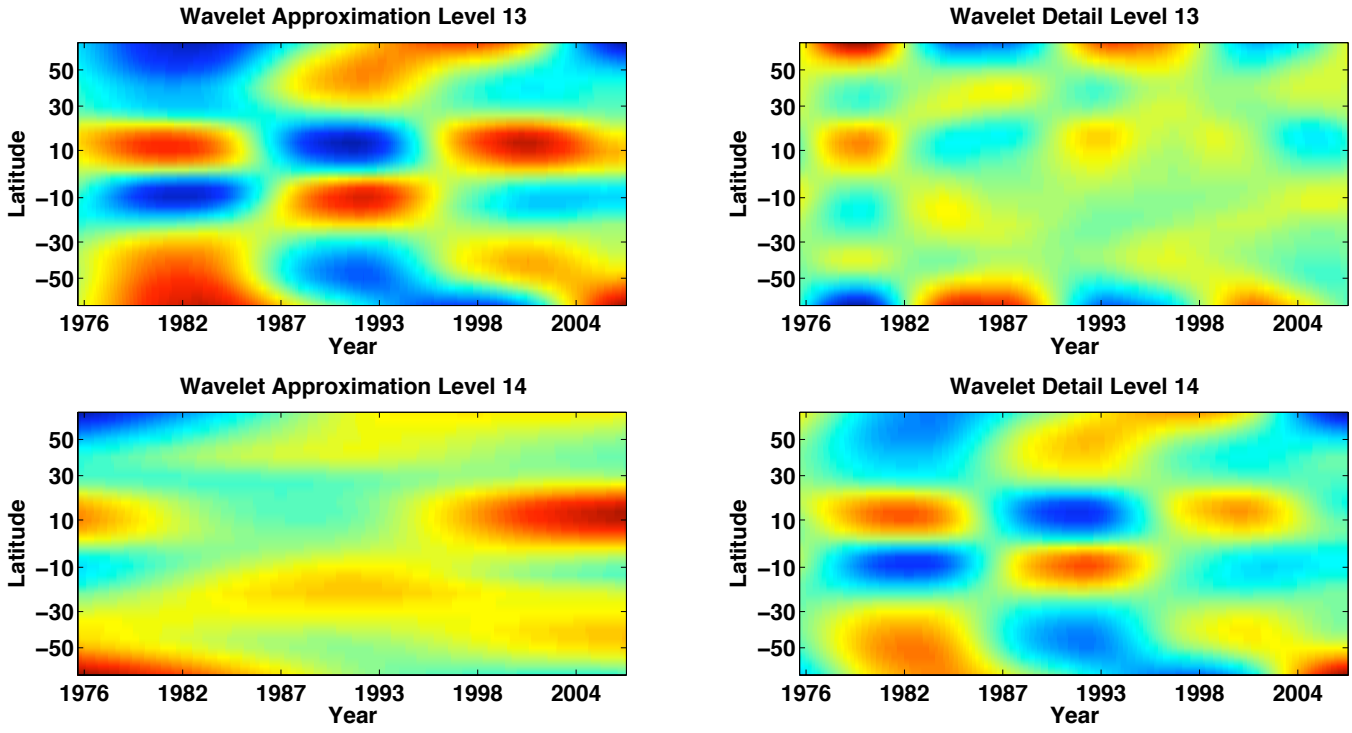

Fig. 4. MRA approximations and details for levels 13–14 (9 to 18 years) of synoptic WSO magnetic fields.

Note that there is nothing special about the Carrington rotation. A "solar-synchronous" spacecraft in orbit around the Sun would instead meausure the local development of flux in a fix location on the Sun.

It is also important to keep in mind that all the measurements are based on the Zeeman splitting only. Using the Hanle effect (Stenflo (2004)) gives us another picture of the solar magnetic activity: the turbulent magnetic fields.

The derived pseudo-periods are also dependent on the angular resolution. The WSO synoptic maps are produced from line-of-sight magnetograms. Next year the Solar Dynamics Observatory (SDO) will be launched. The Helioseismic and Magnetic Imager (HMI) investigation, onboard SDO, will provide 1 arc-second resolution full-disk vector-magnetic images of the longitudinal solar magnetic field at least every 90 seconds.

5 Conclusions

In this study we introduced a MRA study of synoptic solar magnetic fields derived from WSO. The 2-D picture enabled by synoptic maps is highly complex compared to the simple 1-D picture of the commonly used sunspot number. We also suggest to use this method for deriving the magnetic butterfly diagram compared to the standard procedure where averaged values are used. The reason for this is that with MRA we can study the magnetic flux on many timescales at the same time compared to the standard way which only shows time scales of about one Carrington period.

The WSO data gave us the opportunity to study the differences between the cycle 21, 22 and 23. It is striking how different the size of activity is between the both hemispheres. For the cycle 23 the activity, in the sunspot region, is almost absent for the southern hemisphere. In the northern hemisphere strong transport of fluxes occurs for cycle 21 and 22, but not for cycle 23.

In future studies we plan to do a more detailed MRA analysis, including subsurface flows and coronal magnetic fields as well. This will give us a 3-D picture of the solar magnetic activity. We also plan to examine trends and predictions of the solar magnetic activity on different scales. With the launch of SDO, and high resolution real-time synoptic maps, we will enter a new era in solar physics.

Acknowledgements. We are grateful to Wilcox Solar Observatory, Stanford, USA, for providing solar synoptic data.

References

Addison, P.: The Illustrated Wavelet Transform Handbook, Introductory Theory and Applications in Science, Engineering, Medicine and Finance, Institute of Physics Publishing, Bristol, 2002.

Beer, J., Tobias, S. and Weiss, N.: An Active Sun Throughout the Maunder Minimum, Solar Phys., 181, 237–249, 1998.

Boberg, F., Lundstedt, H., Hoeksema, J. T., Scherrer, P. H., and Lui, W.:Solar mean magnetic field variability: A wavelet approach to WSO and SOHO/MDI observations, J. Geophys. Res., Vol. 107, No A10, 15-1–15-7, 2002.

Cadavid, A. C., Lawrence, J. K., McDonald, D. P., Ruzmaikin, A., Independent global modes of solar magnetic field fluctuations, Solar Physics, 226, 359–376, 2005.

Cattaneo, F. and D.W. Hughes, Astron, Geophys., 42(3), 18, 2001.

Choudhuri, A. R., Chatterjee, P., and J. Jiang, Predicting solar cycle 24 with a solar dynamo model, PACS numbers: 96.60.-j, 96.50.Wx, 96.60.qd, 2007.

Daubechies, I.: Ten Lectures on Wavelets, CBMS-NSF regional conference series in applied mathematics, 1992

Dikpati, M., de Toma, G., and Gilman, P.A., Predicting the strength of solar cycle 24 using a flux-transport dynamo-based tool, Geophys., Res. Lett., 33, L05102, 2006.

Fu, L-M.: Neural Networks in Computer Intelligence, McGraw-Ill, Inc., 1994.

Gavryuseva, E., and Godoli, G., Structure and rotation of the large scale solar magnetic field observed at the Wilcox Solar Observatory, Phys. Chem. Earth, 31, 68–76, 2006.

Hathaway, D., Wilson, R. and J. Reichman, A synthesis of solar cycle prediction techniques, J. Geopys. Res. 104, 375–388, 1999.

Hoeksema, J. T., Structure and Evolution of the Large Scale Solar and Heliospheric Magnetic Fields, Ph. D. Thesis, CSSA Rep. 7, 1984.

Hoeksema, J. T., The solar magnetic field since 1976, John M. Wilcox Solar Observatory at Stanford, 1985.

Jensen, J. M., Lundstedt, H., Thompson, M. J., Pijpers, F. P., and Rajaguru, S. P.: Application of Local-Area Helioseismic Methods as Predicters of Space Weather, in Helio- and Asteroseismology: Towards a Golden Future, Ed. D. Danesy, Proc. SOHO 14/GONG+ 2004 Meeting,ESA SP-559, 497–500, 2004.

Knaack, R., Stenflo, J. O., Spherical harmonic decomposition of solar magnetic fields, Astron. Astrophys., 438, 349–363, 2005.

Knaack, R., Stenflo, J. O., and Berdyugina, S. V., Evolution and rotation of large-scale photospheric magnetic fields of the Sun during cycles 21-23, Astron. Astrophys., 438, 1067–1082, 2005.

Kumar, P., and Foufoula-Georgiou, E.: Wavelet analysis for geophysical applications, Rev. Geophys. 35(4), 385–412, 1997.

Liszka, L.: Cognitive Information Processing in Space Physics and Astrophysics, Pachart Publishing House, Tuscon, 2003.

Lundstedt, H.: Solar Activity Predicted with Artificial Intelligence, in Space Weather Geophysical Monograph 125, AGU, 2001.

Lundstedt, H., Gleisner, H. and P. Wintoft, Operational forecasts of the geomagnetic Dst index, Geophys. Res. Lett., 29, 34-1–34-4, 2002.

Lundstedt, H., Progress in space weather predictions and applications, Adv. in Space Res., 36, 2516–2523, 2005.

Lundstedt, H., Liszka, L. and R. Lundin, Solar Activity Explored with New Wavelet Methods, 23, 1–7, Annal. Geophys., 2005.

Lundstedt, H., The sun, space weather and GIC effects in Sweden, Adv. in Space Res., 37, 1182–1191, doi:10.1016/j.asr.2005.10.023, 2006.

Lundstedt, H., Solar activity modelled and forecasted: A new approach, Adv. in Space Res, doi:10.1016/j.asr.2006.03.041, 2006.

Lundstedt, H., Liszka, R. Lundin and R. Muscheler, Long-Term Solar Activity Explored with Wavelet Methods, Annal. Geophys., 24, 1–9, 2006.

Mundt, M. D., Maguire II, W. B., and R. P. Chase, Chaos in sunspot cycle: Analysis and prediction, J. Geophys., Res. Vol. 96, 1705–1716, February 1, 1991.

Muscheler, R., Beer, J. and Kubik, P. W.: Long-Term Solar Variability and Climate Change Based on Radionuclide Data From Ice Cores, in Solar Variability and its Effect on the Earth's Atmospheric and Climate System, AGU Geophysical Monograph series (ed. J. Pap, P. F.) 221–235, 2004.

Muscheler, R., Joos, F., Muller, S. A., and Snowball, I.: Not so unusual - today's solar activity, accepted for Nature, 2005.

Obridko, V.N., Sokoloff, D.D., Kuzanyan, K.M., Shelting, B.D., and Zakharov, K.M., Solar cycle according to mean magnetic field data, Mon. Not. R. Astron. Soc., 365, 827–832, 2006.

Parker, E., Cosmical Magnetic Fields, Their origin and activity, pp 466–611, Oxford Univ., Press, 1979.

Polygiannakis, J., Preka-Papadema, P., and Moussas, X.: On signal-noise decomposition of timeseries using the continuous wavelet transform: application to sunspot index, Mon. Not. R. Astron. Soc. 343, 725–734, 2003.

Scherrer, P. H., Wilcox, J. M., Svalgaard, L., Duvall, T. L., Dittmer, P.H. and Gustafson, E. K.: The mean magnetic field of the sun: Observations at Stanford, Solar Physics, 54, 353–361, 1977.

Scherrer, P.H. , Bogart, R.S. Bush, R.I., Hoeksema, J.T., Kosovichev,A.G., Schou, J., Rosenberg, W., Springer, L., Tarbell, T.D., Title A., Wolfson, C.J., Zayer, I., and The MDI Engineering Team, The Solar Oscillations Investigation - Michelson Doppler Imager, Solar Physics 162: 129–188, 1995.

Stenflo, J. O., Global wave patterns in the Sun's magnetic field, Astrophys. Space Sci., 144, 321–336, 1988.

Stenflo, J. O., Evolution of solar magnetic fields: modal structure, Astron. Astrophys, 191, 137–148, 1988.

Stenflo, J.,O., Hidden magnetism, Nature, Vol. 430, 15 July, 2004.

Svalgaard, L., Cliver, E. W, and Kamide, Y.: Sunspot cycle 24: Smallest cycle in 100 years?, Geophys. Res. Lett., 32, L01104, doi:10.1029/2004GL021664, 2005.

Title, A.: Toward Understanding the Sun's Magnetic Fields and Their Effects, EGU General Assembly 2004, Geophysical Research Abstracts Vol. 6, 2004.

Tobias, S. M., The solar cycle: parity interactions and amplitude modulation, Astron. Astrophys., 322, 1007–1017, 1997.

Tobias, S., Hughes, D., and N. Weiss, Unpredictable Sun leaves researchers in the dark, Nature 442, 26, 6 July, 2006.

Torrence, C., and Compo, G. P.: A practical guide to wavelet analysis, Bull. Am. Meteorol. Soc., 79, 61–78, 1998.

Wang, Y.-M, Sheeley J., N.R. and J. Lean, Underrstanding the evolution of the Sun's open magnetic flux, Geophys. Res., lett.,Vol. 27, No. 5, 621–624, March 1, 2000.

LUND UNIVERSITY

Swedish Institute of Space Physics

IRF Scientific Report 296

ISBN 978-91-628-7519-0
ISSN 0284-1703